IOWA STATE UNIVERSITY
Digital Repository

2016

Synthesis and modification of ternary and quaternary chalcogenide nanocrystals

Michelle J. Thompson
Iowa State University

www.manaraa.com

Synthesis and modification of ternary and quaternary chalcogenide nanocrystals

by

Michelle J. Thompson

A dissertation submitted to the graduate faculty

in partial fulfillment of the requirements for the degree of

DOCTOR OF PHILOSOPHY

Major: Chemistry

Program of Study Committee:
Javier Vela, Major Professor
Joseph Burnett
Wenyu Huang
Gordon Miller
Emily Smith

Iowa State University

Ames, Iowa

2016

TABLE OF CONTENTS

NOMENCLATURE

CZTS	Cu_2ZnSnS_4
CMTS	Cu_2MSnS_4 (M = Zn, Mn, Co, Ni)
TEM	Transmission Electron Microscopy
EDX	Energy Dispersive X-Ray Spectroscopy
PXRD	Powder X-Ray Diffraction
EPR	Electron Paramagnetic Resonance Spectroscopy
XPS	X-Ray Photoelectron Spectroscopy

ACKNOWLEDGMENTS

I would like to thank my advisor, Javier Vela for his encouragement, support, guidance, and patience. He has been a great mentor and has taught me a lot about science, as well as how to balance a life outside of the lab. I would also like to thank Gordie Miller for being a member of my committee, as well as my mentor for the Preparing Future Faculty program. I owe a huge thank you to Joe Burnett for the invaluable knowledge, tips, and advice about successfully teaching undergraduate chemistry courses and living to tell the tale. In addition, I would like to thank my committee members, Professors Wenyu Huang and Emily Smith for their input and guidance throughout this journey.

These five years have flown by, thanks in part to the wonderful friendships I found within the Vela group. A special thanks to Purnima Ruberu for teaching me everything I needed to know as a first year graduate student, as well as becoming a great friend and partner in crime! I would also like to thank previous group members, Yijun Guo and Elham Tavasoli for the organic chemistry assistance while writing my prelim proposal. Thanks to Kyle Blakeney, Malinda Reichert and Pat Dilsaver for the model helicopter lessons and road-trip shenanigans, Sam Alvarado for all the sarcasm and science lessons, and John Lin for expanding my Chinese vocabulary. Many thanks to current group members; Josie Del Pilar for the guidance, Himashi Andaraarachchi for the desserts, Long for the laughter (and chocolate!), and Arthur and Hannah for all the coffee, Chinese food and pow-wows. I could not have done this without you guys. A

special thanks to Katie-Jo (honorary Vela group member); you are an amazing friend and you have made living in Ames an incredible experience.

In addition, I would like to thank my parents and parents-in-law for their endless encouragement and enthusiasm for trying to explain to their friends and co-workers exactly what it is that I do. I am amazed everyday by the amount of love, support, and compassion I receive from my wonderful family and ridiculously incredible friends.

Most importantly, I would like to thank my husband Greg for the patience, love, encouragement, and unselfish support he has given me over these past 5 years. It has been quite an adventure and he has been by my side every step of the way. His humor, insight, and excitement have been invaluable. I truly couldn't have done this without him.

ABSTRACT

Cu_2ZnSnS_4 (CZTS) is a promising quaternary material for solar energy conversion and catalysis, but until recently, synthesis of phase pure, anisotropic CZTS nanocrystals remained a challenge. In this thesis, we demonstrate control over the morphology and composition of CZTS nanorods, controlled doping of CZTS nanorods with several transition metal cations, and we extend the synthetic method to ternary sulfide nanocrystals.

We begin by showing that the initial concentration of cationic precursors has a dramatic effect on the morphology and composition of hexagonal wurtzite CZTS nanorods. Our experiments strongly indicate that $Cu(C_5H_7O_2)_2$ is the most reactive of the metal precursors used, $Zn(CH_3CO_2)_2$ is next, and $Sn(CH_3CO_2)_4$ is the least reactive. Using this reactivity series, we are able to purposely fine-tune the morphology (dots vs. rods), composition, and degree of axial phase segregation of CZTS nanocrystals.

Next, we dope divalent, high spin transition metal ions ($M^{2+} = Mn^{2+}$, Co^{2+}, Ni^{2+}) into the tetrahedral Zn^{2+} sites of wurtzite CZTS nanorods. The resulting $Cu_2M_xZn_{1-x}SnS_4$ (CMTS) nanocrystals retain the hexagonal crystalline structure, elongated morphology, and broad visible light absorption profile of the undoped CZTS nanorods. The nanorods doped with Mn^{2+} and Co^{2+} are EPR active, with spectra which are representative of the literature reports for these transition metals. EPR also shows that washing the nanocrystals with trioctylphosphine oxide (TOPO) is an efficient way to remove excess Mn^{2+} ions from the particle surface. XPS and FTIR show that $Cu_2Mn_xZn_{1-x}SnS_4$ nanocrystals aggregate not through dichalcogenide bonds, but through excess metal ions

crosslinking the sulfur-rich surfaces of neighboring particles. This was also observed in the ternary sulfide (thiospinel) nanocrystals.

In addition to CZTS and CMTS, we extend our synthetic method to synthesize ternary metal sulfides, namely thiospinel and pyrite phase nanocrystals. Due to their application in a variety of energy and catalysis fields, thiospinels and pyrites have attracted attention in recent years. Typically, these materials are synthesized in bulk, with high temperature methods and low surface areas, making them less than ideal for many applications. In this report we use low temperature, solvothermal methods to synthesize nanocrystalline, ternary thiospinels. The nanocrystals have a variety of morphologies, including spheres and nanorods, and show a broad absorbance in the visible range. This is the first time several of the materials are reported in nano sizes. We also report on the attempted synthesis of pyrite nanocrystals.

The results of this work will improve our ability to fabricate CZTS and related nanostructures for photovoltaics and photocatalysis. In addition, these results may help expand the synthetic applicability of CZTS and CMTS materials beyond photovoltaics and into the fields of spintronics and magnetic data storage. Synthesizing nano-scale thiospinels and pyrites may have a direct impact on the catalysis and energy fields as well.

CHAPTER I

INTRODUCTION

General Introduction

This thesis describes the synthesis and characterization of ternary and quaternary metallic and semiconducting nanocrystals. This work reports progress toward phase-pure Cu_2ZnSnS_4 nanorods, with an emphasis on the metal precursor reactivity and how it relates to the composition gradients of the product. These nanorods are then doped with different tetrahedral, high spin, transition metal cations and characterized. In addition, this thesis presents work toward synthesizing materials related to CZTS: ternary metal sulfides in thiospinel and pyrite structures.

Semiconductor nanocrystals

Nanoparticles are, very generally, particles with dimensions between 1 and 100 nanometers. This work will discuss, more specifically, semiconducting nanocrystals. These materials are nano-sized light-emitting crystalline materials which exhibit exciting optical and electronic properties, such as carrier multiplication, spectral diffusion, and single-particle blinking.[1]

In a semiconductor, there is an energy gap between the occupied valence band of the material and the unoccupied conduction band. The band gap is the energy which is required to promote an electron from the valence band into the conduction band. When the material absorbs a photon with energy that is greater than the band gap, the electron is promoted to the conduction band, leaving a positively charged hole behind in the valence

band. This electron-hole pair is called an exciton. An electric field may be applied to move the electron and hole, creating current.[2]

Semiconductor nanocrystals have long been recognized as ideal materials for optoelectronic devices, solar energy harvesting and conversion, and molecular and cellular imaging.[1,3] They are typically fabricated as layers of thin films on substrates or as colloidal suspensions in solution form. Solution phase synthesis has been optimized to provide control over size, morphology, and monodispersity. The particles synthesized in solution typically have a capping layer on the surface comprised of organic surfactants. These semiconducting nanocrystals are heavily utilized due to their size and composition-tunable band gaps, which can vary between 0.3 eV and 4.1 eV (300-4000 nm), broad absorption, long-lived excitons, and good solubility.[4-6]

Nanorods are one type of nanocrystalline morphology, with aspect ratios higher than one (spheres), but typically less than five. Their morphology lies between that of quantum dots and nano-wires, with increased solubility over nanowires, leading to increased utility in solution phase catalysis. Semiconductor nanorods are of particular interest due to their ability to generate multiple excitons (electron hole-pairs).[7,8] Multiple exciton generation can lead to exciting results, such as optical amplification, improvements in efficiencies of solar cells, lasing, and non-linear optics.[8]

Although many colloidal reactions favor the formation of spheres (thermodynamically favored), nanorods can be produced by carefully controlling precursor loading (concentration). In addition, various organic and inorganic surfactants can be used to control growth of certain crystal facets to produce anisotropic nanocrystals.[9,10] This thesis modifies a reported method of synthesizing nanorods through

a combination of thiols as surface ligands to control morphology.[11] This work also explores the precursor reactivity and loading as methods for controlling the morphology and composition of the nanocrystals.

Doped semiconductor nanocrystals

Doping is the purposeful and controlled incorporation of impurities into a material. The doping of transition metals into bulk and nanocrystalline semiconductors is a field which has been explored for numerous years.[12,13] When a system is doped with a new species, the properties of that system may be drastically altered and new/improved applications can be anticipated. A general guideline for substitutional doping (replacing an existing ion within the crystal lattice) is that the ionic radius of the dopant should be within 10% of the ionic radius of the ion it will substitute. In addition, the lattice parameter(s) should be reasonably close (within 15%). If both of these conditions are met, there is a reasonable chance that the doping will be successful.

In nanocrystalline materials, one of the most commonly used dopants has been manganese, since it has been shown to incorporate easily into other systems and can be doped in high quantities. Reports have demonstrated that manganese can be doped into a variety of systems, including CdS(Se) and ZnS(Se).[13,14] There are also many reports on doping semiconductor nanocrystals with rare-earth metals, such as ytterbium and europium to enhance photon upconversion.[15] Many systems utilize transition metal cations, since their unpaired d and f electrons can lead to interesting and desirable magnetic properties. Some other common transition metal dopants in nanocrystals have included nickel, cobalt, copper, titanium, and molybdenum.[15-18]

Cu₂ZnSnS₄

In recent years, Cu₂ZnSnS₄ (CZTS) has garnered attention for its potential optoelectronic applications, such as solar energy harvesting and photocatalysis.[19-22] This quaternary, I₂–II–IV–VI₄ semiconductor is promising for solar conversion and photocatalysis applications due to its direct band gap of around 1.5 eV, which corresponds to 826 nm, which means that CZTS can absorb most of the solar spectrum.[23] The material has a high absorption coefficient and high carrier concentrations, similar to $CuIn_xGa_{1-x}Se_2$ (CIGS, to which CZTS is often compared). CZTS is also desirable because the component materials have a lower toxicity compared with other popular photovoltaic materials, such as the cadmium, arsenic, and indium utilized in CIS ($CuInSe_2$) and CIGS devices. In addition, copper, zinc, tin and sulfur are all relatively inexpensive and widely abundant materials, with concentrations in the Earth's crust of: Cu – 50 ppm, Zn – 75 ppm, Sn – 2.2 ppm, S – 260 ppm.[20]

CZTS is known to crystallize in three different structures: kesterite ($I\bar{4}$), stannite ($I\bar{4}2m$), or wurtzite ($P6_3mc$). The kesterite phase of CZTS is derived from the CIGS structure through isoelectronic substitution of zinc and tin in place of indium or gallium, and is the most stable of the three structures.[24] In the kesterite and stannite structures, which are similar to zinc blende, the metal cations are located in tetrahedral bonding positions which are known and fixed. The difference between the kesterite and stannite structures is the layering, shown in Figure 1. In the stannite unit cell, there are distinct layers of copper cations and layers of zinc cations, but never both in the same layer. However, in the kesterite structure, there are still copper cation layers, but there are also layers which contain both zinc and copper cations. In contrast to the order in kesterite and

stannite, in the wurtzite phase the metal cation sites are mixed and the positions of the zinc, copper, and tin are random.[25]
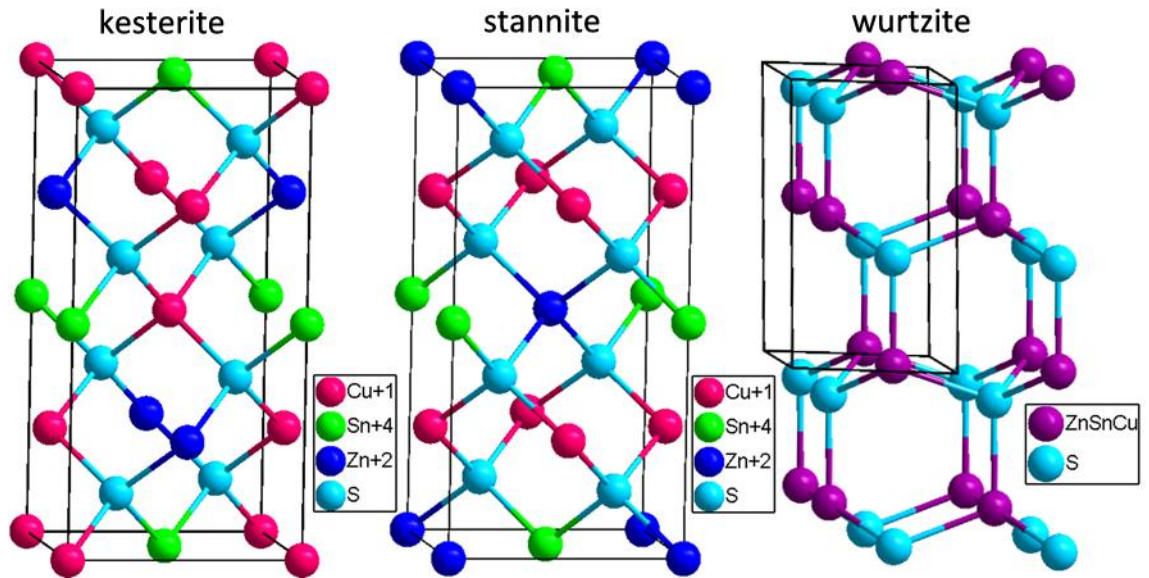

Figure 1. Three most common crystal structures of Cu_2ZnSnS_4: kesterite, stannite and wurtzite.

While there are many potential applications for the material, synthesis of phase-pure CZTS nanocrystals has been a challenge. While phase pure CZTS can be achieved, the phase diagram shows that it can only be formed in a very small region, which makes the synthesis difficult, and impurity phases, such as the binary metal sulfides, in the final product are common.[24] These phases can be difficult to distinguish by powder x-ray diffraction (PXRD), so more in-depth characterization techniques are often needed. This thesis demonstrates the synthesis of CZTS nanorods with control over the composition and morphology by manipulating the precursor loadings of the metal cations.

Recent studies have shown the utility of CZTS nanocrystals and thin films as the solar absorbing layer in photovoltaic devices. In 2014, a solar cell made using CZTS was

reported to have an efficiency of 12.6%, which is nearly half-way to their maximum theoretical efficiency of 31%.[26,27] Along with solar cells, CZTS and CZTS-heterostructures have been shown to be valuable for photocatalysis. There have been several reports demonstrating that CZTS and CZTS heterostructures are photocatalytically active for hydrogen evolution reactions.[28,29]

Ternary metal sulfide nanocrystals

Due to their application in a variety of energy and catalysis fields, thiospinels and pyrites have attracted attention in recent years. Thiospinel materials have been utilized as supercapacitors, anodes in batteries, and catalysts.[30-33] Pyrites have applications in photovoltaics, thermoelectrics, spin-tronics, and catalysis.[34-37] Typically, these materials are synthesized in bulk, using high temperature methods and producing products with low surface areas.

Their low surface areas make these bulk materials less than ideal for applications, but there are very few reports available demonstrating synthesis of these materials in nano sizes. A typical thiospinel has the formula AB_2X_4, while pyrites have the formula AX_2. The unit cells are shown in Figure 2 ($CuCoS_4$ represents the pyrite structure, and $CuCo_2S_4$ represents the thiospinel). This thesis reports on the synthesis of several ternary thiospinels for the first time in nano size, as well as several attempted synthesis routes to make ternary pyrite nanocrystals.
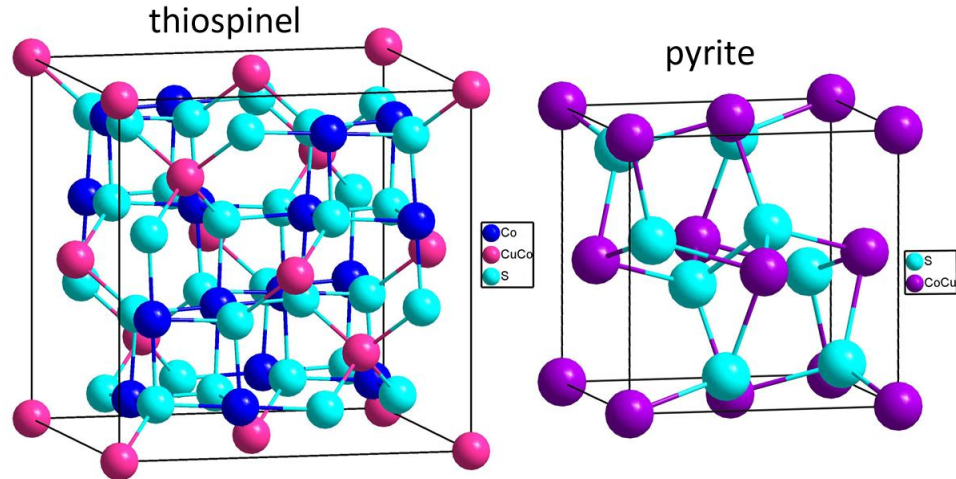
Figure 2. Pyrite and thiospinel unit cells.

Thesis Organization

Chapter 2 of this thesis describes the synthesis and characterization of phase pure, anisotropic Cu_2ZnSnS_4 nanocrystals. This chapter demonstrates that the initial precursor loading of the metal cations has a dramatic effect on the morphology and composition of the resulting nanocrystals. This reactivity is manipulated to control the composition gradients which are typically found in CZTS nanorods, as well as to control the overall composition and morphology of the nanocrystals. The reactivity of the metal salts is determined to decrease from $Cu(C_5H_7O_2)_2 > Zn(CH_3CO_2)_2 > Sn(CH_3CO_2)_4$.

Chapter 3 extends the synthesis of CZTS nanorods to include CZTS nanorods doped with tetrahedral, high spin, transition metal cations. The cations chosen are Co^{2+}, Ni^{2+} and Mn^{2+}. Several methods of characterization confirm the presence of the transition metal dopants, while EPR is used to distinguish between surface and internally doped nanocrystals. A TOPO wash is used to remove manganese ions on the surface of the

nanocrystals. A thiol wash is also utilized and a hypothesis is given for why the wash decreases the aggregation found in the nanocrystals.

Chapter 4 discusses structures that are related to CZTS; ternary metal sulfides (thiospinels and pyrites). These materials have not been extensively explored in nano-size, but have been shown to be useful materials in the bulk. This chapter presents the successful synthesis of several thiospinels, and their subsequent characterization. The attempted synthesis of several ternary pyrites is also reported. Chapter 5 summarizes the previous chapters and future outlook of this work.

References

[1] Smith, A. M.; Nie, S. Semiconductor Nanocrystals: Structure, Properties, and Band Gap Engineering. *Acc. Chem.Res.* **2010**, *43*, 190–200.

[2] Greenham, N. C.; Peng, X. G.; Alivisatos, A. P. Charge Separation and Transport in Conjugated-polymer/semiconductor-nanocrystal Composites Studied by Photoluminescence Quenching and Photoconductivity. *Phys. Rev. B* **1996**, *54*, 17628–17637.

[3] Kamat, P. V. Quantum Dot Solar Cells. Semiconductor Nanocrystals as Light Harvesters. *J. Phys. Chem. C* **2008**, *112*, 18737–18753.

[4] Talapin, D. V.; Lee, J.-S.; Kovalenko, M. V.; Shevchenko, E. V. Prospects of Colloidal Nanocrystals for Electronic and Optoelectronic Applications. *Chem. Rev.* **2010**, *110*, 389–458.

[5] Alivisatos, A. P. Semiconductor Clusters, Nanocrystals, and Quantum Dots. *Science* **1996**, *271*, 933–937.

[6] Bruchez, M.; Moronne, M.; Gin, P.; Weiss, S.; Alivisatos, A. P., Semiconductor Nanocrystals as Fluorescent Biological Labels. *Science* **1998**, *281*, 2013–2016.

[7] Nozik, A. Multiple Exciton Generation in Semiconductor Quantum Dots. *Chem. Phys. Lett.* **2008**, *457*, 3–11.

[8] Klimov, V. Mechanisms for Photogeneration and Recombination of Multiexcitons in Semiconductor Nanocrystals: Implications for Lasing and Solar Energy Conversion. *J. Phys. Chem. B.* **2006**, *110*, 16827–16845.

[9] Peng, Z. A.; Peng, X. G. Mechanisms of the Shape Evolution of CdSe Nanocrystals. *J. Am. Chem. Soc.* **2001**, *123*, 1389–1395.

[10] Buhro, W. E.; Colvin, V. L. Semiconductor Nanocrystals - Shape Matters. *Nature Mater.* **2003**, *2*, 138–139.

[11] Singh, S.; Liu, P.; Singh, A.; Coughlan, C.; Wang, J.; Lusi, M.; Ryan, K. M. Colloidal $Cu_2ZnSn(SSe)_4$ (CZTSSe) Nanocrystals: Shape and Crystal Phase Control to Form Dots, Arrows, Ellipsoids, and Rods. *Chem. Mater.* **2015**, *27*, 4742–4748.

[12] Bhargava, R. N. The Role of Impurity in Doped Nanocrystals. *J. Lumin.* **1997**, *72*, 46–48.

[13] Erwin, S. C.; Zu, L. J.; Haftel, M. I.; Efros, A. L.; Kennedy, T. A.; Norris, D. J. Doping Semiconductor Nanocrystals. *Nature* **2005**, *436*, 91–94.

[14] Beaulac, R.; Archer, P. I.; Ochsenbein, S. T.; Gamelin, D. R. Mn^{2+}–Doped CdSe Quantum Dots: New Inorganic Materials for Spin–Electronics and Spin–Photonics. *Adv. Funct. Mater.* **2008**, *18*, 3873–3891.

[15] Haase, M.; Schaefer, H. Upconverting Nanoparticles. *Angew. Chem. Int. Ed.* **2011**, *50*, 5808–5829.

[16] Radovanovic, P. V.; Norberg, N. S.; McNally, K. E.; Gamelin, D. R., Colloidal Transition-metal-doped ZnO Quantum dots. *J. Am. Chem. Soc.* **2002**, *124*, 15192–15193.

[17] Norberg, N. S.; Parks, G. L.; Salley, G. M.; Gamelin, D. R. Giant Excitonic Zeeman Splittings in Colloidal Co^{2+}–doped ZnSe Quantum Dots. *J. Am. Chem. Soc.* **2006**, *128*, 13195–13203.

[18] Singhal, A.; Achary, S. N.; Manjanna, J.; Chatterjee, S.; Ayyub, P.; Tyagi, A. K., Chemical Synthesis and Structural and Magnetic Properties of Dispersible Cobalt– and Nickel–Doped ZnO Nanocrystals. *J. Phys. Chem. C* **2010**, *114*, 3422–3430.

[19] Guo, Q.; Ford, G. M.; Yang, W.-C.; Walker, B. C.; Stach, E. A.; Hillhouse, H. W.; Agrawal, R. Fabrication of 7.2% Efficient CZTSSe Solar Cells Using CZTS Nanocrystals. *J. Am. Chem. Soc.* **2010**, *132*, 17384–17386.

[20] Katagiri, H.; Jimbo, K.; Maw, W. S.; Oishi, K.; Yamazaki, M.; Araki, H.; Takeuchi, A., Development of CZTS-based Thin Film Solar Cells. *Thin Solid Films* **2009**, *517*, 2455–2460.

[21] Suryawanshi, M. P.; Agawane, G. L.; Bhosale, S. M.; Shin, S. W.; Patil, P. S.; Kim, J. H.; Moholkar, A. V. CZTS Based Thin Film Solar Cells: a Status Review. *Mater. Technol.* **2013**, *28*, 98–109.

[22] Zhou, H.; Hsu, W.-C.; Duan, H.-S.; Bob, B.; Yang, W.; Song, T.-B.; Hsu, C.-J.; Yang, Y. CZTS Nanocrystals: a Promising Approach for Next Generation Thin Film Photovoltaics. *Energy Environ. Sci.* **2013**, *6*, 2822–2838.

[23] Guo, Q.; Hillhouse, H. W.; Agrawal, R., Synthesis of Cu_2ZnSnS_4 Nanocrystal Ink and Its Use for Solar Cells. *J. Am. Chem. Soc.* **2009**, *131*, 11672–11673.

[24] Hossain, M. I. Prospects of CZTS Solar Cells From the Perspective of Material Properties, Fabrication Methods and Current Research Challenges. *Chalcogenide Lett.* **2012**, *9*, 231–242.

[25] Cui, Y.; Deng, R. P.; Wang, G.; Pan, D. C. A General Strategy for Synthesis of Quaternary Semiconductor Cu_2MSnS_4 (M = Co^{2+}, Fe^{2+}, Ni^{2+}, Mn^{2+}) Nanocrystals. *J. Mater. Chem.* **2012**, *22*, 23136–23140.

[26] Winkler, M. T.; Wang, W.; Gunawan, O.; Hovel, H. J.; Todorov, T. K.; Mitzi, D. B. Optical Designs that Improve the Efficiency of $Cu_2ZnSn(S,Se)_4$ Solar Cells. *Energy Environ. Sci.* **2014**, *7*, 1029–1036.

[27] Wang, W.; Winkler, M. T.; Gunawan, O.; Gokmen, T.; Todorov, T. K.; Zhu, Y.; Mitzi, D. B. Device Characteristics of CZTSSe ThinFilm Solar Cells with 12.6% Efficiency. *Adv. Energy Mater.* **2014**, *4*, 1301465.

[28] Wang, J.; Zhang, P.; Song, X.; Gao, L. Surfactant-free Hydrothermal Synthesis of Cu_2ZnSnS_4 (CZTS) Nanocrystals with Photocatalytic Properties. *RSC Adv.* **2014**, *4*, 27805–27810.

[29] Yu, X.; Shavel, A.; An, X.; Luo, Z.; Ibanez, M.; Cabot, A. Cu_2ZnSnS_4-Pt and Cu_2ZnSnS_4-Au Heterostructured Nanoparticles for Photocatalytic Water Splitting and Pollutant Degradation. *J. Am. Chem. Soc.* **2014**, *136*, 9236–9239.

[30] Zhang, Y.; Sun, W.; Rui, X.; Li, B.; Tan, H. T.; Guo, G.; Madhavi, S.; Zong, Y.; Yan, Q. One-Pot Synthesis of Tunable Crystalline Ni3S4@Amorphous MoS2 Core/Shell Nanospheres for High-Performance Supercapacitors. *Small* **2015**, *11*, 3694–3702.

[31] Wang, Q.; Jiao, L.; Du, H.; Si, Y.; Wang, Y.; Yuan, H. Co3S4 Hollow Nanospheres Grown on Graphene as Advanced Electrode Materials for Supercapacitors. *J. Mater. Chem.* **2012**, *22*, 21387–21391.

[32] Mahmood, N.; Zhang, C.; Jiang, J.; Liu, F.; Hou, Y. Multifunctional Co3S4/Graphene Composites for Lithium Ion Batteries and Oxygen Reduction Reaction. *Chem. Eur. J.* **2013**, *19*, 5183–5190.

[33] Li, T.; Li, H.; Wu, Z.; Hao, H.; Liu, J.; Huang, T.; Sun, H.; Zhang, J.; Zhang, H.; Guo, Z. Colloidal Synthesis of Greigite Nanoplates with Controlled Lateral Size for Electrochemical Applications. *Nanoscale* **2015**, *7*, 4171–4178.

[34] Thackeray, M. M.; Depicciotto, L. A.; Dekock, A.; Johnson, P. J.; Nicholas, V. A.; Adendorff, K. T., Spinel Electrodes for Lithium Batteries - A Review. *J. Power Sources* **1987**, *21*, 1–8.

[35] Han, J.-T.; Huang, Y.-H.; Huang, W. Solvothermal Synthesis and Magnetic Properties of Pyrite $Co_{1-x}Fe_xS_2$ with Various Morphologies. *Mater. Lett.* **2006**, *60*, 1805–1808.

[36] De Los Reyes, J. A.; Vrinat, M.; Geantet, C.; Breysse, M.; Grimblot, J. Supported Ternary Sulfide Phases: Characterization and Catalytic Properties of Alumina-Supported $Ni_xRu_{1-x}S_2$. *J. Catal.* **1993**, *142*, 455–464.

[37] Liu, K.; Ji, N.; Ma, Z., Phases and Thermoelectric Properties of Bulk $NiSb_2$ and Composite of $NiSb_2$ and $CoSb_3$ Prepared by Sintering. *Adv. Mater. Res.* **2012**, *503*, 507–510.

CHAPTER 2

AXIAL COMPOSITION GRADIENTS AND PHASE SEGREGATION

REGULATE THE ASPECT RATIO OF Cu_2ZnSnS_4 NANORODS

Michelle J. Thompson, T. Purnima A. Ruberu, Kyle J. Blakeney, Karen V. Torres,

Patrick S. Dilsaver, Javier Vela

Abstract

Cu_2ZnSnS_4 (CZTS) is a promising material for solar energy conversion, but synthesis of phase pure, anisotropic CZTS nanocrystals remains a challenge. We demonstrate that the initial concentration (loading) of cationic precursors has a dramatic effect on the morphology (aspect ratio) and composition (internal architecture) of hexagonal wurtzite CZTS nanorods. Our experiments strongly indicate that $Cu(C_5H_7O_2)_2$ is the most reactive of the metal salt precursors, $Zn(CH_3CO_2)_2$ is the next most reactive, and $Sn(CH_3CO_2)_4$ is the least reactive of the three. Using this reactivity series, we are able to purposely fine-tune the morphology (dots vs. rods) and degree of axial phase segregation of CZTS nanocrystals. These results will improve our ability to fabricate CZTS nanostructures for photovoltaics and photocatalysis.

Introduction

Cu$_2$ZnSnS$_4$ or "CZTS" is one of the most promising materials for solar energy harvesting.[1-3,6-14] Made of highly abundant, widely distributed and relatively biocompatible elements, and with a direct band gap of 1.5 eV, CZTS has emerged as an affordable, greener and more sustainable alternative to other semiconductors such as GaAs, CdTe, CuInS$_2$ (CIS), or CuIn$_x$Ga$_{1-x}$Se$_2$ (CIGS). Different groups reported the synthesis of low dimensionality, nanosized versions of CZTS,[15-37] but this is not without challenges. In particular, methods capable of producing anisotropic CZTS nanostructures are lacking. Anisotropy is desirable for applications that rely on efficient charge carrier mobility across grain boundaries, as well as on the ability to suppress electron-hole pair recombination, such as in photovoltaic cells and photocatalytic devices.[4,38,39]

Results and discussion

In our search for cadmium-free nanomaterials suitable for solar to chemical energy conversion, we were attracted to a report on the synthesis of CZTS nanorods.[17] Modified slightly, this method uses the hot injection of 1-dodecylthiol (1-DDT, 0.52 mmol) and tert-dodecylthiol (t-DDT, 3.7 mmol) to a mixture of Cu(C$_5$H$_7$O$_2$)$_2$ (0.50 mmol), Zn(CH$_3$CO$_2$)$_2$•2H$_2$O (0.25 mmol), Sn(CH$_3$CO$_2$)$_4$ (0.25 mmol), trioctylphosphine oxide (TOPO, 1.75 mmol) and 1-octadecene (ODE, 5 mL) under Ar at 120 °C, followed by heating to 210 °C for 30 min. This procedure typically yields CZTS nanorods with a mean length of 23.7 ± 4.1 nm, a mean diameter of 7.3 ± 1.4 nm, and a length-to-diameter 'aspect' ratio of 3.3 ± 0.8. (Figure 1-A and Table 1-A). Unfortunately, simply repeating this procedure using different injection (nucleation) temperatures or reaction (growth)

times, a common way to affect the anisotropy of chalcogenide nanocrystals,[40,41] did not affect the nanorods' original aspect ratio (see Supporting Information).

We hypothesized that the reason behind the apparent lack of 'plasticity' of CZTS nanorods might lie within their multi-element composition. First-principles studies showed this quaternary phase is stable only within a very small domain of chemical potentials.[42,7] Slight deviations from optimal growth conditions result in spontaneous formation of undesired phases such as ZnS, SnS, SnS_2, CuS, and Cu_2SnS_3 rather than the desired CZTS phase. Critically, the first method of choice for distinguishing between possible nanocrystalline phases, powder X-ray diffraction (XRD), is of limited use here because CZTS and common impurities such as ZnS adopt very similar hexagonal wurtzite crystal structures (Figure 2) (Notes: CZTS's other well-known structure, tetragonal kesterite, was not observed here; Neutron diffraction can provide better phase resolution but is less available).[44,45] Nevertheless, energy-dispersive X-ray spectroscopy (EDX) line scans on several nanorods prepared by the aforementioned procedure consistently showed marked axial composition gradients. Specifically, the amount of copper increased and the amount of zinc decreased from one side of the nanorods to the other (Figure 3).
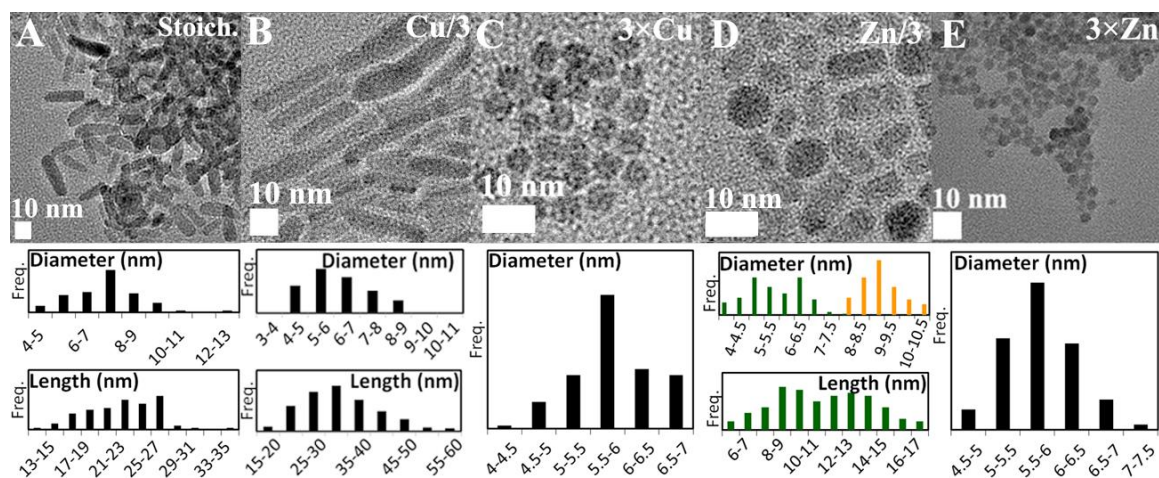
Figure 1. TEM of Cu$_2$ZnSnS$_4$ (CZTS) particle size and morphology as a function of precursor loading: (A) CZTS nanorods made with a stoichiometric (2:1:1) ratio of Cu, Zn and Sn,[17] (b) one third the amount of Cu, (C) three times the amount of Cu, (D) one third the amount of Zn, and (E) three times the amount of Zn (>100 particles measured). (Stoichiometric conditions: 48 mM Cu(C$_5$H$_7$O$_2$)$_2$ 24 mM Zn(CH$_3$CO$_2$)$_2$, and 24 mM Sn(CH$_3$CO$_2$)$_4$ in TOPO-ODE, 0.4 M 1-DDT/t-DDT, 120 °C injection, 210 °C growth for 30 min)

Table 1. Effect of precursor loading on the synthesis of CZTS nanorods.[a]

Loading	Length / nm	Diameter / nm	Aspect ratio	EDX C:Z:T:S	XRD Phase(s)
Stoich.[a]	23.7 ± 4.1	7.3 ± 1.4	3.3 ± 0.8	3:1:1:4	CZTS(w)
Cu/3	33.3 ± 6.7	6.1 ± 1.1	5.5 ± 1.5	5:2:1:9	CZTS(w)
3×Cu	-	5.8 ± 0.5	dots	7:0.1:0.1:2	Cu$_{1.95}$S+ Cu$_{31}$S$_{16}$+ Sn$_3$S$_2$
Zn/3	11.8 ± 2.7	5.9 ± 0.9	2.0 ± 0.6	0.2:1:0.01:1	ZnS+
	-	9.3 ± 0.7	dots	4:1:0:1	Cu$_{31}$S$_{16}$
3×Zn	-	5.8 ± 0.5	dots	9:3:1:4	ZnS/CZTS(w)

[a][Cu]$_T$ = 48 mM, [Zn]$_T$ = 24 mM, [Sn]$_T$ = 24 mM, [S]$_T$ = 0.40 M (see text).

We recently observed similar behavior in ternary CdS$_{1-x}$Se$_x$ nanorods ($0 \leq x \leq 1$).[40,41] After careful study, we learned that axial composition gradients could be purposely induced or suppressed by fine-tuning the loading and/or reactivity of chemical precursors.[29,43] Mismatched reactivities lead to sequential nucleation of phases and axial composition gradients, whereas purposely-matched reactivities lead to concurrent

nucleation and more complete alloying.[41] We conjectured that the same principles could apply here to CZTS nanorods, because preferential precursor reactivity would explain the observed axial composition gradients (Figure 3). However, the observation of opposing copper-rich and zinc-rich tips alone was not enough to discern which cationic precursor (copper, zinc, or tin) was more or less reactive or which metal sulfide nucleated first. To sort out these differences, we purposely increased or decreased the loading (concentration) of the different cationic precursors in the original synthesis while keeping all other conditions constant (Table 1).
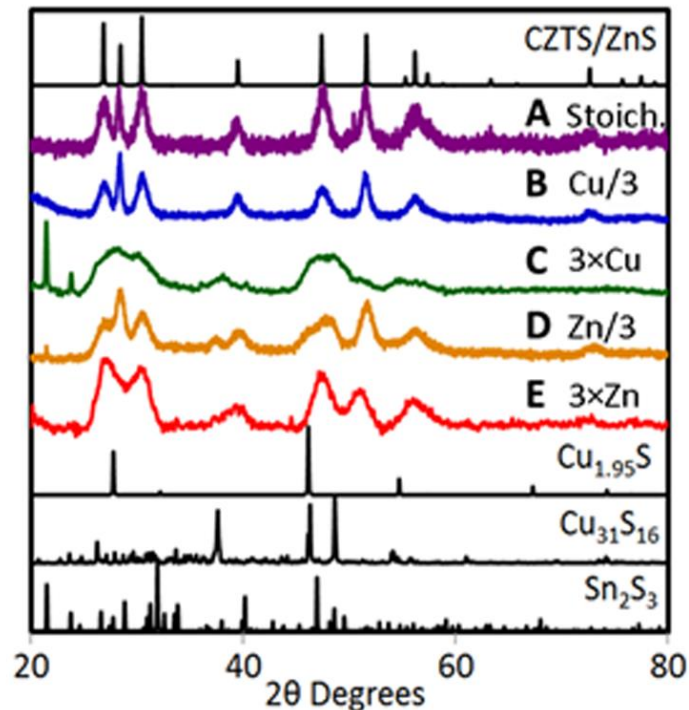

Figure 2. XRD patterns of hexagonal (wurtzite) CZTS/ZnS, common impurities, and nanocrystals synthesized using different amounts of copper, zinc and tin precursors. (A) CZTS rods, (B) Cu/3, (C) Zn/3, (D) 3×Cu, (E) 3×Zn.
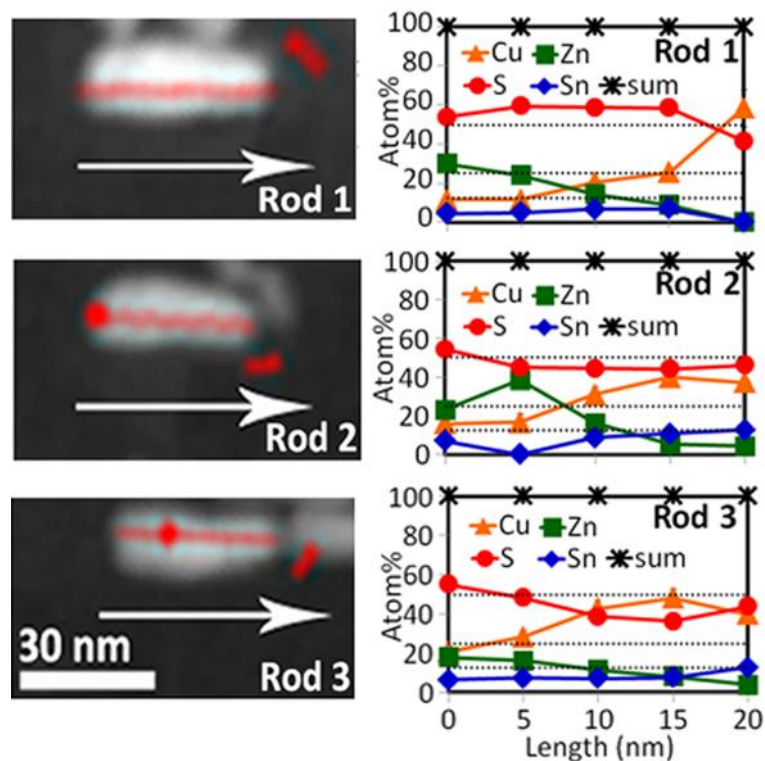
Figure 3. EDX line scans on individual CZTS nanorods made with a stoichiometric (2:1:1) mixture of cationic precursors (48 mM $Cu(C_5H_7O_2)_2$, 24 mM $Zn(CH_3CO_2)_2$, and 24 mM $Sn(CH_3CO_2)_4$) show copper content increases and zinc content decreases from one end of the nanorods to the other (left to right here). Dotted lines correspond to the theoretical CZTS composition (25 atom% Cu, 12.5 atom% Zn and Sn each, and 50 atom% S).

The preparation we originally used employs stoichiometric (2:1:1) amounts of three cationic precursors (Table 1A).[17] Using only one third of the original amount of copper ('Cu/3', 0.17 mmol) resulted in the formation of much more elongated CZTS nanorods having a mean length of 33.3 ± 6.7 nm, a mean diameter of 6.1 ± 1.1 nm, and an aspect ratio of 5.5 ± 1.5 (Figures 1B and 2B, Table 1B). This constitutes an increase of 41% in length and 67% in aspect ratio upon slashing the copper loading to one third. In contrast, using three times the original amount of copper ('3×Cu', 1.50 mmol) resulted in

the formation of copper-rich dots (aspect ratio ≈ 1) having a mean diameter of 5.8 ± 0.5 nm (Figures 1C and 2C, Table 1C).

The type and initial concentration (loading) of copper precursor are known to have an effect on the shape of CuS and $CuInSe_2$ nanocrystals.[47,48] In our case, the fact that CZTS aspect ratio is so dependent on copper loading, along with the afore-mentioned axial composition gradient, strongly indicate that the copper precursor is more reactive than the zinc and tin precursors. Selectivity for anisotropic growth and formation of composition gradients are closely related phenomena that result from sequential nucleation events.[41] We interpret these results as follows: During a typical CZTS nanorod prep, the most reactive (copper) precursor quickly reacts (with 1-DDT/t-DDT) to homogeneously nucleate copper sulfide seeds; the less reactive zinc and tin precursors subsequently react to heterogeneously nucleate zinc, tin (and leftover copper) sulfide along the unique c(z) axis of existing hexagonal wurtzite seeds, resulting in anisotropic growth (elongation). This series of events yields CZTS nanorods with composition gradients.
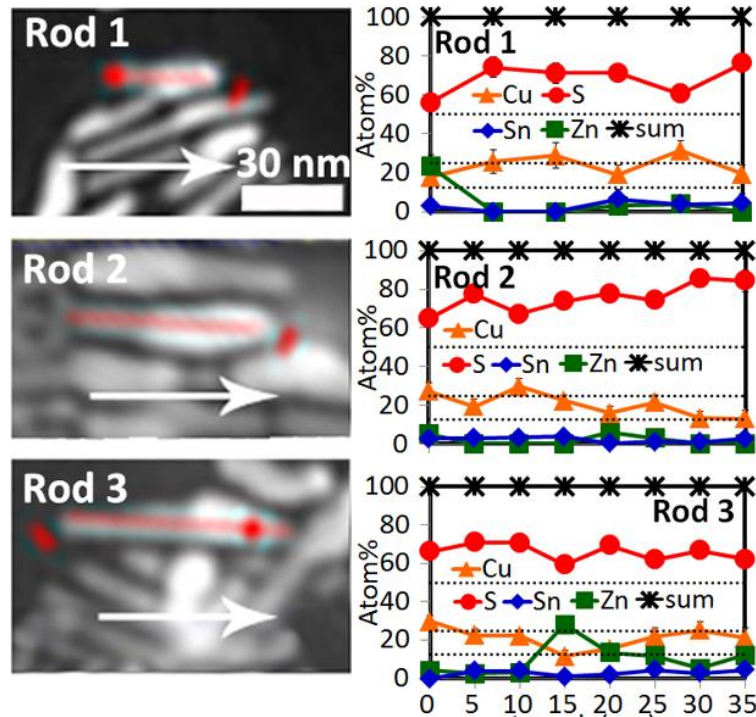
Figure 4. EDX line scans on individual CZTS nanorods made with only one third of the original copper loading ('Cu/3') show that the content of each metal remains fairly constant from one side of the nanorods to the other. Dotted lines correspond to the theoretical CZTS composition (25 atom% Cu, 12.5 atom% Zn and Sn each, and 50 atom% S).

In comparison to the stoichiometric experiment, a lower initial concentration of copper leads to a decrease in the rate of nucleation of copper sulfide. Slower homogeneous nucleation produces less seeds; it also leaves more precursors in solution to grow longer rods.[41] The three metal precursors can then heterogeneously nucleate at more comparable rates, producing longer CZTS nanorods with smaller composition gradients. Indeed, EDX line scans on the copper 'starved', 'Cu/3' nanorods consistently revealed much less pronounced composition gradients (Figure 4). On the contrary, a higher initial concentration of copper leads to a further increase in the rate of nucleation of copper sulfide. At its most extreme, nucleation is so fast and produces so many seeds that it quickly results in CZTS nanocrystals with spherical morphology (Figure 1C).

In contrast to the copper loading-dependent behavior, changing the zinc or tin loading does not directly affect the nanorods' aspect ratio. For example, using only one third of the original amount of zinc ('Zn/3', 0.08 mmol) resulted in a mixture of two different types of particles with rod (11.8 ± 3 nm length, 5.9 ± 0.9 nm diameter, 2.0 ± 0.6 aspect ratio) and dot-like morphologies (9.3 ± 0.7 nm diameter) (Figures 1D and 2D, Table 1D). EDX elemental mapping, in combination with ensemble XRD measurements showed that the rod-like particles are Zn-rich (mostly ZnS with some copper and tin), whereas the dot-like particles are Cu-rich ($Cu_{31}S_{16}$ with some Zn) (Figure 5a and 5b). Clearly, 'starving' the reaction of zinc precursor causes almost complete phase segregation (Figure 5). In turn, using three times the original amount of zinc ('3×Zn', 0.75 mmol) resulted in the formation of CZTS dots having a mean diameter of 5.8 ± 0.5 nm (Figures 1E and 2E, Table 1E).

We also sought to confirm the above results by performing time evolution experiments. Briefly, aliquots were taken out of the reaction mixture during the synthesis of CZTS nanorods and analyzed by optical spectroscopy, TEM and EDX. Using a stoichiometric mixture of cationic precursors, the nanocrystals C:Z:T:S composition was 2:0.04:0.02:1 after 5 min and 2:1:0.2:4 after 30 min (Table 2). Thus, only after the full 30 min reaction time were zinc and tin incorporated into the particles, which is supported by previous observations on thin films.[5,46] Similarly, using one third of the copper loading ('Cu/3'), the nanocrystals C:Z:T:S composition was 2:1:0.06:4 after 5 min and 3:4:1:5 after 30 min reaction (Table 2 and Figure 6). In addition, the nanorods' aspect ratio nearly doubled from 5.2 ± 1.1 after 5 min to 3.0 ± 1.3 after 30 min. The biggest contribution was a change in nanorod length from 16.3 ± 6 nm after 5 min to 32.2nm ± 7nm after 30 min.

Nanorod diameters remained statistically similar at 5.5 ± 0.5 nm after 5 min and 6.2 nm $\pm$ 0.7 nm after 30 min (Figure 6). Thus, time evolution experiments confirmed that: (1) The reactivity order of the cationic precursors used here (and with it, the rate of nucleation of their binary sulfides) decreases in the order $Cu(C_5H_7O_2)_2$ (most reactive) $> Zn(CH_3CO_2)_2$ $> Sn(CH_3CO_2)_4$ (least reactive); (2) decreasing the loading of the most reactive (copper) precursor increases the nanorods' aspect ratio by lowering the rate of nucleation of seed particles; and (3) nanorods continue to elongate over time (5-30 min) via heterogeneous nucleation on existing seeds.

Table 2. Evolution of CZTS nanorod composition over time.[a]

| Loading | time/min | % Atom | | | |
		Cu	Zn	Sn	S
Stoichiometric	5	60 ± 2	1.0 ± 0.9	1.0 ± 1.0	38 ± 1
	30	29 ± 1	13 ± 1	2.0 ± 0.6	56 ± 1
Cu/3	5	31 ± 3	15 ± 2	1.0 ± 1.0	53 ± 2
	30	24 ± 1	31 ± 1	7.0 ± 0.4	38.0 ± 0.3

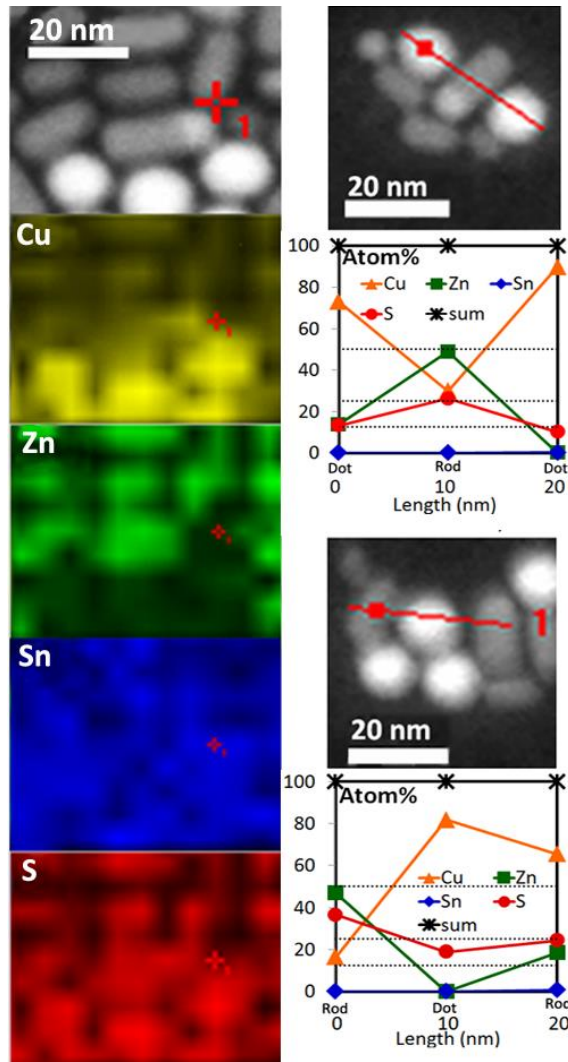[a]$[Cu]_T = 48$ mM, $[Zn]_T = 24$ mM, $[Sn]_T = 24$ mM, $[S]_T = 0.40$ M (see text).

Figure 5. EDX elemental mapping (left) and line scans (right) on samples made with one third of the zinc loading ('Zn/3') show rods are zinc-rich and dots are copper-rich. Dotted lines correspond to the theoretical CZTS composition (25 atom% Cu, 12.5 atom% Zn and Sn each, and 50 atom% S).
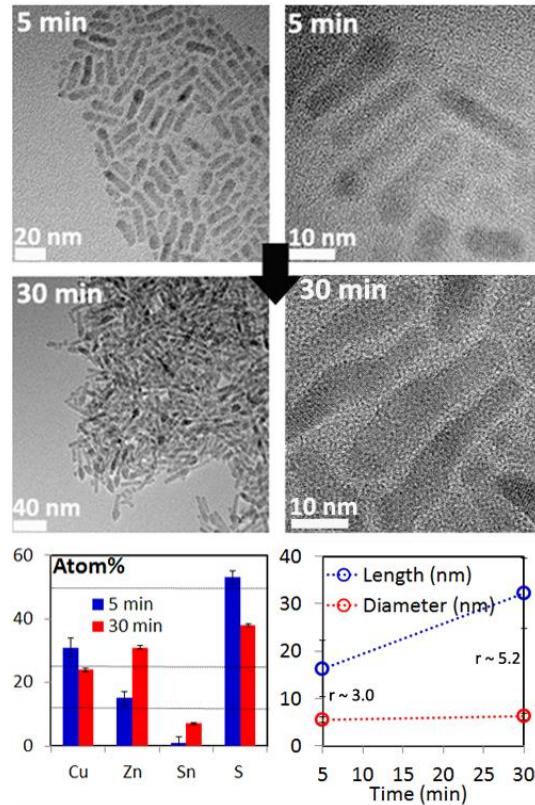
Figure 6. Time evolution of CZTS nanorods made with a 2/3:1:1 Cu:Zn:Sn cationic precursor ratio ('Cu/3' conditions above): TEM images of CZTS nanorods after 5 min (top) and 30 min (middle). EDX composition (bottom left) and aspect ratio (bottom right) as the reaction progresses. Dotted lines correspond to the theoretical CZTS composition (25 atom% Cu, 12.5 atom% Zn and Sn each, and 50 atom% S).

Conclusions

In summary, we have demonstrated that wurtzite CZTS nanorods synthesized using stoichiometric amounts of commercially available cationic precursors contain marked composition gradients along their axes. These hexagonal CZTS nanorods are characterized by a copper-rich end, an opposite zinc-rich end, and low tin content throughout. Non-stoichiometric syntheses, in which we varied the loading of the cationic precursors, along with time evolution experiments showed the that the reactivity of the three cationic precursors and relative rate of nucleation of the corresponding metal sulfides decrease as: $Cu(C_5H_7O_2)_2$ (most reactive) > $Zn(CH_3CO_2)_2$ > $Sn(CH_3CO_2)_4$ (least

reactive). Under stoichiometric conditions, these reactivity differences lead to sequential nucleation events and axial composition gradients: Seeds made of copper sulfides quickly form first by homogeneous nucleation, followed by heterogeneous (epitaxial) nucleation of zinc and tin sulfides.

Decreasing the loading of the most reactive (copper) precursor increases the nanorods' aspect ratio by lowering the rate of nucleation of copper sulfides. This allows the three metal precursors to nucleate at more comparable rates, producing significantly longer CZTS nanorods with a more constant elemental composition along their axis. In contrast, increasing the loading of copper precursor, or changing the loading of zinc or tin precursors either leads to low aspect ratio (dots) and/or phase segregated nanocrystals. Thus, we have shown that cationic precursor loading predictably affects the morphology (dots vs. rods) and degree of axial phase segregation of anisotropic CZTS nanocrystals. These discoveries will improve our ability to fabricate CZTS nanostructures for photovoltaics and photocatalysis. More generally, they will aid our understanding of -and ability to control- phase segregation in complex compound semiconductors such as quaternary CZTS.

Acknowledgments

References

[1] Vela, J. Molecular Chemistry to the Fore: New Insights into the Fascinating World of Photoactive Colloidal Semiconductor Nanocrystals. *J. Phys. Chem. Lett*. **2013**, *4*, 653–668.

[2] Zhou, Y.; Zhou, W.; Li, M.; Du, Y.; Wu, S. Hierarchical Cu_2ZnSnS_4 Particles for a Low-Cost Solar Cell: Morphology Control and Growth Mechanism. *J. Phys. Chem. C* **2011**, *115*, 19632–19639.

[3] Pundsack, T. J.; Chernomordik, B.; Beland, A.; Aydil, E.; Blank, D. Excited-State Dynamics in CZTS Nanocrystals. *J. Phys Chem. Lett.* **2013**, *4*, 2711–2714.

[4] Miyauchi, M.; Hanayama, T.; Atarashi, D.; Sakai, E. Photoenergy Conversion in p-Type Cu_2ZnSnS_4 Nanorods and n-Type Metal Oxide Composites. *J. Phys. Chem. C* **2012**, *116*, 23945–23950.

[5] Li, M.; Zhou, W.; Guo, J.; Zhou, Y.; Hou, Z.; Jiao, J. Zhou, Z.; Du, Z.; Wu, S. Synthesis of Pure Metastable Wurtzite CZTS Nanocrystals by Facile One-Pot Method. *J. Phys. Chem. C* **2012**, *116*, 26507–26516.

[6] Wadia, C.; Alivisatos, A. P.; Kammen, D. M. Materials Availability Expands the Opportunity for Large-Scale Photovoltaics Deployment. *Environ. Sci. Technol.* **2009**, *43*, 2072–2077.

[7] Hossain, M. Prospects of CZTS Solar Cells from the Prospective of Material Properties, Fabrication Methods and Current Research Challenges. *Chalc. Lett.* **2012**, 9, 231−242.

[8] Habas, S. E.; Platt, H. A. S; Van Hest, M.; Ginley, D. Low-Cost Inorganic Solar Cells: From Ink to Printed Device. *Chem. Rev.* **2010**, *110*, 6571−6594.

[9] Jiang, M.; Yan, X. Cu_2ZnSnS_4 Thin Film Solar Cells: Present Status and Future Prospects. In *Solar Cells-Research and Application Prospectives*; Morales-Acevedo, M.; InTech, **2013**, pp. 107–143.

[10] Suryawanshi, M.; Agawane, G. L.; Bhosale, S.M.; Shin, S. W.; Patil, P.S.; Kim, J.H.; Moholkar, A.V. CZTS Based Thin Solar Films: A Status Review. *Mater. Tech.: Adv. Perf. Mater*. **2013**, *28*, 98−109.

[11] Guo, Q.; Hillhouse, H.; Agrawal, R. Synthesis of Cu_2ZnSnS_4 Nanocrystal Ink and Its Use for Solar Cells. *J. Am. Chem. Soc.* **2009**, *131*, 11672−11673.

[12] Steinhagen, C.; Panthani, M.; Akhavan, V.; Goodfellow, B.; Koo, B.; Korgel, B. A. Synthesis of Cu_2ZnSnS_4 Nanocrystals for Use in Low-Cost Photovoltaics. *J. Am. Chem. Soc.* **2009**, *131*, 12554–12555.

[13] Xu, J.; Yang, X.; Yang, Q.; Wong, T.; Lee, C. Cu_2ZnSnS_4 Hierarchical Microspheres as an Effective Counter Electrode Material for Quantum Dot Sensitized Solar Cells. *J. Phys. Chem. C.* **2012**, *116*, 19718−19723.

[14] Fairbrother, A.; García-Hemme, E.; Izquierdo-Roca, V.; Fontane, X.; Pulgarin-Agudelo, F.; Vigil-Galan, O.; Perez-Rodriguez, A.; Saucedo, E. Development of a Selective Chemical Etch to Improve the Conversion Efficiency of Zn-Rich Cu_2ZnSnS_4 Solar Cells. *J. Am. Chem. Soc.* **2012**, *134*, 8018−8021.

[15] Guo, Q.; Kim, S. J.; Kar, M.; Shafarman, W.; Birkmire, R.; Stach, E.; Agrawal, R.; Hillhouse, H.W. Development of $CuInSe_2$ Nanocrystal and Nanoring Inks for Low-Cost Solar Cells. *Nano Lett.* **2008**, *8*, 2982−2987.

[16] Zou, C.; Zhang, L. J.; Lin, D.; Yang, Y.; Li, Q.; Xu, X.; Chen, X.; Huang, S. Facile Synthesis of Cu_2ZnSnS_4 Nanocrystals. C*rystEngComm.* **2011**, *13*, 3310−3313.

[17] Singh, A.; Geaney H.; Laffir, F.; Ryan, K. Colloidal Synthesis of Wurtzite Cu_2ZnSnS_4 Nanorods and Their Perpendicular Assembly. *J. Am. Chem. Soc.* **2012**, *134*, 2910−2913.

[18] Zhuang, Z. B.; Peng, Q.; Zhang, B.; Li, Y. Controllable Synthesis of Cu_2S Nanocrystals and Their Assembly into a Superlattice. *J. Am. Chem. Soc* .**2008**, *130*, 10482−10483.

[19] Riha, S. C.; Parkinson, B. A.; Prieto, A. L. Compositionally Tunable $Cu_2ZnSn(S_{1-x}Se_x)_4$ Nanocrystals: Probing the Effect of Se-Inclusion in Mixed Chalcogenide Thin Films. *J. Am. Chem. Soc.* **2011***, 133*, 15272−12575.

[20] Norako, M. E.; Greaney, M. J.; Brutchey, R. L. Synthesis and Characterization of Wurtzite-Phase Copper Tin Selenide Nanocrystals. *J. Am. Chem. Soc.* **2012**, *134*, 23−26.

[21] Lu, X.; Zhuang, Z.; Peng, Q.; Li, Y. Wurtzite Cu_2ZnSnS_4 Nanocrystals: a Novel Quaternary Semiconductor. *Chem. Commun.* **2011**, *47*, 3141−3143.

[22] Shavel, A.; Arbiol, J.; Cabot, A. Synthesis of Quaternary Chalcogenide Nanocrystals: Stannite $Cu_2Zn_xSn_ySe_{1+x+2y}$. *J. Am. Chem. Soc.* **2010**, *132*, 4514−4515.

[23] Larsen, T. H.; Sigman, M.; Ghezelbash, A.; Doty, R.C.; Korgel, B.A. Solventless Synthesis of Copper Sulfide Nanorods by Thermolysis of a Single Source Thiolate-Derived Precursor. *J. Am. Chem. Soc.* **2003**, *125*, 5638−5639.

[24] Guo, Q.; Ford, G. M.; Yang, W.; Walker, B. C.; Stach, E. A.; Hillhouse, H. W.; Agrawal, R. Fabrication of 7.2% Efficient CZTSSe Solar Cells Using CZTS Nanocrystals. *J. Am. Chem. Soc.* **2010***, 132*, 17384−17386.

[25] Deka, S.; Genovese, A.; Zhang, Y.; Miszta, K.; Bertoni, G.; Krahne, R.; Giannini, C.; Manna, L. Phosphine Free Synthesis of p-Type Copper(I) Selenide Nanocrystals in Hot Coordinating Solvents. *J. Am. Chem. Soc.* **2010**, *132*, 8912−8914.

[26] Ramasamy, K; Malik, M.; O'Brien, P. Routes to Copper Zinc Tin Sulfide Cu_2ZnSnS_4: A Potential Material for Solar Cells. *Chem. Commun.* **2012**, *48*, 5703−5714.

[27] Riha, S. C.; Parkinson, B. A.; Prieto, A. L. Solution-Based Synthesis and Characterization of Cu_2ZnSnS_4 Nanocrystals. *J. Am. Chem. Soc.* **2009**, *131*, 12054−12055.

[28] Zoppi, G.; Forbes, I.; Miles, R. W.; Dale, P. J. Scragg, J. J.; Peter, L. M. Cu₂ZnSnSe₄ in Film Solar Cells Produced by Selenisation of Magnetron Sputtered Precursors. *Prog. Photovoltaics*, **2009**, *17*, 315−319.

[29] Regulacio, M.; Ye, C.; Lim, S. H.; Bosman, M.; Ye, E.; Chen, S.; Xu, Q.; Han, M. Colloidal Nanocrystals of Wurtzite-Type Cu₂ZnSnS₄: Facile Noninjection Synthesis and Formation Mechanism. *Chem. Eur. J.* **2012***, 18*, 3127–3131.

[30] Huang, S.; Luo, W.; Zou, Z. Band Positions and Photoelectrochemical Properties of Cu₂ZnSnS₄ Thin Films by the Ultrasonic Spray Pyrolysis Method. *J. Phys. D: Appl. Phys.* **2013,** *46*, 235108–235114.

[31] Fan, F.; Wu, L.; Ming, G.; Liu, G.; Wang, Y.; Yu, S.; Chen, S.; Wang, L.; Gong, X. Composition-and Band-Gap-Tunable Synthesis of Wurtzite-Derived Cu₂ZnSn(S₁₋ₓSeₓ)₄ Nanocrystals: Theoretical and Experimental Insights. *ACS Nano* **2013**, 7, 1454–1463.

[32] Liu, W.; Guo, B.; Mak, C.; Li, A.; Wu, X.; Zhang, F. Facile Synthesis of Ultrafine Cu₂ZnSnS₄ Nanocrystals by Hydrothermal Method for Use in Solar Cells. *Thin Solid Films* **2013,** *535*, 39–43.

[33] Sarswat, P.; Free, M. An Investigation of Rapidly Synthesized Cu₂ZnSnS₄ Nanocrystals. *J. Cryst. Growth,* **2013**, *372*, 87–94.

[34] Zhang, W.; Zhai, L. Solution-based Synthesis of Wurtzite Cu₂ZnSnS₄ Nanoleaves Introduced by α-Cu₂S Nanocrystals as Catalyst. *Nanoscale* **2013,** *5*, 8114−8121.

[35] Jiang, C.; Lee, J. S.; Talapin, D. V. Soluble Precursors for CuInSe₂ CuIn₁₋ₓGaₓSe₂ and Cu₂ZnSn(S,Se)₄ Based on Colloidal Nanocrystals and Molecular Metal Chalcogenide Surface Ligands. *J. Am. Chem. Soc.* **2012**, *134*, 5010−5013.

[36] Fischereder, A.; Rath, T.; Hass, W.; Amenitsch, H.; Albering, J.; Meischler, D.; Larissegger, S.; Edler, M.; Saf, R.; Hofer, F.; Trimmel, G. Investigation of Cu₂ZnSnS₄ Formation from Metal Salts and Thioacetamide. *Chem. Mater.* **2010**, *22*, 3399–3406.

[37] Chane-Ching, J. Y.; Gillorin, A.; Zaberca, O.; Balocchi, A.; Marie, X. Highly-Crystallized Quaternary Chalcopyrite Nanocrystals Via a High-Temperature Dissolution-Reprecipitation Route. *Chem. Comm.* **2011**, *47*, 5229–5231.

[38] Talapin, D. V.; Lee, J.-S.; Kovalenko, M.; Shevchenko, E. V. Prospects of Colloidal Nanocrystals for Electronic and Optoelectronic Applications. *Chem. Rev.* **2010***, 110*, 389–458.

[39] Sun, B.; Marx, E.; Greenham, N. C. Photovoltaic Devices Using Blends of Branched CdSe Nanoparticles and Conjugated Polymers. *Nano Lett.* **2003**, *3*, 961–963.

[40] Ruberu, T. P. A.; Vela, J. Expanding the One-Dimensional CdS-CdSe Composition Landscape: Axially Anisotropic CdS₁₋ₓSeₓ Nanorods. *ACS Nano* **2011**, *5*, 5775–5784.

[41] Ruberu. T. P. A.; Albright, H. R.; Ward, B.; Cisneros, J.; Fan, J.; Vela, J. Molecular Control of the Nanoscale: Effect of Phosphine-Chalcogenide Reactivity on CdS-CdSe Nanocrystal Composition and Morphology. *ACS Nano* **2012**, *6*, 5348–5359.

[42] Nagoya, A.; Asahi, R.; Wahl, R.; Kresse, G. Defect Formation and Phase Stability of Cu_2ZnSnS_4 Photovoltaic Material. *Phys. Rev. B* **2010**, *81*, 113202–1–4.

[43] Guo, Y.; Alvarado, S. R.; Barclay, J. D.; Vela, J. Shape-Programmed Nanofabrication: Understanding the Reactivity of Dichalcogenide Precursors. *ACS Nano* **2013**, *7*, 3616–3626.

[44] Schorr, S.; Mainz, R.; Moenig, H.; Lauermann, I.; Baer, M. The Complex Material Properties of Chalcopyrite and Kesterite Thin-Film Solar Cell Absorbers Tackled by Synchrotron-Based Analytics. *Prog Photovoltaics* **2012,** *20*, 557-567.

[45] Just, J.; Luetzenkirchen-Hecht, D.; Frahm, R.; Shorr, S.; Unold, T. Determination of Secondary Phases in Kesterite Cu_2ZnSnS_4 Thin Films by X-Ray Absorption Near Edge Structure Analysis. *Appl. Phys. Lett.* **2011,** *99*, 262105–1–3.

[46] Jost, S.; Shurr, R.; Holzing, A.; Hergert, F.; Hock, R.; Purwins, M.; Palm, J. The Formation of the Thin-Film Solar Cell Absorber $CuInS_2$ by Annealing of Cu-In-S Stacked Elemental Layer Precursors- A Comparison of Selenisation and Sulfurisation. *Thin Solid Films* **2009**, *517*, 2136–2139.

[47] Kundu, J.; Pradhan, D., Influence of Precursor Concentration, Surfactant, and Temperature on the Hydrothermal Synthesis of CuS: Structural, thermal, and Optical Properties. *New J. Chem.* **2013,** *37*, 1470–1478

[48] Wang, M.; Batabyal, S.; Li, Z.; Li, D.; Mhaisalkar, S.G.; Lam, Y. Nanocrystalline Copper Indium Selenide ($CuInSe_2$) Particles for Solar Energy Harvesting. *RSC Adv.* **2013,** *3*, 9829–9834.

Appendix of supporting information

Materials: Copper (II) acetylacetonate (99.99%), 1-dodecanethiol (98+%), tert-dodecylmercaptan (98.5%) and trioctylphosphine oxide (TOPO) (99%) were purchased from Sigma Aldrich; zinc (II) acetate dihydrate (98+%) from Strem Chemicals; tin (IV) acetate (98%) from Alfa Aesar; and 1-Octadecene (90%) from Acros. Materials were used as received.

Synthesis: CZTS nanorods were made by a modified literature procedure. In a typical synthesis, 0.5mmol copper (II) acetylacetonate, 0.25 mmol zinc (II) acetate dihydrate, 0.25 mmol tin (IV) acetate, and 1.75 mmol trioctylphosphine oxide (TOPO) were mixed with 5 mL of 1-ODE in a three-neck, round bottom flask and evacuated at room temperature for 30 min. The solution was then heated to 120°C, where a mixture of 0.52 mmol 1- DDT and 3.72 mmol t-DDT was quickly injected. The reaction mixture was then heated to 210°C for 30 min with continuous stirring. The solution was allowed to cool to 80°C, at which point, 1.5 mL anhydrous toluene was injected to quench the reaction. The nanorods were washed several times with a mixture of acetonitrile, ethanol, and methanol, and centrifuged at 5000 RPM for 8 minutes, yielding a dark brown/black product. The loading of precursor metals was varied by 1/3 or 3× molar amounts based on the original CZTS synthesis.

Structural Characterization: *X-Ray Diffraction*. Powder X-ray diffraction (XRD) data were measured using Cu KR radiation on a Rigaku Ultima IV diffractometer. *Transmission Electron Microscopy*. Transmission electron microscopy (TEM) was conducted on carbon-coated nickel grids using a FEI Technai G2F20 field emission scanning transmission electron microscope (STEM) at 200 kV (point-to-point resolution <0.25 nm, line-to-line resolution <0.10 nm). Nanorods' elemental axial composition was

characterized by energy-dispersive x-ray spectroscopy (EDX) line scans in STEM mode. *Particle analysis*. Dimensions were measured manually using ImageJ. Size measurements and particle statistics were obtained for >100 particles. Average sizes are reported along ± 1 standard deviation.

Optical Characterization: Absorption spectra were measured with a photodiode array Agilent 8453 UV-Vis-NIR spectrophotometer. Solvent absorption was subtracted from all spectra.

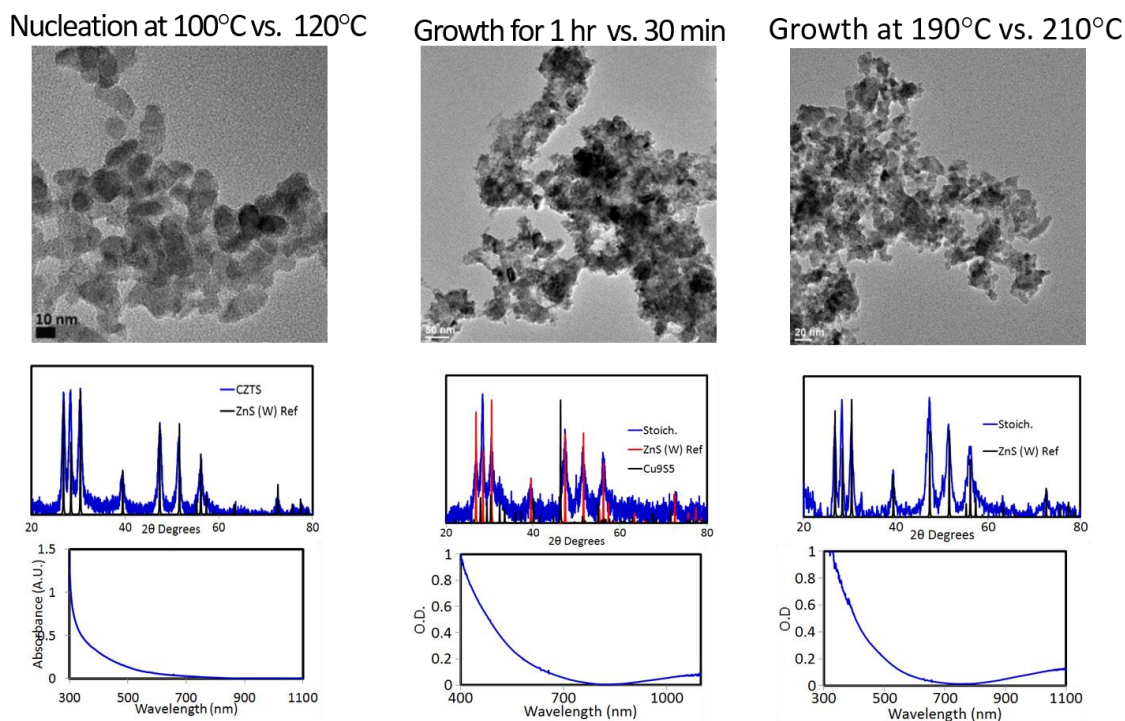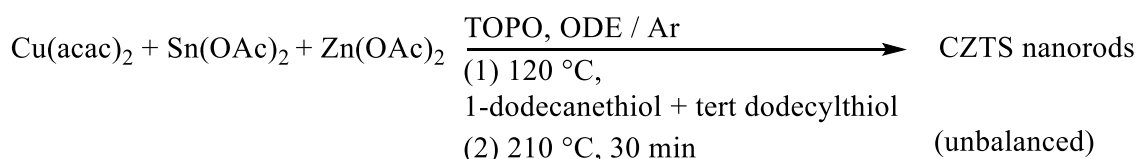**Scheme S1.** General synthesis route for formation of CZTS nanorods.

$$Cu(acac)_2 + Sn(OAc)_2 + Zn(OAc)_2 \xrightarrow[\substack{(1)\ 120\ °C,\\ \text{1-dodecanethiol + tert dodecylthiol}\\ (2)\ 210\ °C,\ 30\ min}]{\text{TOPO, ODE / Ar}} \text{CZTS nanorods}$$

(unbalanced)

Figure S1. Changing reactions conditions to optimize CZTS synthesis.

Sample		Cu	Zn	Sn	S
CZTS	Avg. Atom%	32 ± 1	11 ± 1	12 ± 1	45 ± 2
	Avg. Ratio	3	1	1	4
Cu/3	Avg. Atom%	28 ± 3	12 ± 3	6 ± 2	54 ± 2
	Avg. Ratio	5	2	1	9
3×Cu	Avg. Atom%	77 ± 2	1 ± 1	1 ± 0.4	21 ± 0.4
	Avg. Ratio	57	1	1	16
Zn/3 **Rods**	Avg. Atom%	10 ± 2	56 ± 4	1 ± 2	33 ± 2
	Avg. Ratio	0.2	1	0.01	1
Zn/3 **Dots**	Avg. Atom%	70 ± 3	19 ± 3	0	11 ± 0.4
	Avg. Ratio	4	1	0	1
3×Zn	Avg. Atom%	52 ± 1	19 ± 1	6 ± 1	24 ± 1
	Avg. Ratio	9	3	1	4
Sn/3	Avg. Atom%	59 ± 0.8	8 ± 0.4	3 ± 0.3	30 ± 0.3
	Avg. Ratio	20	3	1	10
3×Sn	Avg. Atom%	28 ± 0.4	16 ± 0.3	15 ± 0.3	41 ± 0.2
	Avg. Ratio	2	1	1	3

Table S1. EDX average atom% and ratios for CZTS with varying precursor loadings.

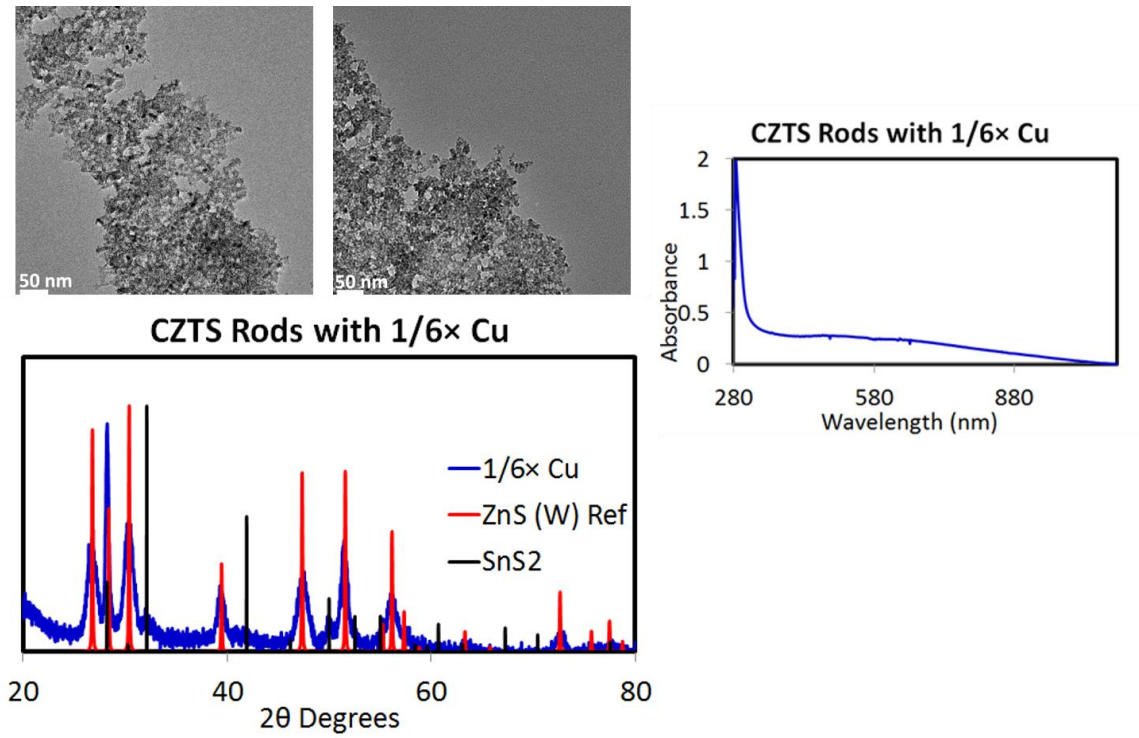**Figure S2**. Synthesis of CZTS nanorods with 1/6×Cu precursor loading.
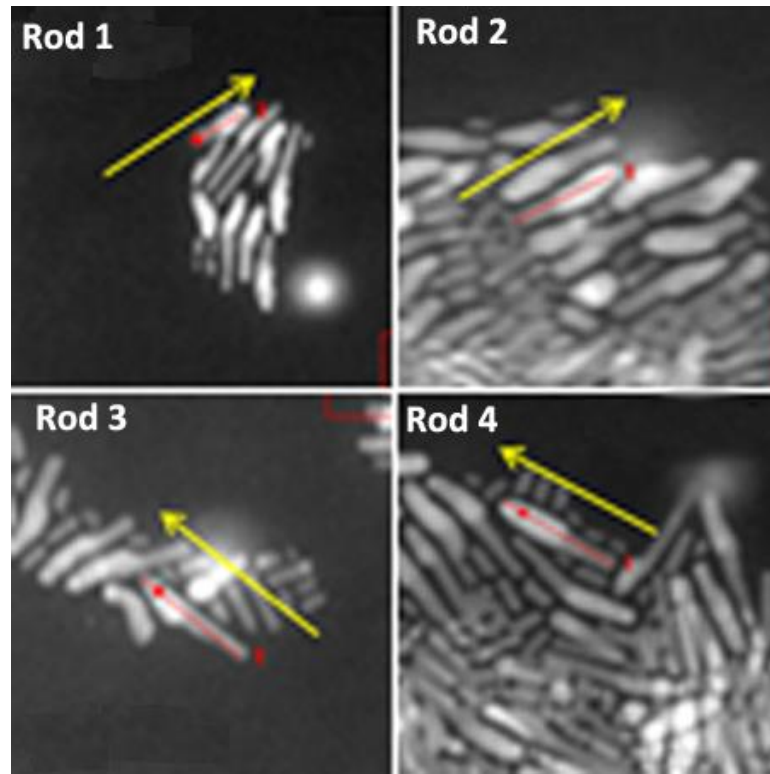
Figure S3. Dark field TEM images of EDX line scans of sample with Cu/3 precursor loading.
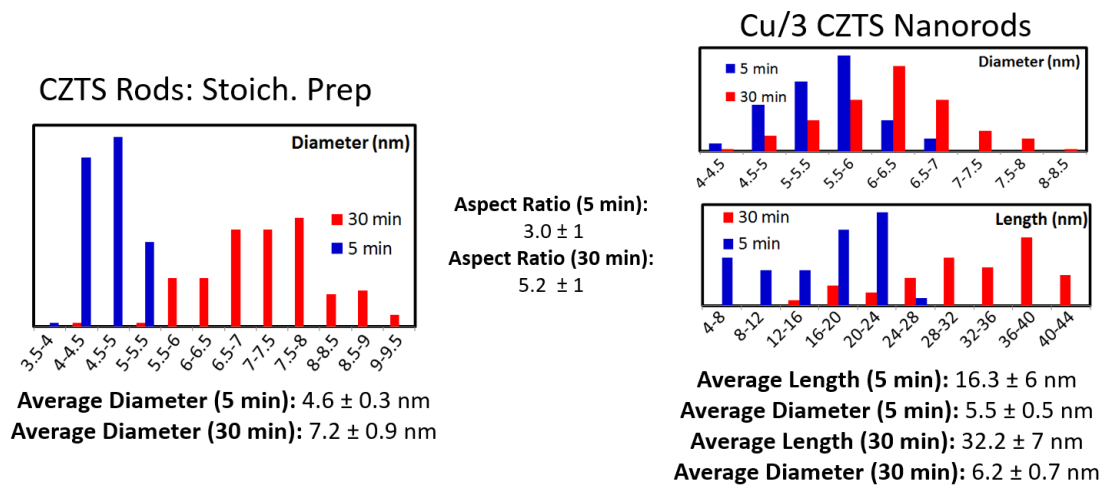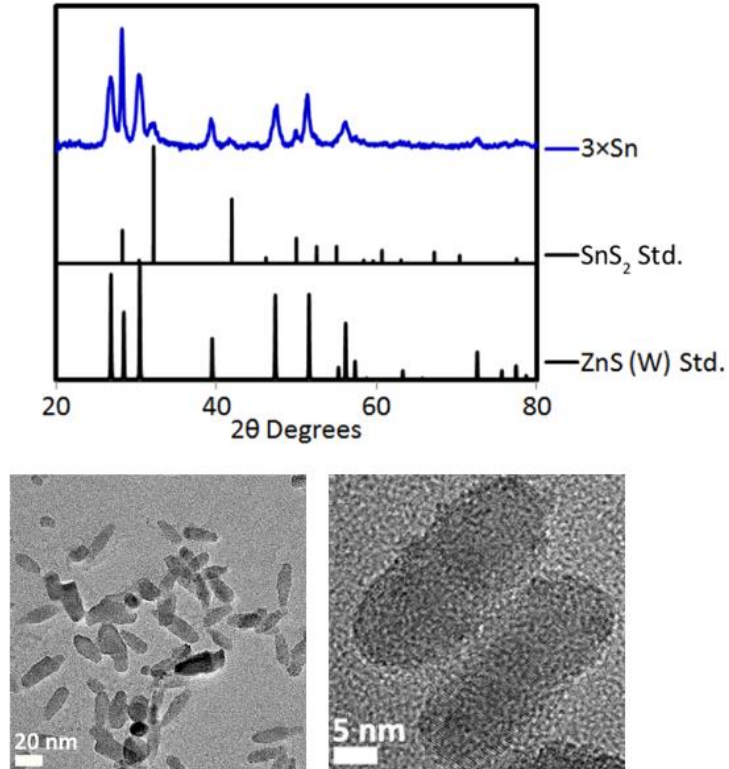

Figure S4. Time evolution studies using TEM dimensions on stoichiometric and Cu/3 nanorod syntheses. Showed nanorods grow longer and wider over time.

Average Length: 32.6 ± 6 nm
Average Diameter: 11.1 ± 1 nm
Aspect Ratio: 2.9

Figure S5. Characterization of 3×Sn precursor loading. PXRD (top) shows wurtzite pattern and SnS₂ impurity. TEM (bottom) shows nanorod morphology.
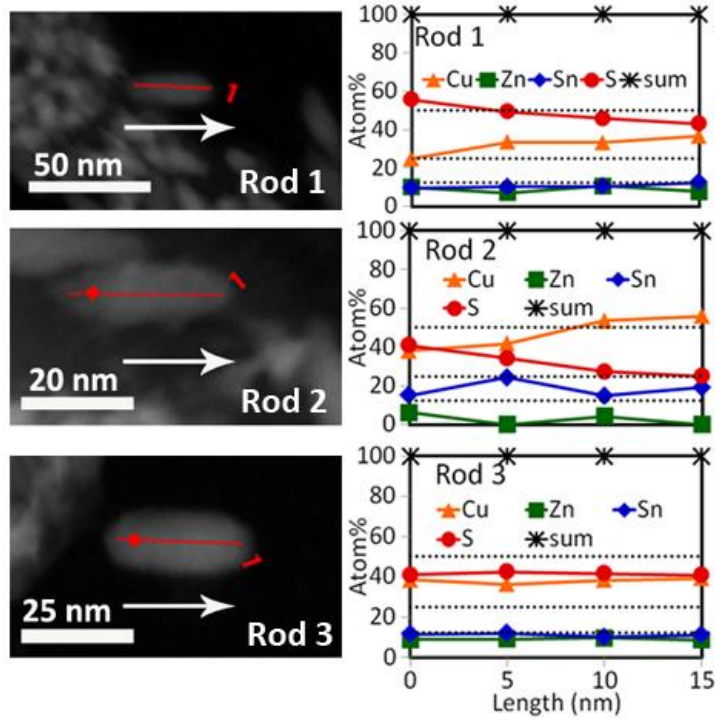
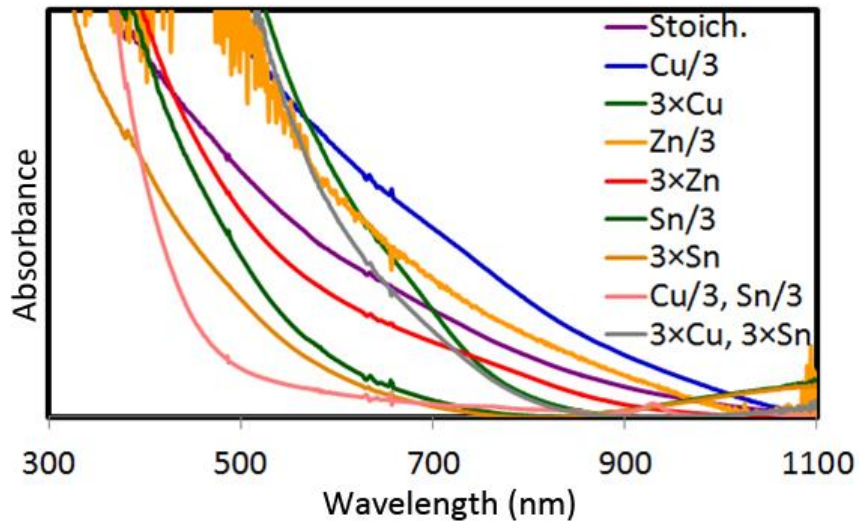**Figure S6.** EDX line scans of 3×Sn precursor loading shows less pronounced composition gradients.

Figure S7. Solution phase optical absorption spectra of CZTS with different precursor loadings.
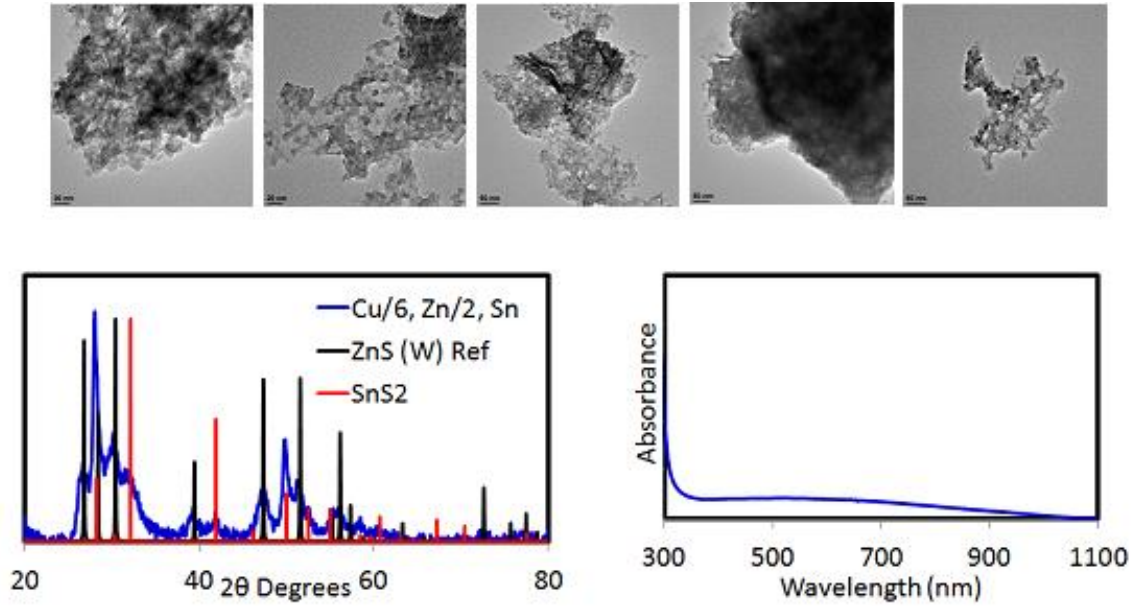
Figure S8. Characterization of sample with Cu/6, Zn/2 and tin precursor loading, TEM (upper), PXRD (lower left) and UV-Visible solution phase absorbance (lower right).

CHAPTER 3

CU₂ZNSNS₄ NANORODS DOPED WITH TETRAHEDRAL, HIGH SPIN TRANSITION METAL IONS: MN²⁺, CO²⁺, AND NI²⁺

Michelle J. Thompson, Kyle J. Blakeney, Sarah D. Cady, Malinda D. Reichert,

Joselyn Del Pilar-Albaladejo, Seth T. White, Javier Vela

Abstract

Because of its useful optoelectronic properties and the relative abundance of its elemental components, the quaternary semiconductor Cu_2ZnSnS_4 (CZTS) has garnered considerable interest in recent years. In this work, we dope divalent, high spin transition metal ions ($M^{2+} = Mn^{2+}$, Co^{2+}, Ni^{2+}) into the tetrahedral Zn^{2+} sites of wurtzite CZTS nanorods. The resulting $Cu_2M_xZn_{1-x}SnS_4$ (CMTS) nanocrystals retain the hexagonal crystalline structure, elongated morphology, and broad visible light absorption profile of the undoped CZTS nanorods. Electron paramagnetic resonance (EPR), X-ray photoelectron spectroscopy (XPS) and Fourier transform infrared (FTIR) spectroscopy help corroborate the composition and local ion environment of the doped nanocrystals. EPR shows that, similarly to $Mn_xCd_{1-x}Se$, washing $Cu_2Mn_xZn_{1-x}SnS_4$ nanocrystals with trioctylphosphine oxide (TOPO) is an efficient way to remove excess Mn^{2+} ions from the particle surface. XPS and FTIR of as isolated and thiol-washed samples show that, in contrast to binary chalcogenides, $Cu_2Mn_xZn_{1-x}SnS_4$ nanocrystals aggregate not through

dichalcogenide bonds, but through excess metal ions crosslinking the sulfur-rich surfaces of neighboring particles. Our results may help in expanding the synthetic applicability of CZTS and CMTS materials beyond photovoltaics and into the fields of spintronics and magnetic data storage.

Introduction

Colloidal semiconductor nanocrystals have garnered great interest due to their potential applications in solar energy harvesting, light-emitting devices, and as optical probes for imaging and tracking.[1,2] Among semiconductor materials, Cu_2ZnSnS_4 (CZTS) and, potentially also transition metal-doped $Cu_2M_xZn_{1-x}SnS_4$ ($M = Mn^{2+}, Co^{2+}, Ni^{2+}$), are promising for solar cell applications due to their direct band gap of ~1.5 eV, large absorption coefficient, and abundantly distributed and relatively biocompatible elements.[3-17]

Incorporating transition metals into semiconductors is a burgeoning field of research. Doped semiconductor nanocrystals have been heavily studied for energy transfer and sensing, magnetic and optoelectronic devices, and data storage.[12,18-22] Some of the most explored metal-doped nanoscale semiconductors include Mn^{2+}-doped ME nanocrystal quantum dots ($M = Zn, Cd; E = S$ or Se),[23-25] nanoribbons,[2] and CdS/ZnS core-shells.[26] Beyond manganese(II), there has been a focused effort to dope different transition metal ions into a variety of semiconductors, including Ni^{2+} into ZnE, Co^{2+} or Ni^{2+} into ZnO, Co^{2+} into TiO_2, and Co^{2+} into CdE ($E = S$ or Se).[27-35]

Similar to these systems, incorporating tetrahedrally coordinated, high spin, first row transition metal ions into the CZTS lattice could lead to new magnetically- and optically–active earth abundant materials with potential applications in the field of

information technology, specifically in spintronics and magnetic data storage.[36,37] However, in contrast to doped II-VI materials, there are few reports on doping Mn^{2+}, Co^{2+}, or Ni^{2+} into the CZTS lattice. These reports focused mainly on optical properties of the fully (rather than the partially) substituted "CMTS" materials, such as Cu_2CoSnS_4,[13-15,38] Cu_2MnSnS_4,[39,40] and Cu_2NiSnS_4 nanocrystals.[16,17,41]

Building on the controllable synthesis of colloidal semiconductor nanocrystals,[42-47] we and others recently manipulated the composition and morphology of CZTS nanorods by adjusting the relative reactivity of the molecular precursors used.[48-50] We also utilized this method to synthesize photocatalytic CZTS-Au heterostructures.[51] Here, we use this platform to dope first-row, transition metal ions into $Cu_2M_xZn_{1-x}SnS_4$ nanorods (M = Mn^{2+}, Co^{2+}, Ni^{2+}).

Experimental

Materials. Copper(II) acetylacetonate (99.99%), 1-dodecanethiol (98+%), tert-dodecylthiol (98.5%), nickel(II) acetate tetrahydrate (99+%), cobalt(II) tetrahydrate (99+%) and trioctylphosphine oxide (TOPO) (99%) were purchased from Sigma Aldrich; zinc(II) acetate dihydrate (98+%), and manganese(II) acetate tetrahydrate (99+%) from Strem Chemicals; tin(IV) acetate (98%) from Alfa Aesar; and 1-octadecene (ODE) (90%) from Acros. All materials were used as received.

Synthesis. CZTS nanorods were made by a modified literature procedure.[48,52] In a typical synthesis, copper(II) acetylacetonate (0.5 mmol), zinc(II) acetate dihydrate and/or dopant ion precursor (manganese(II) acetate tetrahydrate, nickel(II) acetate tetrahydrate, cobalt(II) tetrahydrate) (0.25 mmol), tin(IV) acetate (0.25 mmol), and TOPO (1.75 mmol) were mixed with ODE (5 mL) in a three-neck, round bottom flask and evacuated at room

temperature for 30 min. The flask was heated to 120 °C, and a mixture of 1-dodecanethiol (0.52 mmol) and tert-dodecylthiol (3.72 mmol) quickly injected. After additional heating to 210 °C for 30 min with continuous stirring, the solution was allowed to cool to 80 °C, and anhydrous toluene (1.5 mL) added. Brown/black colored solids (nanocrystals) were isolated by repeated precipitation with a mixture of acetonitrile, ethanol and methanol, and centrifugation at 5000 rpm for 8 min, followed by re-dissolution in toluene. *TOPO Wash.* To remove excess manganese ions from the surface of the nanocrystals, we employed a trioctylphosphine oxide (TOPO) 'wash'.[53,54] Briefly, we added a small amount of TOPO to the nanoparticles, sonicated the mixture for 10 minutes, and then washed again twice with methanol and ethanol. *Thiol Wash.* In order to reduce nanoparticle aggregation, we employed a wash using excess thiols. Briefly, approximately 0.4 mL of a 1:7 mixture of 1-dodecanethiol and tert-dodecylthiol was added to approximately 5 mL of particles (half to one whole batch) dispersed in toluene. After sonication for 1 h, the particles were washed once with ethanol and methanol and centrifuged at 5000 rpm for 8 min.

Characterization. *Powder X-ray diffraction* (XRD) were measured using Cu Kα radiation on a Rigaku Ultima IV diffractometer. A standard pattern of wurtzite (hexagonal) ZnS was used in lieu of that of wurtzite CZTS (unknown). *Transmission Electron Microscopy* (TEM) was conducted on carbon-coated nickel or gold grids using a FEI Tecnai G2F20 field emission scanning transmission electron microscope (STEM) at 200 kV (point-to-point resolution <0.25 nm, line-to-line resolution <0.10 nm). The nanorods' axial elemental composition was characterized using energy-dispersive spectroscopy (EDX) line scans in STEM mode. Atom% values were determined by

averaging five EDX scans of representative areas within each sample. *Particle sizes* (dimensions) and statistics (>100 particles) were measured manually using ImageJ. Average sizes are reported with ± 1 standard deviations. *Electron Paramagnetic Resonance* (EPR) spectra were measured using an ELEXYS E580 EPR Spectrometer (Bruker BioSpin) equipped with an SHQE resonator and an Oxford ESR900 cryostat. The samples were dispersed in toluene, placed in a 4 mm quartz tube, and frozen in liquid N_2 prior to insertion into the cryostat. Low temperature spectra were measured at 10 K. Typical spectra were acquired with a sweep width of 5000 G, 2048 points, 8 G amplitude modulation and 1.986 mW microwave power. Simulations were performed in the computational package EasySpin, which runs on the Matlab platform, using the 'pepper' function. Although the full spin Hamiltonian employed in the EasySpin simulations contains six terms, only three are used in our simulations: the Electron Zeeman interaction (EZI), Zero-Field interaction (ZFI), and Nuclear Zeeman interaction (NZI), shown below:[55]

$$\widehat{H} = \sum_i \left[\widehat{H}_{EZI}(i) + \widehat{H}_{ZFI}(i)\right] + \sum_k \widehat{H}_{NZI}(i)$$

X-ray photoelectron spectroscopy (XPS) was measured with a Physical Electronics 5500 Multitechnique system using a standard Al Kα source. Analysis spot size was 1×1 mm and the sample was mounted on 2-sided tape (3M). Binding energies were referenced to the C 1s peak at 285.0 eV. *Optical absorption spectra* were measured with a photodiode array Agilent 8453 UV-Vis-NIR spectrophotometer. Solvent absorption was subtracted from all spectra. Tauc plots were generated by calculating $(\alpha h\upsilon)^2$ because

CZTS has a direct band gap. The band gap was estimated by extropolating the most linear portion of the graph.[7,56] *Diffuse reflectance* spectra of solid films were measured with a SL1 Tungsten Halogen lamp (vis-IR), a SL3 Deuterium Lamp (UV), and a BLACK-Comet C-SR-100 Spectrometer. Samples were prepared by drop-casting toluene solutions onto glass. *Fourier Transform Infrared Spectroscopy* (FTIR) spectra (4000-400 cm^{-1}) were measured in KBr pellet form and ambient temperature using a Bruker Tensor 37 Fourier transform infrared spectrophotometer.

Results and discussion

Literature reports show that fully substituted ("parent") Cu_2MSnS_4 (CMTS) compounds normally adopt either the kesterite ($I\bar{4}$) or stannite ($I\bar{4}2m$) crystal structure (M = Zn^{2+}, Mn^{2+}, Co^{2+}, Ni^{2+}).[9,10,13] The metal ion positions in these structures, their magnetic interactions, and M-M distances, have been characterized and reported in previous magnetism studies.[40] Partially substituting (doping) $Cu_2M_xZn_{1-x}SnS_4$ nanorods (M = Mn^{2+}, Co^{2+}, Ni^{2+}) with a wurtzite crystal structure ($P6_3mc$) could lead to additional and interesting magnetic properties.[16,57] Simple considerations predict that doping and even complete solid solutions are possible over the whole $Cu_2M_xZn_{1-x}SnS_4$ composition range ($0 \leq x \leq 1$). Across these series, available lattice parameters differ little, by less than 1%, as do ionic radii for the four-coordinate Zn^{2+}, Mn^{2+}, Co^{2+} and Ni^{2+}, by less than 10% (Table 1).[58]

Table 1. Structural Parameters of CZTS and Transition Metal Substituted (CMTS) Materials.

Compound	Lattice Parameters (structure)[a]	Relative Lattice Mismatch (parent str.)	M²⁺	M²⁺ Radius[b]
Cu_2ZnSnS_4	a = 5.435 Å, c = 10.843 Å (kesterite)[59]	+0% (k.)	Zn^{2+}	0.74 Å (+0%)
ZnS	a = 5.4093 Å (zinc blende)[60]	+0% (z.b.)		
	a = 3.8140 Å, c = 6.2576 Å (wurtzite)[61]	+0% (w.)		
Cu_2MnSnS_4	a = 5.514, c = 10.789 Å (kesterite)[62]	-0.5% (k.)	Mn^{2+}	0.80 Å (+8%)
	a = 3.843 Å, c = 6.331 Å (wurtzite)[39]	+1.2% (w.)		
Cu_2CoSnS_4	a = 5.402 Å, c = 10.805 Å (stannite)[63]	-0.4% (k./s.)	Co^{2+}	0.72 Å (-3%)
Cu_2NiSnS_4	a = 5.425 Å (zinc blende)[63]	+0.3% (z.b.)	Ni^{2+}	0.69 Å (-7%)

[a]Lattice parameters determined from Powder Diffraction Files (PDF); CZTS: 26-575, CMnTS: 51-575 CCoTS: 26-513, CNiTS: 26-552, ZnS (z.b.): 5-566, ZnS(w.): 36-1450. No PDF file was available for wurtzite Cu_2MnSnS_4. [b]Shannon's crystal radii (ref. 58).

General Synthesis. Our general synthesis of $Cu_2M_xZn_{1-x}SnS_4$ nanorods is shown in Scheme 1.[48] Briefly, a 1:7 mixture of 1-dodecanethiol and tert-dodecylthiol was injected to a dispersion of the metal precursor salts in an ODE-TOPO mixture at 120 °C, causing an immediate color change from blue to green; subsequent heating to 210 °C turned the solution dark brown or black, which is consistent with the measured band gap values of 1.3-1.6 eV and 775-950 nm (Figure 1 and Supporting Information available). First principles calculations have shown that the valence band in wurtzite and kesterite CZTS mainly consists of sulfur p and copper d orbitals, while the conduction band consists of sulfur s and p, and tin p orbitals.[64,65] It is reasonable to expect that doping with

a transition metal may alter the band gap somewhat by adding metal d orbitals, as is observed experimentally.[13,16,39]
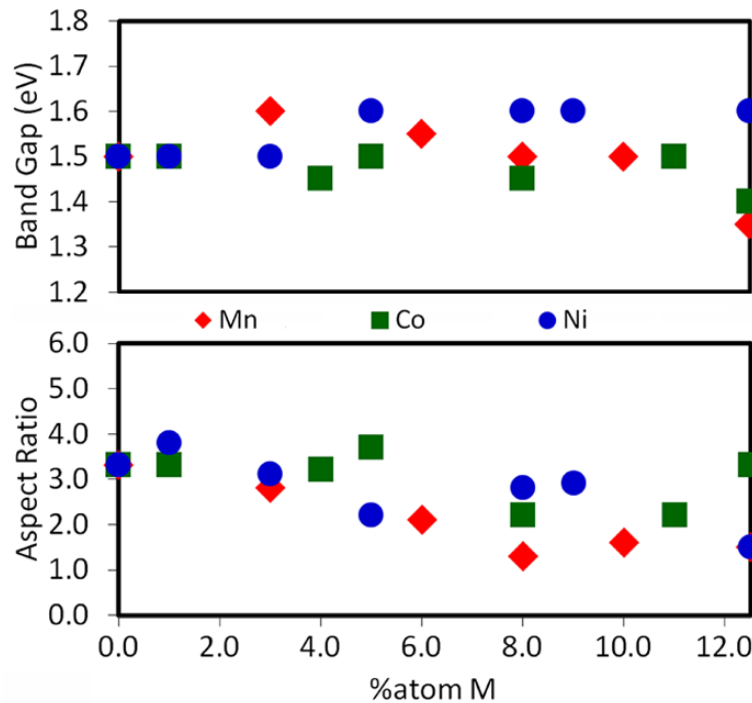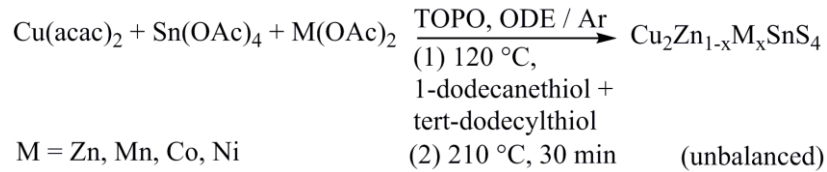
Scheme 1.

$$Cu(acac)_2 + Sn(OAc)_4 + M(OAc)_2 \xrightarrow[\substack{(1)\ 120\ °C,\\ 1\text{-dodecanethiol} +\\ \text{tert-dodecylthiol}\\ (2)\ 210\ °C,\ 30\ min}]{TOPO,\ ODE\ /\ Ar} Cu_2Zn_{1-x}M_xSnS_4$$

M = Zn, Mn, Co, Ni   (unbalanced)

Figure 1. Effect of doping level on the observed absorption onset (band gap obtained from tauc plot, see Supporting Information) (a) and aspect ratio (b) of $Cu_2M_xZn_{1-x}SnS_4$ (M = Mn, Co, Ni) nanocrystals.

Mn^{2+}-Doped CZTS Nanorods. Powder X-ray diffraction (XRD) shows that $Cu_2Mn_xZn_{1-x}SnS_4$ nanocrystals have the same wurtzite (hexagonal) structure as the undoped CZTS nanorods (Figure 2).[58] The anisotropic, elongated (1D) nature of the

nanocrystals is evident from the different peak widths of the diffractions corresponding to the 100 (broad, diameter dimension) and 002 (narrow, axial direction) lattice planes (Table 2).[66] Transmission electron microscopy (TEM) confirms the elongated, 1D morphology of the nanorods (Figure 3). From the XRD and TEM data, Mn-doping appears to have a small but consistent lowering effect on the aspect ratio of the nanocrystals (Figure 1); the changing single crystalline domain "size" across different directions is reflected in the broadening and narrowing of different peaks in the powder XRD patterns (for example, Figure 2).[66] EDX data indicate that it may be possible to substitute manganese into copper sites, in addition to the zinc sites, as judged by the highest observed manganese value of 18 atom%, compared to a theoretical limit of 12.5 atom% for the zinc sites, only.
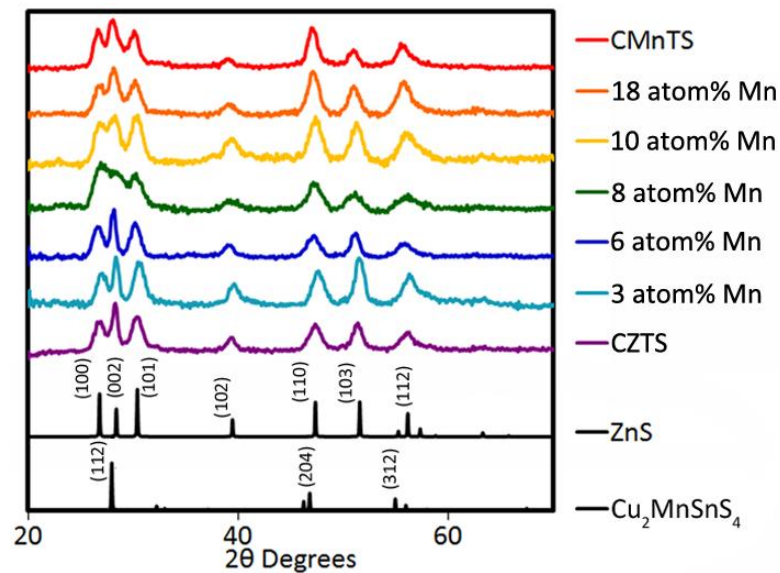

Figure 2. Powder XRD patterns of hexagonal (wurtzite) $Cu_2Mn_xZn_{1-x}SnS_4$ nanocrystals. Relevant standard patterns are included for comparison. Doping levels are atom% Mn from EDX (see Experimental), with CMnTS having a nominal value of 12.5%.

Table 2. Composition and morphology of $Cu_2M_xZn_{1-x}SnS_4$ nanocrystals (M = Mn, Co, Ni).

[Dopant] (atom%)[a]	Compositional assignment	XRD L (nm)	XRD D (nm)	AR	TEM L (nm)	TEM D (nm)	AR
$3.3 \pm 0.1\%$ Mn	$Cu_2Mn_{0.26}Zn_{0.74}SnS_4$	13.2	6.4	2.1	17 ± 5	5.8 ± 0.8	2.9 ± 0.1
$6.3 \pm 0.6\%$ Mn	$Cu_2Mn_{0.50}Zn_{0.50}SnS_4$	14.6	6.4	2.3	14 ± 2	7 ± 1	2.00 ± 0.05
$6.0 \pm 0.3\%$ Mn	$Cu_2Mn_{0.48}Zn_{0.52}SnS_4$	6.6	5.4	1.2	13 ± 2	9 ± 1	1.44 ± 0.03
$8.0 \pm 0.3\%$ Mn	$Cu_2Mn_{0.64}Zn_{0.36}SnS_4$	4.4	3.6	1.2	6 ± 1	4.4 ± 0.7	1.36 ± 0.02
$10.4 \pm 0.4\%$ Mn	$Cu_2Mn_{0.83}Zn_{0.17}SnS_4$	5.4	5.2	1.1	9 ± 2	5 ± 1	1.80 ± 0.04
$18.4 \pm 0.9\%$ Mn	$Cu_{1.53}Mn_{1.47}SnS_4$	6.7	6.3	1.1	10 ± 2	7 ± 1	1.43 ± 0.03
$1.4 \pm 0.1\%$ Co	$Cu_2Co_{0.11}Zn_{0.89}SnS_4$	12.4	6.8	1.8	19 ± 5	5.9 ± 0.9	3.2 ± 0.2
$3.8 \pm 0.2\%$ Co	$Cu_2Co_{0.30}Zn_{0.70}SnS_4$	12.8	6.8	1.9	19 ± 6	6.1 ± 0.9	3.1 ± 0.2
$4.6 \pm 0.7\%$ Co	$Cu_2Co_{0.37}Zn_{0.63}SnS_4$	14.6	8	1.8	26 ± 8	7 ± 1	3.7 ± 0.3
$7.9 \pm 0.3\%$ Co	$Cu_2Co_{0.63}Zn_{0.37}SnS_4$	10.8	7.6	1.4	16 ± 3	7 ± 1	2.29 ± 0.07
$10.8 \pm 0.3\%$ Co	$Cu_2Co_{0.86}Zn0_{0.14}SnS_4$	10.0	5.0	2.0	14 ± 2	6 ± 1	2.33 ± 0.05
$13 \pm 2\%$ Co	Cu_2CoSnS_4	5.3	5.1	1.1	21 ± 4	7 ± 1	3.0 ± 0.1
$0.7 \pm 0.3\%$ Ni	$Cu_2Ni_{0.06}Zn_{0.94}SnS_4$	9.5	4.4	2.2	15 ± 4	4.0 ± 0.7	3.8 ± 0.2
$3.1 \pm 0.8\%$ Ni	$Cu_2Ni_{0.25}Zn_{0.75}SnS_4$	10.8	7.3	1.5	17 ± 5	5.5 ± 0.7	3.1 ± 0.2
$5 \pm 1\%$ Ni	$Cu_2Ni_{0.38}Zn_{0.62}SnS_4$	7.6	6.4	1.2	11 ± 2	5.0 ± 0.8	2.20 ± 0.05
$8 \pm 2\%$ Ni	$Cu_2Ni_{0.62}Zn_{0.38}SnS_4$	15.8	3.5	4.5	13 ± 3	4.7 ± 0.8	2.77 ± 0.09
$9.0 \pm 0.9\%$ Ni	$Cu_2Ni_{0.72}Zn_{0.28}SnS_4$	16.4	3.8	4.3	14 ± 3	4.8 ± 0.7	2.92 ± 0.09
$12 \pm 1\%$ Ni	Cu_2NiSnS_4	6.2	4.7	1.3	8 ± 2	5.3 ± 0.8	1.51 ± 0.03

[a]Average of five EDX area scans.
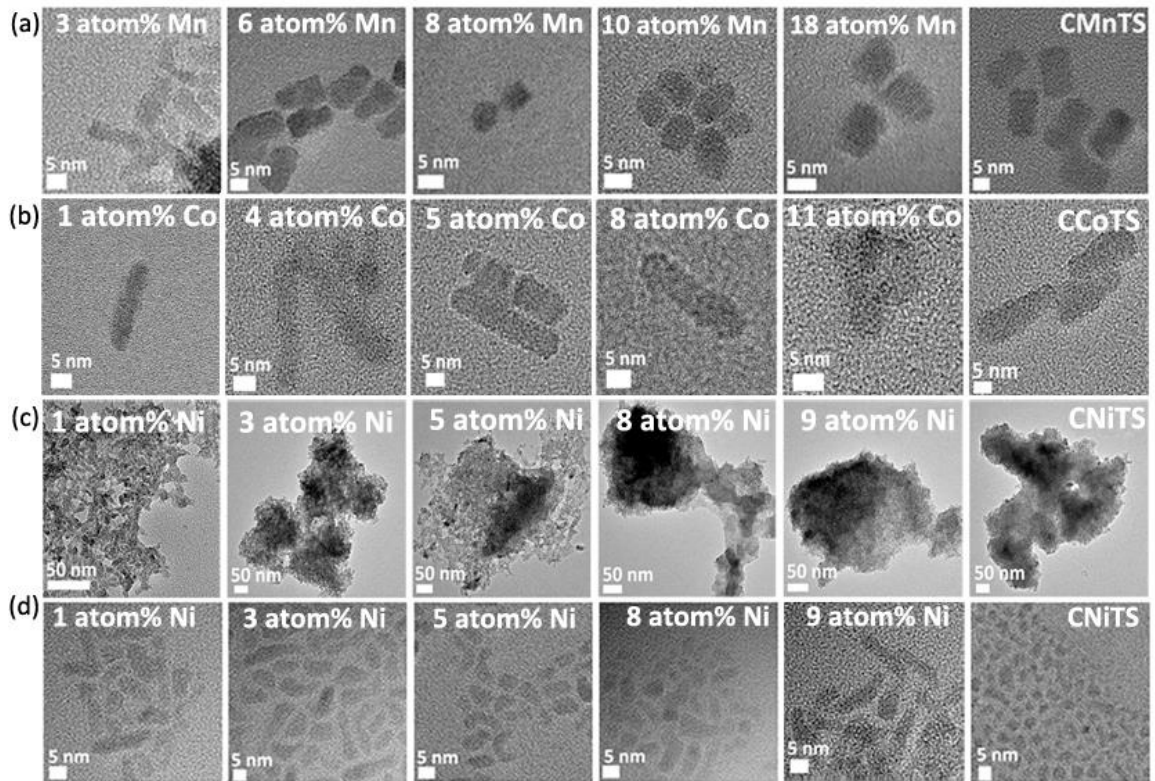
Figure 3. Representative TEM images of $Cu_2M_xZn_{1-x}SnS_4$ nanocrystals with M = Mn (a), Co (b), and Ni before (c) and after (d) thiol washing (to decrease aggregation, see experimental). Doping levels are atom% values determined from EDX (see Experimental); CMnTS, CCoTS, CNiTS have a nominal doping level of 12.5% M.

EPR Characterization and Effect of TOPO Washing. To characterize the presence of magnetic ion dopants within the nanocrystalline CZTS lattice, we employed electron paramagnetic resonance (EPR) spectroscopy. To remove excess manganese ions from the surface of the nanocrystals, we employed the TOPO (trioctylphosphine oxide) washing method (see Experimental and scheme S2).[53,54] After this TOPO wash, the EPR spectra were smoother and more consistent from sample to sample. Removal of excess Mn^{2+} is known to reduce spin-spin interactions between neighboring magnetic ions. In our case, this improvement is best seen in the EPR of the 3 atom% Mn sample, where the hyperfine splitting becomes discernable only after the surface manganese ions have been removed (Figure 4). By analogy to other well-studied nanocrystal host lattices such as CdSe, this result indicates that the remaining manganese signal is coming from Mn^{2+} ions within the doped CZTS crystal lattice.

EPR measurements at 10 K show that the $Cu_2Mn_{0.26}Zn_{0.74}SnS_4$ nanorods, with the lowest manganese concentration we studied (3 atom% Mn), exhibit the typical six peak spectrum consistent with tetrahedral, high spin Mn^{2+}, a $3d^5$ ion with $S = 5/2$.[67-74] EasySpin simulation of this sample's EPR spectrum yields a hyperfine splitting of $A = 68 \times 10^{-4}$ cm^{-1}, $g = 2.0055$, and a zero field splitting parameter of $D = 31 \times 10^{-4}$ cm^{-1} (see Supporting Information). These values are similar to those found in previous reports of internal Mn^{2+} in tetrahedral sites.[23,69,73,75,78-80] No hyperfine splitting was observed at room temperature, likely because EPR sensitivity of most transition metals increases by lowering the temperature.[67]

XPS measurements were utilized to determine the oxidation states of the materials, shown in Figure 8. The Cu $2p_{1/2}$ and $2p_{3/2}$ peaks at 952.0 eV and 932.2 eV are

indicative of Cu(I) with a splitting of 19.9 eV (see below and Supporting Information).[81] The Mn $2p_{1/2}$ and $2p_{3/2}$ peaks at 653.9 eV and 642.3 eV have a splitting of 11.6 eV, indicative of Mn(II).[41] Sn $3d_{3/2}$ and $3d_{5/2}$ peaks for tin(IV), at 494.9 eV and 486.5 eV show a splitting of 8.4 eV.[82] The S 2p peak at 162.5 eV is consistent with literature reports of the sulfur 2p peak in sulfide phases.[83]
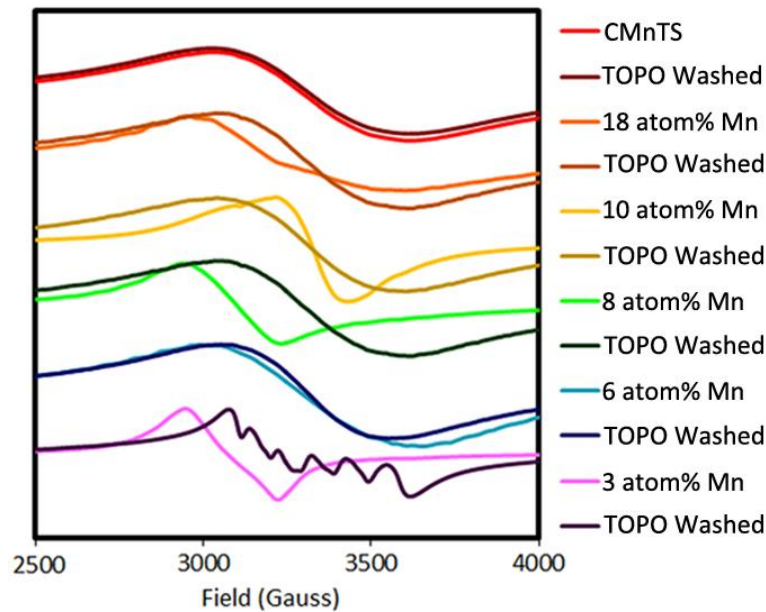

Figure 4. EPR spectra of $Cu_2Mn_xZn_{1-x}SnS_4$ nanocrystals in toluene at 10 K. Doping levels are atom% Mn from EDX (see Experimental), with CMnTS having a nominal value of 12.5%.

Co^{2+}-Doped CZTS Nanorods. Powder XRD shows that the $Cu_2Co_xZn_{1-x}SnS_4$ nanocrystals also adopt the wurtzite crystal structure (Figure 5). Only the sample containing 11 atom% Co appears to contain a small amount of the ternary cubic impurity $CuCo_2S_4$ (reference pattern is shown in Figure 5). Both XRD (from the broad 100 *vs.* narrow 002 diffractions) and TEM show that these nanocrystals are elongated (Table 2

and Figure 3b). Unlike the Mn case above, Co doping does not systematically affect the aspect ratio of the nanorods (Figure 1).
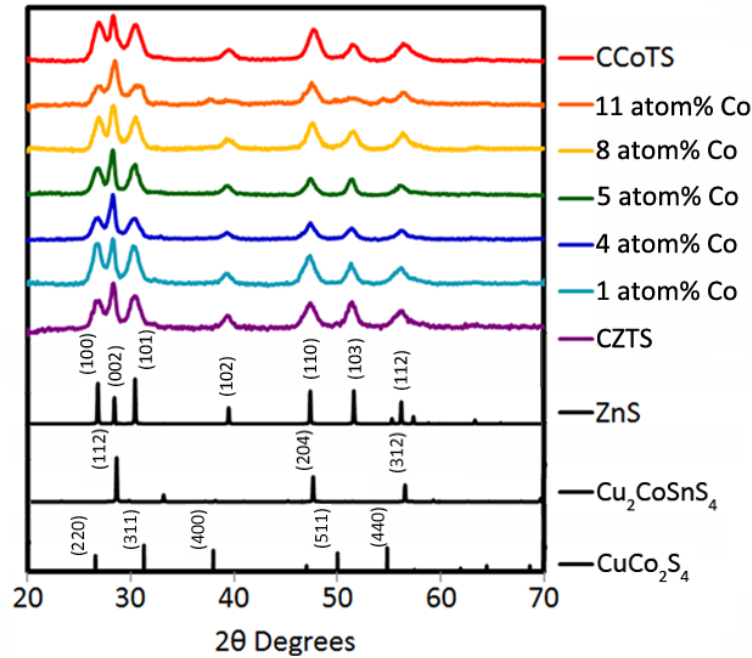

Figure 5. Powder XRD patterns of hexagonal (wurtzite) $Cu_2Co_xZn_{1-x}SnS_4$ nanocrystals. Relevant standard patterns, along with that of a possible impurity, $CuCo_2S_4$ (PDF #42-1450), are included for comparison. Doping levels are atom% Co from EDX (see Experimental), with CCoTS having a nominal value of 12.5%.

To characterize the presence of magnetic cobalt dopant ions within the $Cu_2Co_xZn_{1-x}SnS_4$ nanocrystals, we employed X-band EPR measurements at 10 K (Figure 6). The analysis was performed at low temperature because, due to fast spin-lattice relaxation, high spin Co(II) is only active at temperatures less than 20 K.[84] The EPR spectra show a feature at ~1240 Gauss which is associated with a high spin Co^{2+} signal.[85-89] This signal corresponds to a spin of S = 3/2, due to 3 unpaired electrons ($3d^7$). The cobalt signal is broad due to dipole-dipole coupling, so no hyperfine structure is observed (broad signals are typical for high spin cobalt systems).[90] However, by simulating this

Co^{2+} portion of the CCoTS spectra we calculate a g value of 4.3. This high g value agrees well with related literature reports (see Supporting Information).[92-95] Based on the g value of 4.3, we can estimate the value of E/D to be ~0.02 (unitless).[89,96-98]

The signal at ~3400 G is due to Cu^{2+} defects, with $g_z = g_\parallel = 2.26$ and g_x, $g_y = g_\perp = 2.025$, A_x, $A_y = A_\perp = 16 \times 10^{-4}$ cm^{-1} and $A_z = A_\parallel = 133 \times 10^{-4}$ cm^{-1} (see Supporting Information). These values are similar to those in previous reports for Cu^{2+} spectra.[99-101] We believe that the resolution differences are due to changes in concentration of the Cu^{2+} impurity in each sample. This Cu^{2+} signal has been seen before in kesterite CZTS nanocrystals, and indicates that there may be a mixture of Cu$^+$ and Cu^{2+} defects in our samples.[57,100,102]
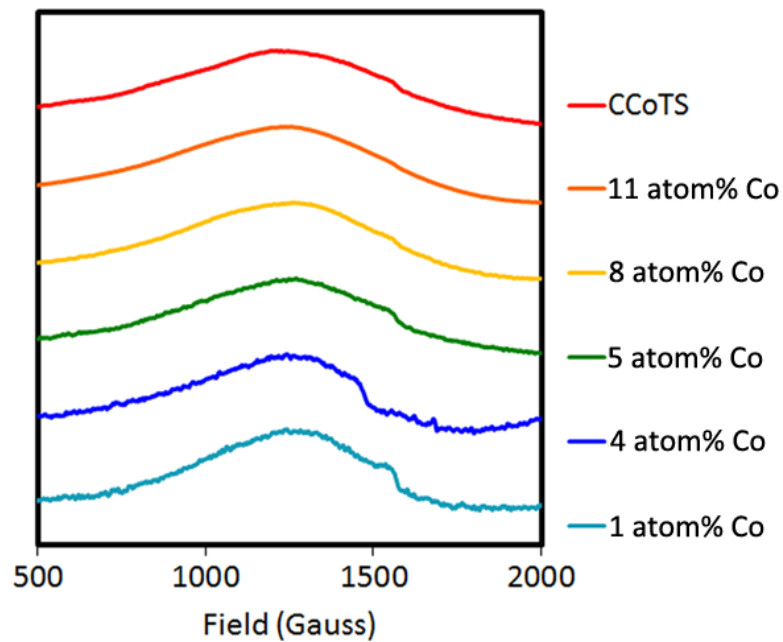

Figure 6. EPR spectra of Cu$_2$Co$_x$Zn$_{1-x}$SnS$_4$ nanocrystals in toluene at 10 K. Doping levels are atom% Co from EDX (see Experimental), with CCoTS having a nominal value of 12.5%.

To confirm the oxidation states of the metals and sulfur in the cobalt doped CZTS nanocrystals, we employed X-ray photoelectron spectroscopy (XPS), as shown in Figure 7. Cu $2p_{1/2}$ and $2p_{3/2}$ peaks at 951.9 eV and 932.1 eV are indicative of Cu(I) with a splitting of 19.8 eV.[81] Co $2p_{1/2}$ and $2p_{3/2}$ peaks at 794.0 eV and 778.6 eV are indicative of Co(II) with a splitting of 15.3 eV.[103] Sn $3d_{3/2}$ and $3d_{5/2}$ peaks for Sn(IV), at 494.6 eV and 486.3 eV show a splitting of 8.4 eV.[82] The peak at 162.4 eV is consistent with literature reports of the sulfur 2p peak in sulfide phases.[83]
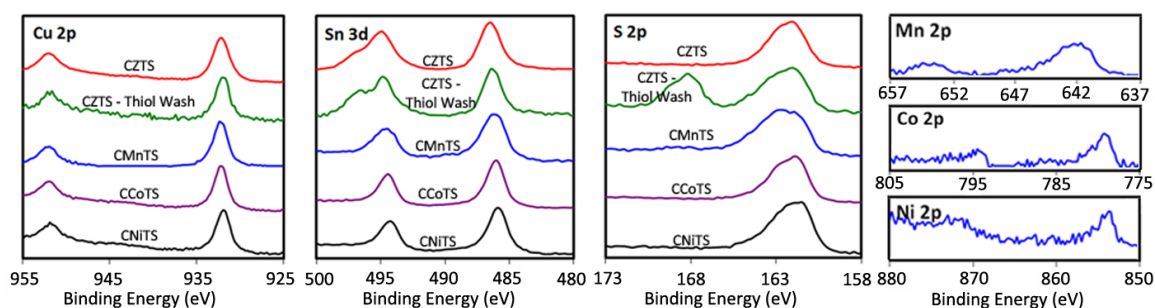
Figure 7. Comparative (stacked) XPS spectra of CZTS, CMnTS, CCoTS, and CNiTS, and thiol-washed CZTS nanocrystals.

Ni^{2+}-Doped CZTS Nanorods. Powder XRD and TEM shows that the $Cu_2Ni_xZn_{1-x}SnS_4$ nanocrystals are hexagonal (wurtzite) nanorods (Figures 3c and 8). Compared to Mn, Ni doping has a smaller but still measurable effect in lowering the degree of anisotropy (elongation) of the nanocrystals (Figure 1). Specifically, their aspect ratio goes from roughly 4 to 2 upon doping with 0 atom% nickel and 12.5 atom% nickel, respectively (Table 2). Based on literature reports, the zero-field splitting of transition metals with S = 1 exceeds the microwave quantum, and their EPR signal appears at fields and frequencies beyond the capabilities of traditional EPR instruments.[104] An example of such EPR silent system is Ni^{2+}, a $3d^8$ non-Kramer's system with an integer-spin ground

state S = 1.[105] For this reason, EPR measurements were not performed on the Ni doped nanocrystals.
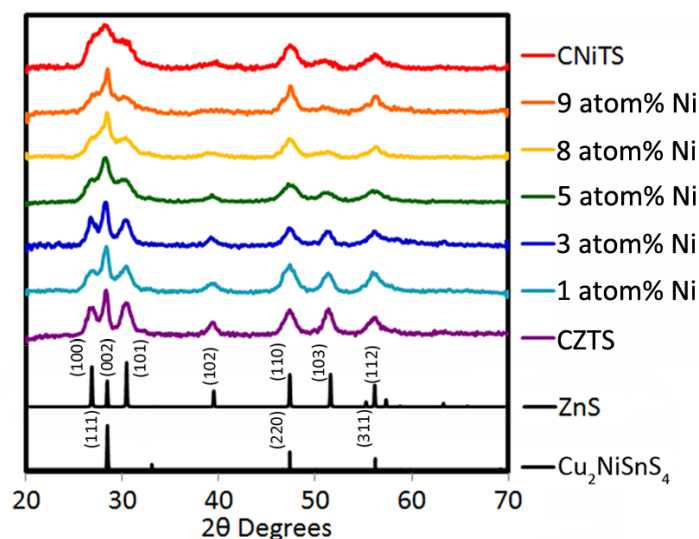

Figure 8. Powder XRD patterns of hexagonal (wurtzite) $Cu_2Ni_xZn_{1-x}SnS_4$ nanocrystals. Relevant standard patterns are included for comparison. Doping levels are atom% Ni from EDX (see Experimental), with CNiTS having a nominal value of 12.5%.

To elucidate the different element's oxidation states in the Cu_2NiSnS_4 nanocrystals, we performed XPS measurements (Figure 7). Cu $2p_{1/2}$ and $2p_{3/2}$ peaks at 951.7 eV and 931.8 eV are indicative of Cu(I) with a splitting of 19.8 eV.[81] Ni $2p_{1/2}$ and $2p_{3/2}$ peaks at 871.1 eV and 853.4 eV are indicative of Ni(II) with a splitting of 17.8 eV.[106] Sn $3d_{3/2}$ and $3d_{5/2}$ peaks for Sn(IV), at 494.4 eV and 486.0 eV show a splitting of 8.4 eV.[82] The S 2p peak at 162.4 eV is consistent with literature reports of the sulfur 2p peak in sulfide phases.[80]

Aggregation of CZTS and Ni^{2+}-Doped CZTS Nanorods: Effect of Thiol Washing. Significant nanocrystal aggregation was observed in the TEM images of the as prepared nickel-doped materials, as well as in the parent undoped CZTS nanorods. Previous

studies have followed the formation of aggregates in binary metal chalcogenide nanocrystals. On the basis of Raman and XPS spectroscopy, these previous studies proposed that clustering in such binary systems was due to dichalcogenide bond formation between neighboring particles.[107,108] Washing with a reducing agent was shown to break the dichalcogenide bonds, breaking up the aggregates, and producing well-defined, soluble particles.

In view of these results, we attempted a similar method to wash our aggregated quaternary particles using excess thiols. Briefly, a mixture of 1-dodecanethiol and tert-dodecylthiol was used to wash the particles dispersed in toluene, before proceeding to purification (see Experimental). TEM shows that this method succeeds in reducing aggregation of both CZTS and $Cu_2Ni_xZn_{1-x}SnS_4$ nanorods (Figures 3c,d and 9). To gain further insight into the surface chemistry changes that may be responsible for this behavior in our system, we utilized XPS. After thiol washing the CZTS nanocrystals, a second sulfur peak at 168.3 eV, indicative of oxidized sulfur in sulfonates, RSO_3^-, appeared in the XPS spectrum (Figure 8).[109] A shoulder peak at 497 eV has been reported as characteristic of the Sn 3d peak.[110] Critically, FTIR spectra confirmed the presence of a sulfonate species after the thiol wash, as evidenced by a sulfonate symmetric stretching peak at 1189 cm^{-1} (see Supporting Information).[111,112] An additional IR peak at 1145 cm^{-1}, both before and after thiol washing the CZTS nanorods, corresponds to TOPO ligands on the surface of the nanorods.[113] Several attempts using Raman and XPS failed to show any sulfur peaks associated with disulfide bond forming/breaking on the surface of these quaternary nanocrystals.

Based on these results, we believe that the surface chemistry of quaternary chalcogenides such as CZTS and CNiTS nanorods differs substantially from that of other chalcogenide systems. On the basis of the aforementioned XPS and FTIR data, we speculate that excess metal ions, present during synthesis, may be responsible for the observed aggregation by crosslinking terminal sulfides on the surface of the nanocrystals (scheme S1).[114] This aggregation is much more prevalent in the Cu_2ZnSnS_4 and $Cu_2Ni_xZn_{1-x}SnS_4$ nanocrystals. We believe this could be because Zn^{2+} and Ni^{2+} are softer acids than Co^{2+} and Mn^{2+}.[115-117] Hard-soft acid-base theory predicts that Zn^{2+} and Ni^{2+} will be more attracted to sulfur, since S^{2-} is a soft base, leading to increased aggregation in these materials compared to the $Cu_2Mn_xZn_{1-x}SnS_4$ or $Cu_2Co_xZn_{1-x}SnS_4$ nanocrystals. Upon washing, the added thiols bind the excess metal ions, thus removing them from the particle surface and reducing aggregation. In this way, the terminal sulfur or sulfides on the particle surface become exposed and more susceptible to oxidation when stored in air, forming the sulfonate species we observed via XPS and FTIR.

Conclusions

We have successfully doped hexagonal (wurtzite) Cu_2ZnSnS_4 nanorods with Mn^{2+}, Co^{2+}, and Ni^{2+}. Experimental evidence is consistent with substitution at the zinc site in the three series from CZTS to CMTS. All three series show a wurtzite crystal structure by powder XRD, and broad absorption over the visible range, with a band gap ranging from 1.3-1.6 eV. TEM measurements show that each material retains the original nanorod morphology, with aspect ratios generally varying from 3.8-1.3 as the metal loading increases. EPR analysis confirms the presence of Mn^{2+} and Co^{2+} metal ions in a high spin configuration and XPS analysis shows that the oxidation states of the metal

dopants are Mn^{2+}, Co^{2+}, and Ni^{2+}. XPS was also used to determine the oxidation states of additional components as Cu^+, Sn^{4+}, Zn^{2+}, and S^{2-}.
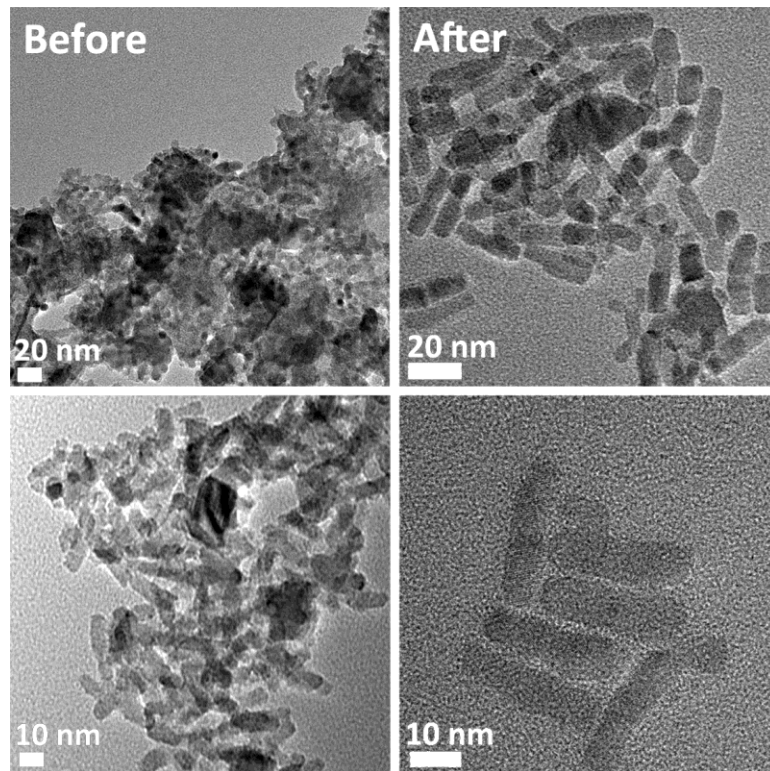

Figure 9. TEM images of CZTS rods before (left) and after (right) thiol washing, showing a corresponding decrease in particle aggregation (see Experimental).

Along with the original methanol/ethanol wash, a TOPO wash was employed to purify the $Cu_2Mn_xZn_{1-x}SnS_4$ samples. The TOPO ligands bind strongly to the excess Mn^{2+} ions on the surface of the nanocrystals. Upon centrifugation, the TOPO ligands are removed, pulling the excess Mn^{2+} from the surface as well. The EPR signal in the 3 atom% Mn sample confirms that this is the case, because the spectrum shows a drastic change before and after this wash, from one smooth curve to the expected six peak splitting EPR pattern. Analogous to other systems, this change in the EPR spectrum indicates that the manganese remaining in the sample is located within (at the interior of) the nanocrystal lattice.

Several samples in this study showed substantial aggregation, particularly Cu_2ZnSnS_4 and $Cu_2Ni_xZn_{1-x}SnS_4$ nanocrystals. We mitigated this problem by employing an additional thiol wash. Aggregation was significantly reduced throughout the entire sample by washing the nanocrystals with a mixture of 1-dodecanethiol and tert-dodecylthiol, followed by centrifugation. We believe aggregation is due to metal ions crosslinking the surface terminal sulfides of separate nanocrystals. Upon washing, the additional free thiols bind and remove the metal ions, leaving the terminal sulfurs free to oxidize in air. This hypothesis is supported by the XPS data and FTIR data after the thiol wash, which show new peaks corresponding to sulfonate species.

In summary, we have synthesized and characterized wurtzite $Cu_2M_xZn_{1-x}SnS_4$ nanorods (M = Mn^{2+}, Co^{2+}, Ni^{2+}) with different dopant concentrations from $0 \leq x \leq 1$ (from CZTS to CMTS). In addition, we have shown that different methods of washing the nanocrystals can be employed to improve the purity and spectral quality of these materials. The magnetic properties of these materials warrant further investigation, and may enable future applications in new areas such as data storage and spintronics.

Acknowledgement

References

[1] Vela, J. Molecular Chemistry to the Fore: New Insights into the Fascinating World of Photoactive Colloidal Semiconductor Nanocrystals. *J. Phys. Chem. Lett.* **2013**, *4*, 653–668.

[2] Yang, J.; Son, J. S.; Yu, J. H.; Joo, J.; Hyeon, T. Advances in the Colloidal Synthesis of Two-Dimensional Semiconductor Nanoribbons. *Chem. Mater.* **2013**, *25*, 1190–1198.

[3] Singh, S.; Liu, P.; Singh, A.; Coughlan, C.; Wang, J.; Lusi, M.; Ryan, K. M. Colloidal $Cu_2ZnSn(SSe)_4$ (CZTSSe) Nanocrystals: Shape and Crystal Phase Control to Form Dots, Arrows, Ellipsoids, and Rods. *Chem. Mater.* **2015**, *27*, 4742–4748.

[4] Hossain, M. I. Prospects of CZTS Solar Cells from the Perspective of Material Properties, Fabrication Methods and Current Research Challenges. *Chalcogenide Lett.* **2012**, *9*, 231–242.

[5] Guo, Q.; Ford, G. M.; Yang, W.-C.; Walker, B. C.; Stach, E. A.; Hillhouse, H. W.; Agrawal, R. Fabrication of 7.2% Efficient CZTSSe Solar Cells Using CZTS Nanocrystals. *J. Am. Chem. Soc.* **2010**, *132*, 17384–17386.

[6] Steinhagen, C.; Panthani, M. G.; Akhavan, V.; Goodfellow, B.; Koo, B.; Korgel, B. A. Synthesis of Cu_2ZnSnS_4 Nanocrystals for Use in Low–Cost Photovoltaics. *J. Am. Chem. Soc.* **2009**, *131*, 12554–12555.

[7] Riha, S. C.; Parkinson, B. A.; Prieto, A. L. Solution–Based Synthesis and Characterization of Cu_2ZnSnS_4 Nanocrystals. *J. Am. Chem. Soc.* **2009**, *131*, 12054–12055.

[8] Mitzi, D. B.; Gunawan, O.; Todorov, T. K.; Wang, K.; Guha, S. The Path Towards a High-performance Solution–processed Kesterite Solar Cell. *Sol. Energy Mater. Sol. Cells* **2011**, *95*, 1421–1436.

[9] Suryawanshi, M. P.; Agawane, G. L.; Bhosale, S. M.; Shin, S. W.; Patil, P. S.; Kim, J. H.; Moholkar, A. V. CZTS Based Thin Film Solar Cells: a Status Review. *Mater. Technol.* **2013**, *28*, 98–109.

[10] Wang, H. Progress in Thin Film Solar Cells Based on Cu_2ZnSnS_4. *Int. J. Photoenergy* **2011**, 1–10.

[11] Wadia, C.; Alivisatos, A. P.; Kammen, D. M. Materials Availability Expands the Opportunity for Large-Scale Photovoltaics Deployment. *Environ. Sci. & Tech.* **2009**, *43*, 2072–2077.

[12] Sarkar, S.; Bose, R.; Jana, S.; Jana, N. R.; Pradhan, N. Doped Semiconductor Nanocrystals and Organic Dyes: An Efficient and Greener FRET System. *J. Phys. Chem. Lett.* **2010**, *1*, 636–640.

[13] Gillorin, A.; Balocchi, A.; Marie, X.; Dufour, P.; Chane–Ching, J. Y. Synthesis and Optical Properties of Cu_2CoSnS_4 Colloidal Quantum Dots. *J. Mater. Chem.* **2011**, *21*, 5615–5619.

[14] Murali, B.; Krupanidhi, S. B. Facile Synthesis of Cu_2CoSnS_4 Nanoparticles Exhibiting Red–edge–effect: Application in Hybrid Photonic Devices. *J. Appl. Phys.* **2013**, *114*, 144312.

[15] Zhang, X.; Bao, N.; Lin, B.; Gupta, A., Colloidal Synthesis of Wurtzite Cu_2CoSnS_4 Nanocrystals and the Photoresponse of Spray–deposited Thin Films. *Nanotech.* **2013**, *24*, 105706.

[16] Cui, Y.; Deng, R. P.; Wang, G.; Pan, D. C. A General Strategy for Synthesis of Quaternary Semiconductor Cu_2MSnS_4 (M = Co^{2+}, Fe^{2+}, Ni^{2+}, Mn^{2+}) Nanocrystals. *J. Mater. Chem.* **2012**, *22*, 23136–23140.

[17] Wang, T.–X.; Li, Y.–G.; Liu, H.–R.; Li, H.; Chen, S.–X. Flower–like Cu_2NiSnS_4 Nanoparticles Synthesized by a Facile Solvothermal Method. *Mater. Lett.* **2014**, *124*, 148–150.

[18] Bhargava, R. N. The Role of Impurity in Doped Nanocrystals. *J. Lumin.* **1997**, *72*, 46–48.

[19] Erwin, S. C.; Zu, L. J.; Haftel, M. I.; Efros, A. L.; Kennedy, T. A.; Norris, D. J. Doping Semiconductor Nanocrystals. *Nature* **2005**, *436*, 91–94.

[20] Koole, R.; Mulder, W. J. M.; van Schooneveld, M. M.; Strijkers, G. J.; Meijerink, A.; Nicolay, K. Magnetic Quantum Dots for Multimodal Imaging. *Wiley Interdiscip. Rev. Nanomed. Nanobiotechnol.* **2009**, *1*, 475–491.

[21] Chen, H.–Y.; Son, D. H. Energy and Charge Transfer Dynamics in Doped Semiconductor Nanocrystals. *Isr. J. Chem.* **2012**, *52*, 1016–1026.

[22] Buonsanti, R.; Milliron, D. J. Chemistry of Doped Colloidal Nanocrystals. *Chem. Mater.* **2013**, *25*, 1305–1317.

[23] Beaulac, R.; Archer, P. I.; Ochsenbein, S. T.; Gamelin, D. R. Mn^{2+}–Doped CdSe Quantum Dots: New Inorganic Materials for Spin–Electronics and Spin–Photonics. *Adv. Funct. Mater.* **2008**, *18*, 3873–3891.

[24] Norris, D. J.; Yao, N.; Charnock, F. T.; Kennedy, T. A. High–quality Manganese–doped ZnSe Nanocrystals. *Nano Lett.* **2001**, *1*, 3–7.

[25] Bhargava, R. N.; Gallagher, D.; Hong, X.; Nurmikko, A. Optical Properties of Manganese–Doped Nanocrystals of ZnS. *Phys. Rev. Lett.* **1994**, *72*, 416–419.

[26] Yang, H. S.; Santra, S.; Holloway, P. H. Syntheses and Applications of Mn–doped II–VI Semiconductor Nanocrystals. *J. Nanosci. Nanotechnol.* **2005**, *5*, 1364–1375.

[27] Norberg, N. S.; Parks, G. L.; Salley, G. M.; Gamelin, D. R. Giant Excitonic Zeeman Splittings in Colloidal Co^{2+}–doped ZnSe Quantum Dots. *J. Am. Chem. Soc.* **2006**, *128*, 13195–13203.

[28] Saravanan, L.; Pandurangan, A.; Jayavel, R. Synthesis of Cobalt–doped Cadmium Sulphide Nanocrystals and their Optical and Magnetic Properties. *J. Nanopart. Res.* **2011**, *13*, 1621–1628.

[29] Norton, D. P.; Overberg, M. E.; Pearton, S. J.; Pruessner, K.; Budai, J. D.; Boatner, L. A.; Chisholm, M. F.; Lee, J. S.; Khim, Z. G.; Park, Y. D.; Wilson, R. G. Ferromagnetism in Cobalt–implanted ZnO. *Appl. Phys. Lett.* **2003**, *83*, 5488–5490.

[30] Wang, X.; Xu, J.; Zhang, B.; Yu, H.; Wang, J.; Zhang, X.; Yu, J.; Li, Q. Signature of Intrinsic High–temperature Ferromagnetism in Cobalt–doped Zinc Oxide Nanocrystals. *Adv. Mater.* **2006**, *18*, 2476–2480.

[31] Schwartz, D. A.; Norberg, N. S.; Nguyen, Q. P.; Parker, J. M.; Gamelin, D. R. Magnetic Quantum Dots: Synthesis, Spectroscopy, and Magnetism of Co^{2+}– and Ni^{2+}–doped ZnO Nanocrystals. *J. Am. Chem. Soc.* **2003**, *125*, 13205–13218.

[32] Archer, P. I.; Radovanovic, P. V.; Heald, S. M.; Gamelin, D. R. Low–temperature Activation and Deactivation of High–Curie–temperature Ferromagnetism in a New Diluted Magnetic Semiconductor: Ni^{2+}–doped SnO_2. *J. Am. Chem. Soc.* **2005**, *127*, 14479–14487.

[33] Elango, M.; Nataraj, D.; Nazeer, K. P.; Thamilselvan, M. Synthesis and Characterization of Nickel Doped Cadmium Sulfide ($CdS:Ni^{2+}$) Nanoparticles. *Mater. Res. Bull.* **2012**, *47*, 1533–1538.

[34] Kumar, S.; Verma, N. K. Effect of Ni–doping on Optical and Magnetic Properties of Solvothermally Synthesized ZnS Wurtzite Nanorods. *J. Mater. Sci. Mater. Electron.* **2014**, *25*, 785–790.

[35] Singhal, A.; Achary, S. N.; Manjanna, J.; Chatterjee, S.; Ayyub, P.; Tyagi, A. K., Chemical Synthesis and Structural and Magnetic Properties of Dispersible Cobalt– and Nickel–Doped ZnO Nanocrystals. *J. Phys. Chem. C* **2010**, *114*, 3422–3430.

[36] Bryan, J. D.; Gamelin, D. R. Doped Semiconductor Nanocrystals: Synthesis, Characterization, Physical Properties, and Applications. *Prog. Inorg. Chem.* **2005**, *54*, 47–126.

[37] Norris, D. J.; Efros, A. L.; Erwin, S. C. Doped Nanocrystals. *Science* **2008**, 319, 1776–1779.

[38] Chane–Ching, J. Y.; Gillorin, A.; Zaberca, O.; Balocchi, A.; Marie, X. Highly–crystallized Quaternary Chalcopyrite Nanocrystals via a High–temperature Dissolution–reprecipitation Route. *Chem. Commun.* **2011**, *47*, 5229–5231.

[39] Liang, X.; Guo, P.; Wang, G.; Deng, R.; Pan, D.; Wei, X. Dilute Magnetic Semiconductor Cu_2MnSnS_4 Nanocrystals with a Novel Zinc blende and Wurtzite Structure. *RSC Adv.* **2012**, *2*, 5044–5046.

[40] Fukushima, T.; Yamauchi, K.; Picozzi, S. Magnetically Induced Ferroelectricity in Cu_2MnSnS_4 and $Cu_2MnSnSe_4$. *Phys. Rev. B* **2010**, *82*, 014102.

[41] Xiao, C.; Li, K.; Zhang, J.; Tong, W.; Liu, Y.; Li, Z.; Huang, P.; Pan, B.; Su, H.; Xie, Y. Magnetic Ions in Wide Band Gap Semiconductor Nanocrystals for Optimized Thermoelectric Properties. *Mater. Horiz.* **2014**, *1*, 81–86.

[42] Alvarado, S. R.; Guo, Y.; Ruberu, T. P. A.; Tavasoli, E.; Vela, J. Solutions to Semiconductor Nanocrystal Problems. *Coord. Chem. Rev.* **2014**, *263*, 182–196.

[43] Guo, Y.; Alvarado, S. R.; Barclay, J. D.; Vela, J. Shape–Programmed Nanofabrication: Understanding the Reactivity of Dichalcogenide Precursors. *ACS Nano* **2013**, *7*, 3616–3626.

[44] Ruberu, T. P. A.; Vela, J. Expanding the One–Dimensional CdS–CdSe Composition Landscape: Axially Anisotropic $CdS_{1-x}Se_x$ Nanorods. *ACS Nano* **2011**, *5*, 5775–5784.

[45] Ruberu, T. P. A.; Albright, H. R.; Callis, B.; Ward, B.; Cisneros, J.; Fan, H.-J.; Vela, J. Molecular Control of the Nanoscale: Effect of Phosphine-Chalcogenide Reactivity on CdS-CdSe Nanocrystal Composition and Morphology. *ACS Nano* **2012**, *6*, 5348–5359.

[46] Alvarado, S. R.; Shortt, I. A.; Fan, H.-J.; Vela, J. Assessing Phosphine-Chalcogen Bond Energetics from Calculations. *Organometallics* **2015**, *34*, 4023–4031.

[47] Hendricks, M. P.; Campos, M. P.; Cleveland, G. T.; Jen-La Plante, I.; Owen, J. S. A Tunable Library of Substituted Thiourea Precursors to Metal Sulfide Nanocrystals. *Science* **2015**, *348*, 1226–1230.

[48] Thompson, M. J.; Ruberu, T. P. A.; Blakeney, K. J.; Torres, K. V.; Dilsaver, P. S.; Vela, J. Axial Composition Gradients and Phase Segregation Regulate the Aspect Ratio of Cu_2ZnSnS_4 Nanorods. *J. Phys. Chem. Lett.* **2013**, 4, 3918–3923.

[49] Collord, A. D.; Hillhouse, H. W. Composition Control and Formation Pathway of CZTS and CZTGS Nanocrystal Inks for Kesterite Solar Cells. *Chem. Mater.* **2015**, *27*, 1855–1862.

[50] Zou, Y.; Su, X.; Jiang, J. Phase-Controlled Synthesis of Cu_2ZnSnS_4 Nanocrystals: The Role of Reactivity between Zn and S. *J. Amer. Chem. Soc.* **2013**, *135*, 18377–18384.

[51] Dilsaver, P. S.; Reichert, M. D.; Hallmark, B. L.; Thompson, M. J.; Vela, J., Cu_2ZnSnS_4–Au Heterostructures: Toward Greener Chalcogenide–Based Photocatalysts. *J. Phys. Chem. C* **2014**, *118*, 21226–21234.

[52] Singh, A.; Geaney, H.; Laffir, F.; Ryan, K. M., Colloidal Synthesis of Wurtzite Cu_2ZnSnS_4 Nanorods and Their Perpendicular Assembly. *J. Am. Chem. Soc.* **2012**, *134,* 2910–2913.

[53] Mikulec, F. V.; Kuno, M.; Bennati, M.; Hall, D. A.; Griffin, R. G.; Bawendi, M. G. Organometallic Synthesis and Spectroscopic Characterization of Manganese-doped CdSe Nanocrystals. *J. Am. Chem. Soc.* **2000**, *122*, 2532–2540.

[54] Bryan, J. D.; Heald, S. M.; Chambers, S. A.; Gamelin, D. R. Strong Room–temperature Ferromagnetism in Co^{2+}–doped TiO_2 Made from Colloidal Nanocrystals. *J. Am. Chem. Soc.* **2004**, *126*, 11640–11647.

[55] Stoll, S.; Schweiger, A. EasySpin, a Comprehensive Software Package for Spectral Simulation and Analysis in EPR. *J. Magn. Reson.* **2006**, *178*, 42−55.

[56] Tauc, J. Optical Properties and Electronic Structure of Amorphous Ge and Si. *Mater. Res. Bull.* **1968**, *3*, 37−46.

[57] Bernardini, G. P.; Borrini, D.; Caneschi, A.; Di Benedetto, F.; Gatteschi, D.; Ristori, S.; Romanelli, M. EPR and SQUID Magnetometry Study of Cu_2FeSnS_4 (Stannite) and Cu_2ZnSnS_4 (Kesterite). *Phys. Chem. Miner.* **2000**, *27*, 453–461.

[58] Shannon, R. D. Revised Effective Ionic Radii and Systematic Studies of Interatomic Distances in Halides and Chalcogenides. *Acta Crystallogr. A* **1976**, *32*, 751–767.

[59] Guen, L.; Glaunsinger, W. S.; Wold, A. Physical Properties of the Quaternary Chalcogenides $Cu_2^IB^{II}C^{IV}X_4$ (B^{II} = Zn, Mn, Fe, Co; C^{IV} = Si, Ge, Sn; X = S, Se) *Mat. Res. Bull.* **1979**, *14*, 463–467.

[60] Vanaswegen, J. T. S.; Verleger, H. Rontgenographische Untersuchung Des Systems ZnS-FeS. *Naturwissenschaften* **1960**, *47*, 131–131.

[61] Xu, Y. N.; Ching, W. Y. Electronic, Optical, and Structural Properties of some Wurtzite Crystals. *Phys. Rev. B* **1993**, *48*, 4335–4351.

[62] Fries, T.; Shapira, Y.; Palacio, F.; Morón, M. C.; McIntyre, G. J.; Kershaw, R.; Wold, A.; McNiff, E. J. Magnetic Ordering of the Antiferromagnet Cu_2MnSnS_4 from Magnetization and Neutron-scattering Measurements. *Phys. Rev. B* **1997**, *56*, 5424–5431.

[63] Schafer, W.; Nitsche, R. Tetrahedral Quaternary Chalcogenides of Type Cu_2-II-IV-$S_4(Se_4)$. *Mat. Res. Bull.* **1974**, *9*, 645–654.

[64] Zhao, Z.; Ma, C.; Cao, Y.; Yi, J.; He, X.; Qiu, J. Electronic Structure and Optical Properties of Wurtzite-kesterite Cu_2ZnSnS_4. *Phys. Lett. A* **2013**, *377*, 417–422.

[65] Ghosh, A.; Thangavel, R.; Rajagopalan, M. First-Principles Study of Structural Stability and Optical Properties of Cu_2XSnY_4 (X = Fe, Co, Ni; Y = S, Se) for Photovoltaic Applications. *Energy Environ. Focus* **2014**, *3*, 142–151.

[66] Reichert, M. D.; Lin, C.-C.; Vela, J. How Robust are Semiconductor Nanorods? Investigating the Stability and Chemical Decomposition Pathways of Photoactive Nanocrystals. *Chem. Mater.* **2014**, *26*, 3900–3908.

[67] Magana, D.; Perera, S. C.; Harter, A. G.; Dalal, N. S.; Strouse, G. F. Switching–on Superparamagnetism in Mn/CdSe Quantum Dots. *J. Am. Chem. Soc.* **2006**, *128*, 2931–2939.

[68] Eaton, G. R.; Eaton, S. S.; Barr, D. P.; Weber, R. T. Quantitative EPR; Springer: New York, 2010

[69] Zheng, W.; Wang, Z.; Wright, J.; Goundie, B.; Dalal, N. S.; Meulenberg, R. W.; Strouse, G. F. Probing the Local Site Environments in Mn:CdSe Quantum Dots. *J. Phys. Chem. C* **2011**, *115*, 23305–23314.

[70] Murase, N.; Jagannathan, R.; Kanematsu, Y.; Watanabe, M.; Kurita, A.; Hirata, K.; Yazawa, T.; Kushida, T. Fluorescence and EPR Characteristics of Mn^{2+}–doped ZnS Nanocrystals Prepared by Aqueous Colloidal Method. *J. Phys. Chem. C* **1999**, *103*, 754–760.

[71] Mikulec, F. V.; Kuno, M.; Bennati, M.; Hall, D. A.; Griffin, R. G.; Bawendi, M. G. Organometallic Synthesis and Spectroscopic Characterization of Manganese–doped CdSe Nanocrystals. *J. Am. Chem. Soc.* **2000**, *122*, 2532–2540.

[72] da Silva, R.S.; de Freitas, E.S.; Dantas, N.O. Optical, Magnetic, and Structural Properties of Semiconductor and Semimagnetic Nanocrystals, Nanocrystals – Synthesis, Characterization and Applications, Dr. Sudheer Neralla (Ed.), *InTech*, **2012**, 61–80.

[73] Gupta, A. K.; Kripal, R. EPR and Photoluminescence Properties of Mn^{2+} Doped CdS Nanoparticles Synthesized Via Co–precipitation Method. *Spectrochim. Acta Mol. Biomol. Spectrosc.* **2012**, *96*, 626–631.

[74] Drago, R. S., Physical Methods in Inorganic Chemistry. Reinhold Publishing Corporation: The University of Michigan, 1965.

[75] Beermann, P. A. G.; McGarvey, B. R.; Muralidharan, S.; Sung, R. C. W. EPR Spectra of Mn^{2+}-doped ZnS Quantum Dots. *Chem. Mater.* **2004**, *16*, 915–918.

[76] Beaulac, R.; Ochsenbein, S.; Gamelin, D., Colloidal Transition-Metal-Doped Quantum Dots. In *Nanocrystal Quantum Dots, Second Edition*, Klimov, V., Ed. CRC Press: 2010; pp. 397–453.

[77] Bhattacharyya, S.; Zitoun, D.; Gedanken, A. One-pot Synthesis and Characterization of Mn^{2+}-doped Wurtzite CdSe Nanocrystals Encapsulated with Carbon. *J. Phys. Chem. C* **2008**, *112*, 7624–7630.

[78] Guo, B. C.; Pang, Q.; Yang, C. L.; Ge, W. K.; Yang, S. H.; Wang, J. N. Reverse Micelles Synthesis and Optical Characterization of Manganese Doped CdSe Quantum Dots, *AIP Conf. Proc.* **2005**, *772*, 605–606.

[79] Jian, W. B.; Fang, J. Y.; Ji, T. H.; He, J. B., Quantum-size-effect-enhanced Dynamic Magnetic Interactions Among Doped Spins in $Cd_{1-x}Mn_xSe$ Nanocrystals. *Appl. Phys. Lett.* **2003**, *83*, 3377–3379.

[80] Vela, J. and Hollingsworth, J. A. Semiconductor Nanocrystals: Doped Compositions in *Nanomaterials: Inorganic and Bioinorganic Perspectives*, Encyclopedia of Inorganic Chemistry, 2nd ed., John Wiley & Sons, Ltd., New York, 2008.

[81] Liu, Y.; Yao, D.; Yao, S.; Zhao, J.; Zhang, H.; Tian, W.; Yang, B. Phosphine–free Synthesis of Heavy Co^{2+}– and Fe^{2+}–doped Cu_2SnSe_3 Nanocrystals by Virtue of Alkylthiol–assistant Se Powder Dissolution. *J. Mater. Chem. A* **2013**, *1*, 2748–2751.

[82] Yang, C.; Qin, M.; Wang, Y.; Wan, D.; Huang, F.; Lin, J. Observation of an Intermediate Band in Sn–doped Chalcopyrites with Wide–spectrum Solar Response. *Sci. Rep.* **2013**, 3.

[83] Ji, S.; Shi, T.; Qiu, X.; Zhang, J.; Xu, G.; Chen, C.; Jiang, Z.; Ye, C. A Route to Phase Controllable $Cu_2ZnSn(S_{1-x}Se_x)_4$ Nanocrystals with Tunable Energy Bands. *Sci. Rep.* **2013**, 3.

[84] Jiménez, H. R.; Salgado, J.; Moratal, J. M.; Morgenstern–Badarau, I. EPR and Magnetic Susceptibility Studies of Cobalt(II)– and Nickel(II)–Substituted Azurins from Pseudomonas aeruginosa. Electronic Structure of the Active Sites. *Inorg. Chem.* **1996**, *35*, 2737–2741.

[85] Vinck, E.; Van Doorslaer, S.; Murphy, D. M.; Fallis, I. A. The Electronic Structure of N,N'–bis(3,5–di–tert–butylsalicylidene)–1,2–cyclohexane–diamino Cobalt(II). *Chem. Phys. Lett.* **2008**, *464*, 31–37.

[86] Krivokapic, I.; Zerara, M.; Daku, M. L.; Vargas, A.; Enachescu, C.; Ambrus, C.; Tregenna–Piggott, P.; Amstutz, N.; Krausz, E.; Hauser, A. Spin–crossover in Cobalt(II) Imine Complexes. *Coord. Chem. Rev.* **2007**, *251*, 364–378.

[87] Overnell, J.; Good, M.; VaŠÀK, M. Spectroscopic Studies on Cadmium(II)– and Cobalt(II)–substituted Metallothionein from the Crab Cancer Pagurus. *Eur. J. Biochem.* **1988**, *172*, 171–177.

[88] Maganas, D.; Milikisyants, S.; Rijnbeek, J. M. A.; Sottini, S.; Levesanos, N.; Kyritsis, P.; Groenen, E. J. J. A Multifrequency High–Field Electron Paramagnetic Resonance Study of (CoS_4)–S–II Coordination. *Inorg. Chem.* **2010**, *49*, 595–605.

[89] Fukui, K.; Ohyanishiguchi, H.; Hirota, N. ESR and Magnetic–Susceptibility Studies on High–Spin Tetrahedral Cobalt(II)–Thiolate Complexes – An Approach to Rubredoxin–Type Active–Sites. *Bull. Chem. Soc. Jpn.* **1991**, *64*, 1205–1212.

[90] Park, J. S.; Park, T. J.; Kim, K. H.; Oh, K.; Seo, M. S.; Lee, H. I.; Jun, M. J.; Nam, W.; Kim, K. M., Synthesis and Characterization of High-spin Cobalt(II)-based "Inorgainc Tennis Ball". *Bull. Korean Chem. Soc.* **2006**, *27*, 193–194.

[91] Schubert, H. L.; Rose, R. S.; Leech, H. K.; Brindley, A. A.; Hill, C. R.; Rigby, S. E. J.; Warren, M. J. Structure and Function of SirC from Bacillus Megaterium: a Metal-binding Precorrin-2 Dehydrogenase. *Biochem. J.* **2008**, *415*, 257–263.

[92] Hoffmann, S. K.; Goslar, J.; Lijewski, S. Electron Paramagnetic Resonance and Electron Spin Echo Studies of Co^{2+} Coordination by Nicotinamide Adenine Dinucleotide (NAD^+) in Water Solution. *Appl. Magn. Reson.* **2013**, *44*, 817–826.

[93] Weckhuysen, B. M.; Verberckmoes, A. A.; Uytterhoeven, M. G.; Mabbs, F. E.; Collison, D.; de Boer, E.; Schoonheydt, R. A., Electron Spin Resonance of High-spin Cobalt in Microporous Crystalline Cobalt-containing Aluminophosphates. *J. Phys. Chem. B* **2000**, *104*, 37–42.

[94] Rotilio, G.; Calabres.L; Mondovi, B.; Blumberg, W. E. Electron-paramagnetic Resonance Studies of Cobalt-copper Bovine Superoxide-dismutase. *J. Biol. Chem.* **1974**, *249*, 3157–3160.

[95] Lever, A. B. P.; Gray, H. B. Loss of Hyperfine-structure in Liquid-helium EPR-spectra of Some Cobalt Oxygen Adducts. *J. Mag. Res.* **1978**, *32*, 169–172.

[96] Bennett, B., EPR of Cobalt-Substituted Zinc Enzymes. In *Metals in Biology*, Hanson, G.; Berliner, L., Eds. Springer New York: 2010; 345–370.

[97] Drulis, H.; Dyrek, K.; Hoffmann, K. P.; Hoffmann, S. K.; Weseluchabirczynska, A. Electron-paramagnetic-res Spectra of Low-symmetry Tetrahedral High-spin Cobalt(II) in a Cinchoninium Tetrachlorocoaltate(II) Dihydrate Single-crystal. *Inorg. Chem.* **1985**, *24*, 4009–4012.

[98] Pountney, D. L.; Vasak, M. Spectroscopic Studies on Metal Distribution in Co(II)/Zn(II) Mixed-metal Clusters in Rabbit Liver Metallothionein-2. *Eur. J. Biochem.* **1992**, *209*, 335–341.

[99] Hemsworth, G. R.; Henrissat, B.; Davies, G. J.; Walton, P. H. Discovery and Characterization of a New Family of Lytic Polysaccharide R–nonooxygenases. *Nat. Chem. Biol.* **2014**, *10*, 122–126.

[100] Chory, C.; Zutz, F.; Witt, F.; Borchert, H.; Parisi, J. Synthesis and Characterization of Cu_2ZnSnS_4. *Phys. Status Solidi C* **2010**, *7*, 1486–1488.

[101] Silva, L. A.; de Andrade, J. B.; Mangrich, A. S. Use of Cu^{2+} as a Metal Ion Probe for the EPR Study of Metal Complexation Sites in the Double Sulfite $(Cu_2^ISO_3)•(Cd^{II}SO_3)•2H_2O$. *J. Braz. Chem. Soc.* **2007**, *18*, 607–610.

[102] Valakh, M. Y.; Dzhagan, V. M.; Babichuk, I. S.; Fontane, X.; Perez–Rodriquez, A.; Schorr, S. Optically Induced Structural Transformation in Disordered Kesterite Cu_2ZnSnS_4. *JETP Lett.* **2013**, *98*, 255–258.

[103] Barreca, D.; Massignan, C.; Daolio, S.; Fabrizio, M.; Piccirillo, C.; Armelao, L.; Tondello, E. Composition and Microstructure of Cobalt Oxide Thin Films Obtained from a Novel Cobalt(II) Precursor by Chemical Vapor Deposition. *Chem. Mater.* **2001**, *13*, 588–593.

[104] Krzystek, J.; Park, J. H.; Meisel, M. W.; Hitchman, M. A.; Stratemeier, H.; Brunel, L. C.; Telser, J. EPR spectra from "EPR–silent" Species: High–Frequency and High–field EPR Spectroscopy of Pseudotetrahedral Complexes of Nickel(II). *Inorg. Chem.* **2002**, *41*, 4478–4487.

[105] Maganas, D.; Grigoropoulos, A.; Staniland, S. S.; Chatziefthimiou, S. D.; Harrison, A.; Robertson, N.; Kyritsis, P.; Neese, F. Tetrahedral and Square Planar $Ni[(SPR_2)_2N]_2$ complexes, R = Ph & Pr–i Revisited: Experimental and Theoretical Analysis of Interconversion Pathways, Structural Preferences, and Spin Delocalization. *Inorg. Chem.* **2010**, *49*, 5079–5093.

[106] Matsumura, Y.; Enomoto, Y.; Sugiyama, M.; Akamatsu, K.; Nawafune, H. Direct Metallization of Nickel on Polymeric Template Patterns for Fabrication of Copper Circuits on Glass Substrates. *J. Mater. Chem.* **2008**, *18*, 5078–5082.

[107] Pala, I. R.; Arachchige, I. U.; Georgiev, D. G.; Brock, S. L. Reversible Gelation of II–VI Nanocrystals: The Nature of Interparticle Bonding and the Origin of Nanocrystal Photochemical Instability. *Angew. Chem. Int. Ed.* **2010**, *49*, 3661–3665.

[108] Gacoin, T.; Malier, L.; Boilot, J. P. Sol-gel Transition in CdS Colloids. *J. Mater. Chem.* **1997**, *7*, 859–860.

[109] Kelemen, S. R.; Freund, H. The Application of X–Ray Photoelectron–Spectroscopy (XPS) to Coal Oxidation–Kinetics. *Abstr. Pap. Am. Chem. Soc.* **1988**, *196*, 706–722.

[110] Yin, L.–W.; Ran, L. Highly Crystalline Ti–doped SnO_2 Hollow Structured Photocatalyst with Enhanced Photocatalytic Activity for Degradation of Organic Dyes. *CrystEngComm* **2015**, *17*, 4225–4237.

[111] Rivas, B. L.; Pooley, S. A.; Aceiton, E.; Geckeler, K. E. Synthesis, Characterization, and Properties of a Selective Adsorbent to Mercury(II) Ions. *J. Appl. Polym. Sci.* **2002**, *85*, 2559–2563.

[112] Bandara, J.; Mielczarski, J. A.; Kiwi, J. 1. Molecular Mechanism of Surface Recognition. Azo Dyes Degradation on Fe, Ti, and Al Oxides Through Metal Sulfonate Complexes. *Langmuir* **1999**, *15*, 7670–7679.

[113] Young, A. G.; Al-Salim, N.; Green, D. P.; McQuillan, A. J. Attenuated Total Reflection Infrared Studies of Oleate and Trioctylphosphine Oxide Ligand Adsorption and Exchange Reactions on CdS Quantum Dot Films. *Langmuir* **2008**, *24*, 3841–3849.

[114] Nag, A.; Kovalenko, M. V.; Lee, J.-S.; Liu, W.; Spokoyny, B.; Talapin, D. V. Metal-free Inorganic Ligands for Colloidal Nanocrystals: S^{2-}, HS^-, Se^{2-}, HSe^-, Te^{2-}, HTe^-, TeS_3^{2-}, OH^-, and NH_2^- as Surface Ligands. *J. Am. Chem. Soc.* **2011**, *133*, 10612–10620.

[115] Kyte, J. Structure in Protein Chemistry, 2nd Ed.; Garland Science: New York, 2006.

[116] Pearson, R. G., Absolute Electronegativity and Hardness - Application to Inorganic Chemistry. *Inorg. Chem.* **1988**, *27*, 734–740.

[117] Hancock, R. D.; Martell, A. E., Hard and Soft Acid-base Behavior in Aqueous Solution. *J. Chem. Ed.* **1996**, *73*, 654–661.

Appendix of supporting information
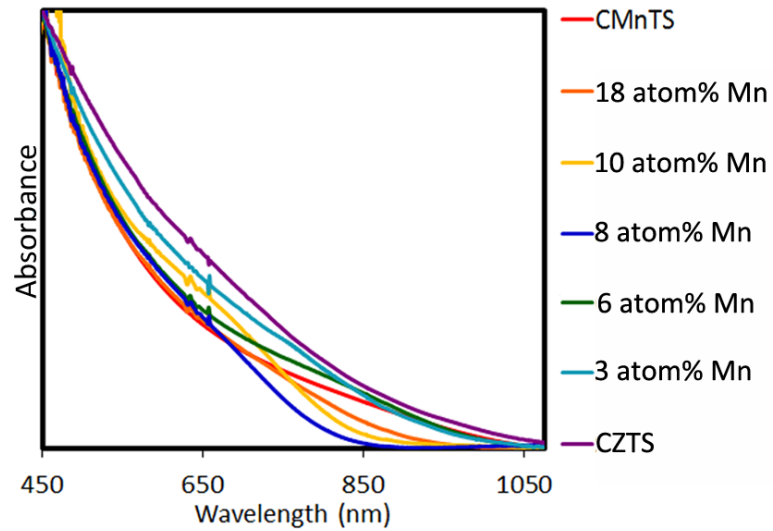
Figure S1. Solution phase optical absorption spectra of manganese(II) doped CZTS nanocrystals.
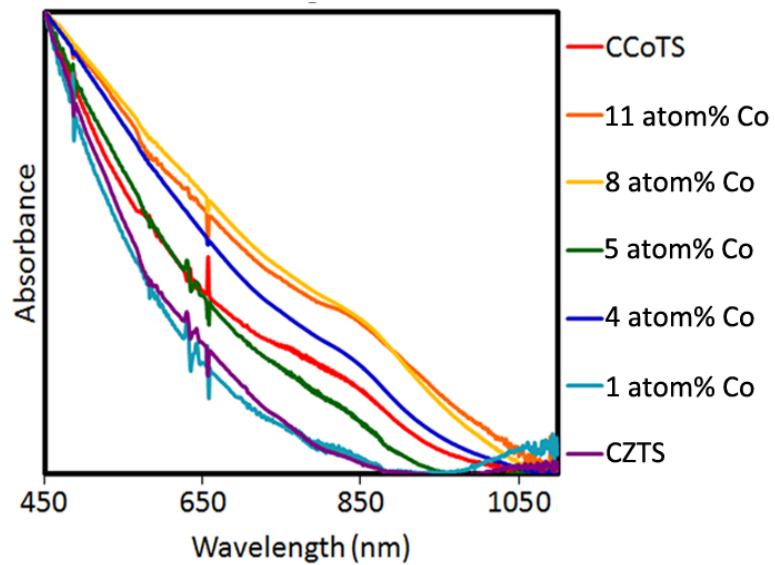
Figure S2. Solution phase optical absorption spectra of cobalt(II) doped CZTS nanocrystals.
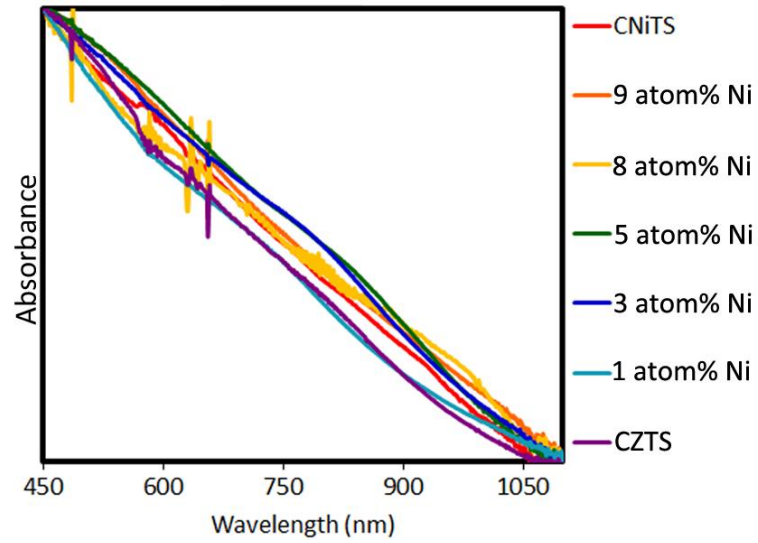
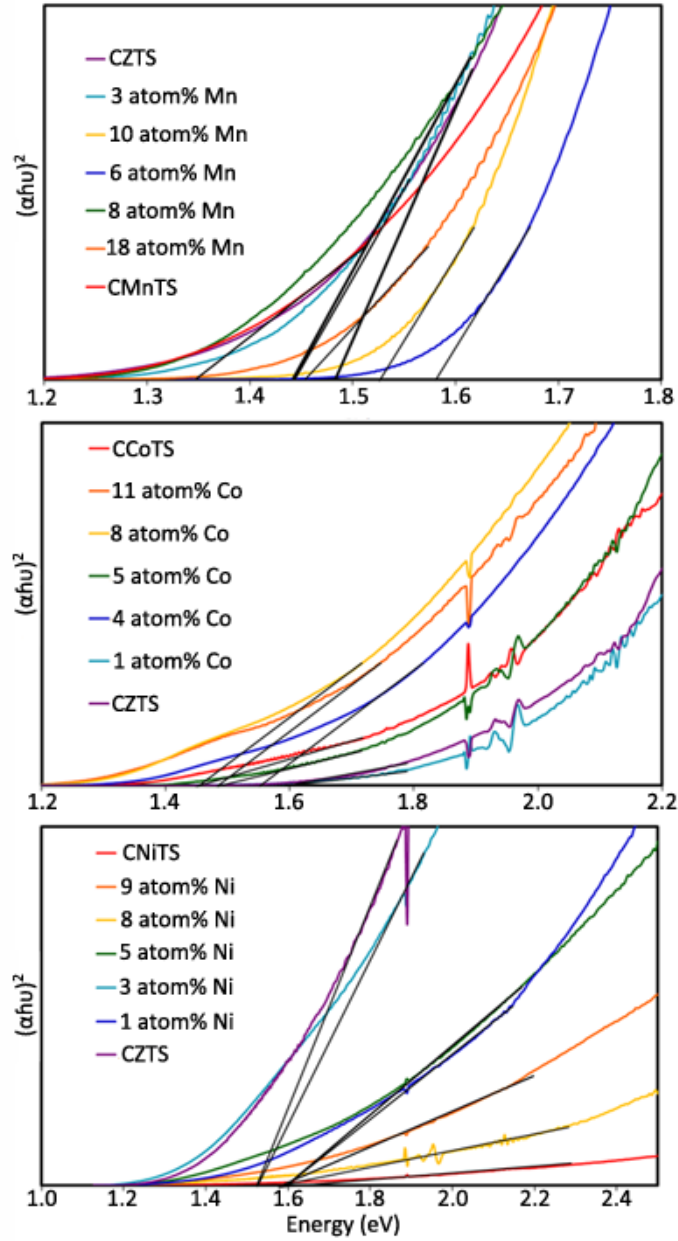**Figure S3.** Solution phase optical absorption spectra of nickel(II) doped CZTS nanocrystals.

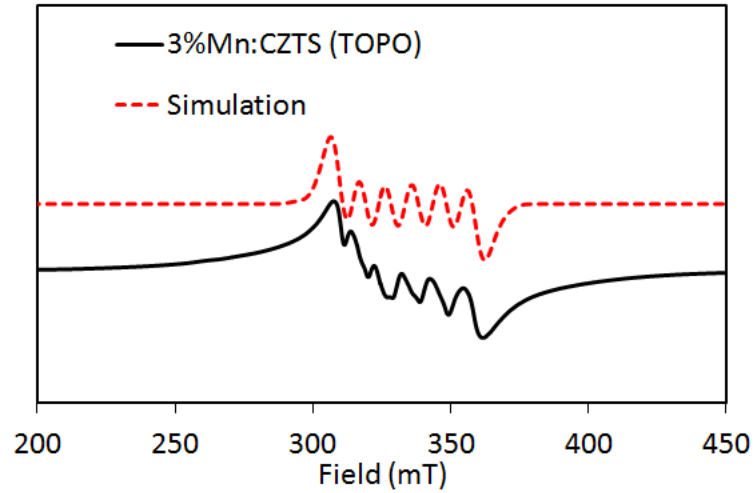**Figure S4.** Tauc plots used to estimate the band edge of transition metal-doped CZTS nanocrystals.

Figure S5. Simulated and experimental EPR spectra of 3 atom% manganese(II) doped CZTS (TOPO wash).
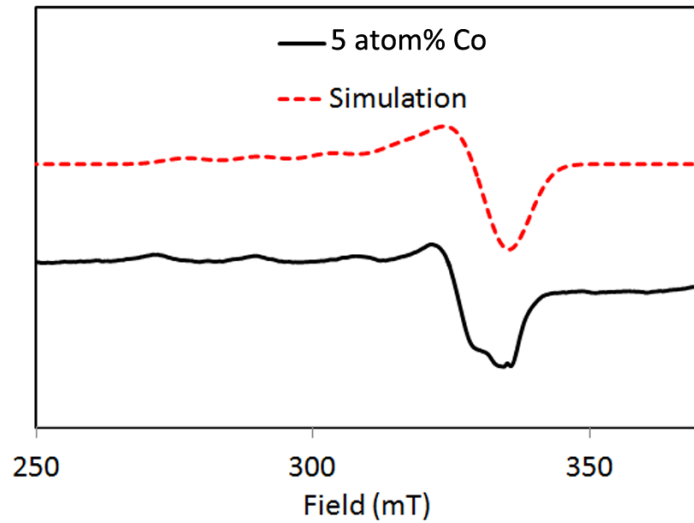
Figure S6. Simulated and experimental EPR spectra of 5 atom% cobalt(II) doped CZTS nanocrystals.
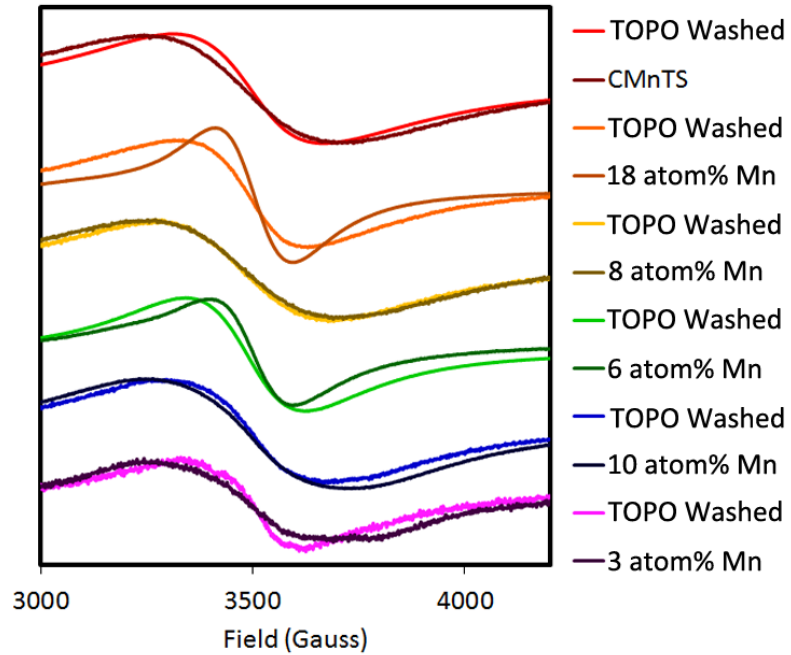
Figure S7. Room temperature (294 K) EPR spectra of manganese(II) doped CZTS nanocrystals.
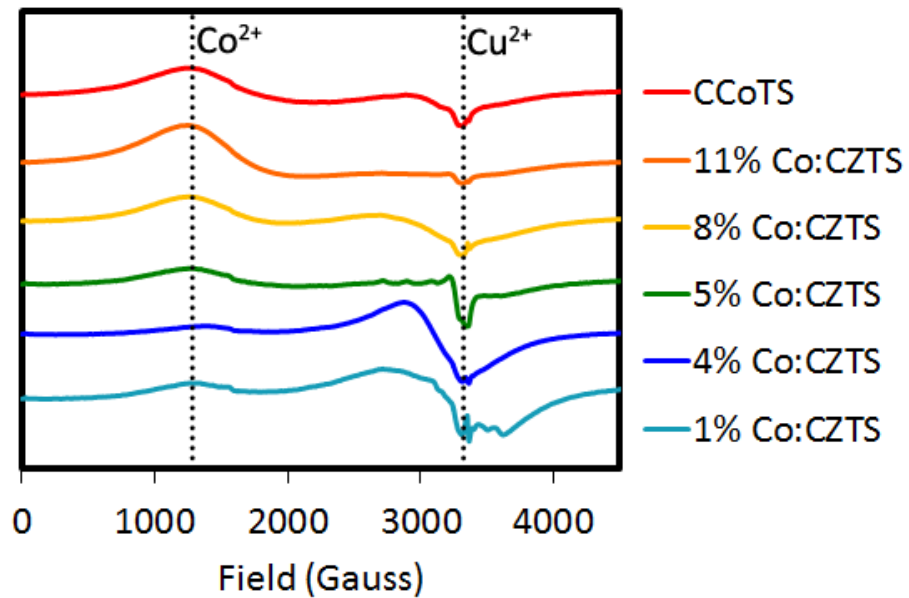
Figure S8. 10 K EPR spectra of cobalt(II) doped CZTS nanocrystals.
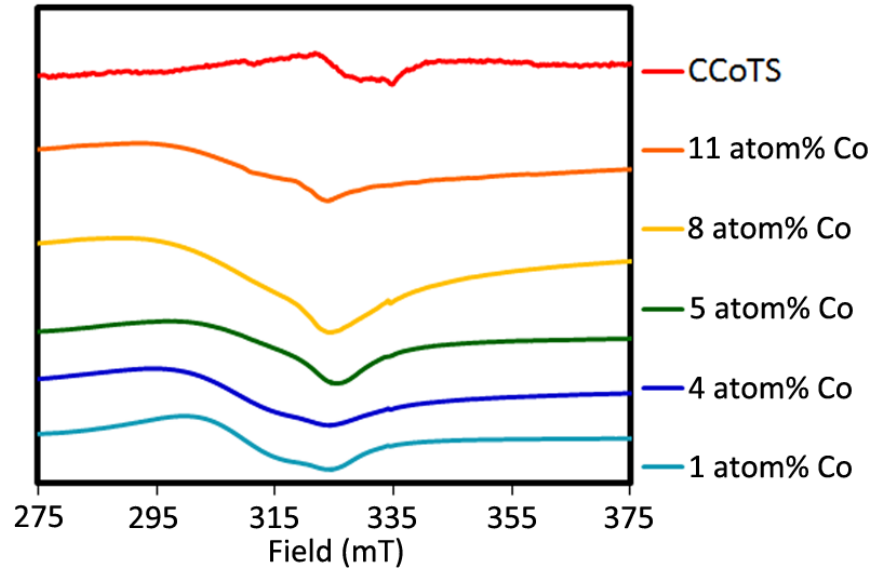
Figure S9. 10 K EPR spectra of cobalt(II) doped CZTS nanocrystals (copper region).
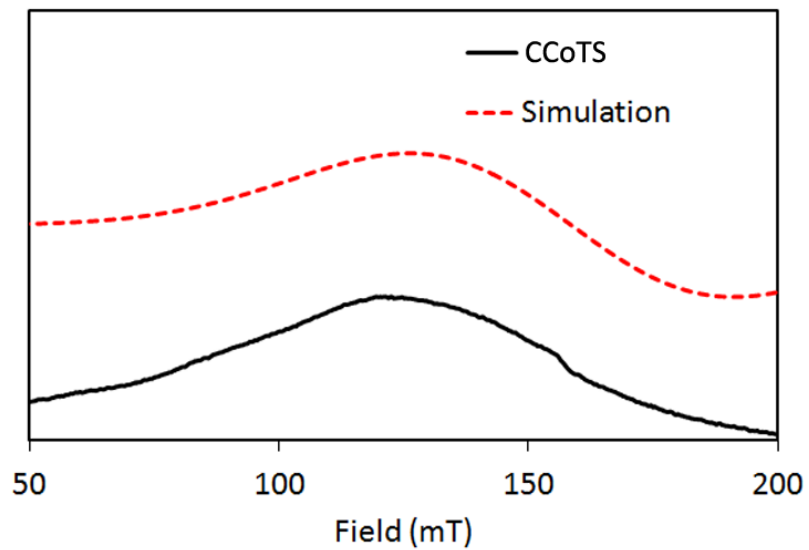
Figure S10. Simulated and experimental EPR spectra of CCoTS nanocrystals.
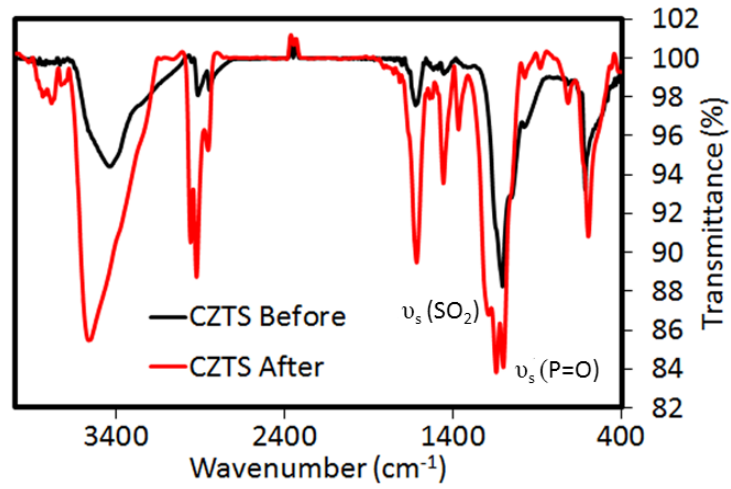
Figure S11. FTIR spectra of CZTS nanocrystals before (black) and after (red) thiol wash with a 1:7 mixture of 1-dodecanethiol and tert-dodecylmercaptan.
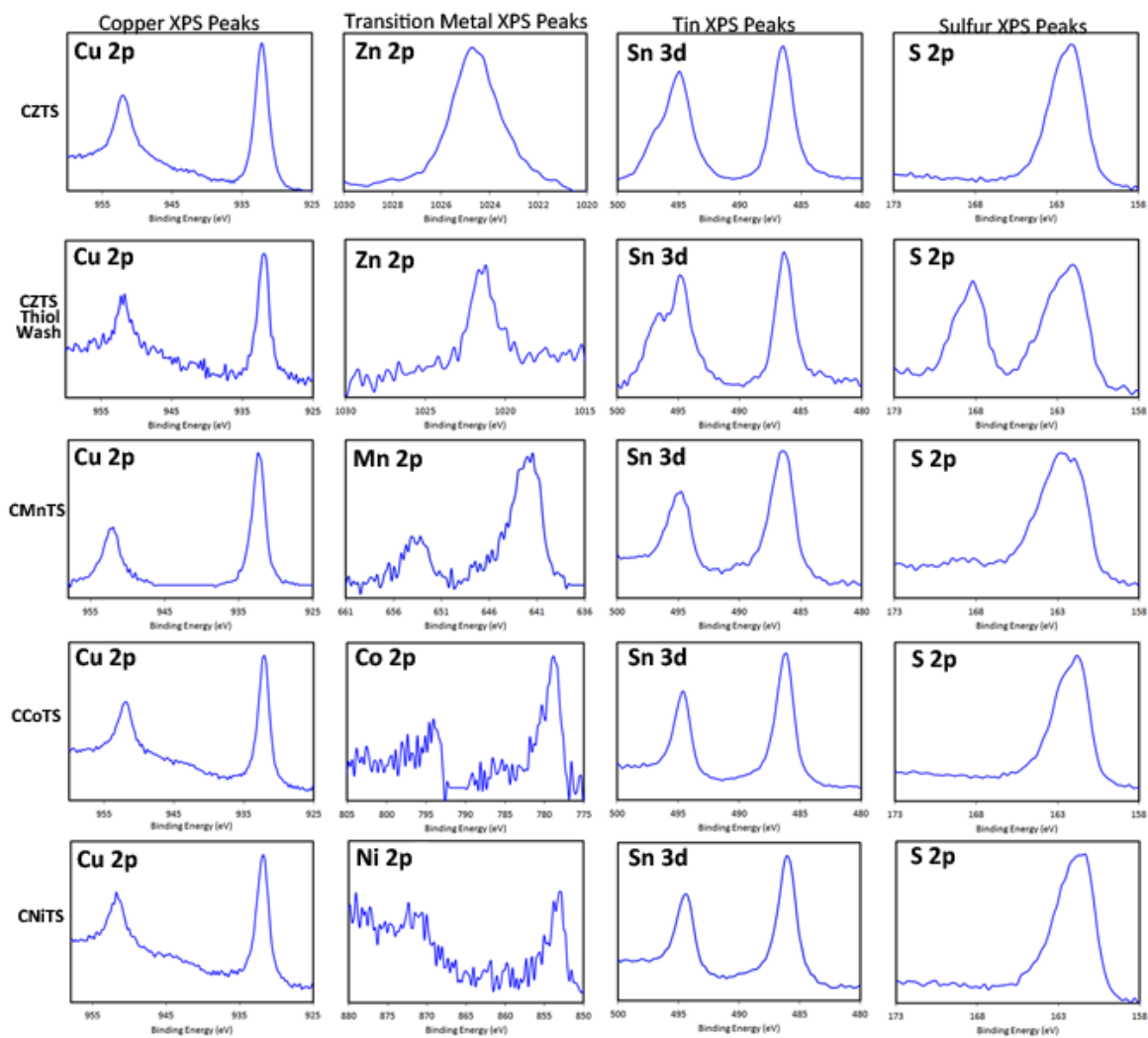
Figure S12. XPS analysis of CZTS, thiol washed-CZTS, CMnTS, CCoTS, and CNiTS nanocrystals.
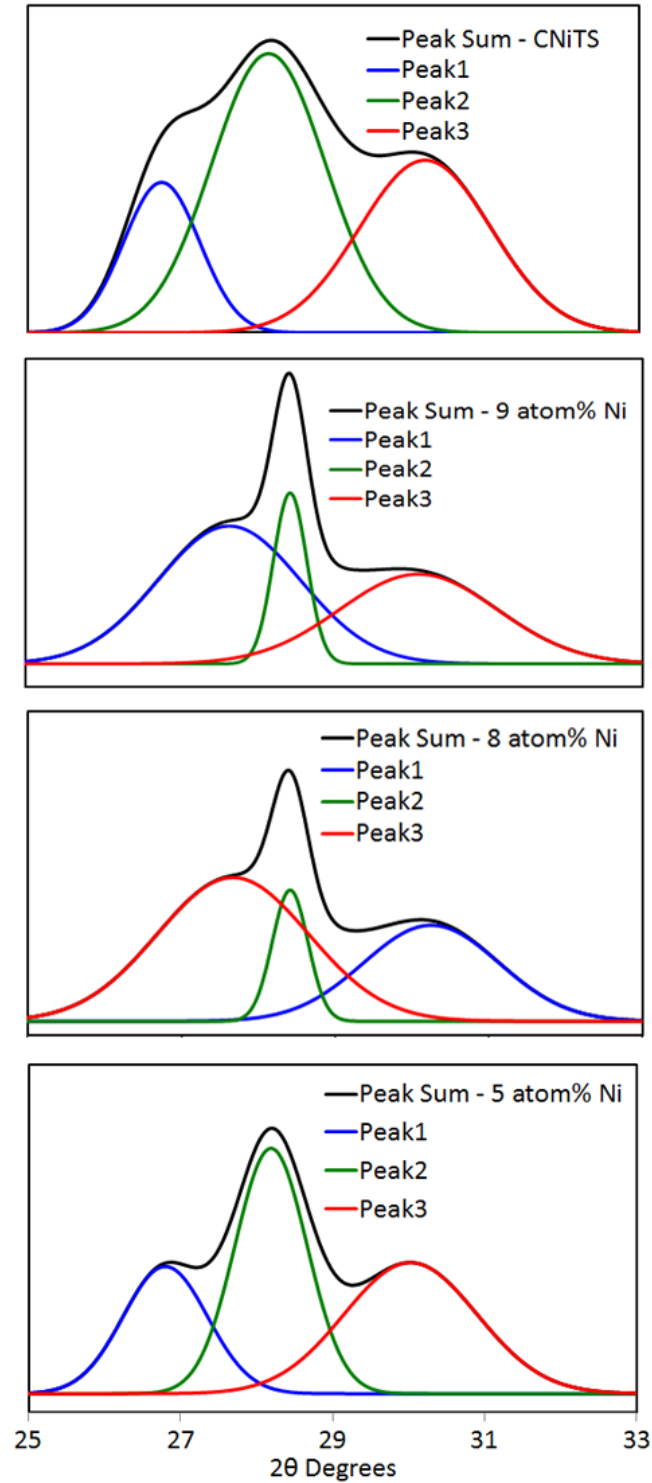
Figure S13. Deconvolution of (100), (002) and (101) diffraction peaks from the PXRD patterns of Ni(II) doped CZTS.
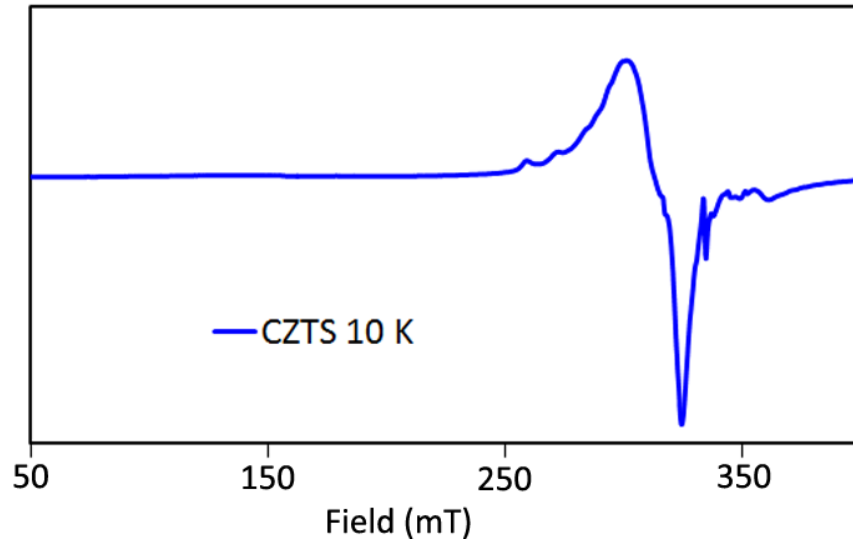
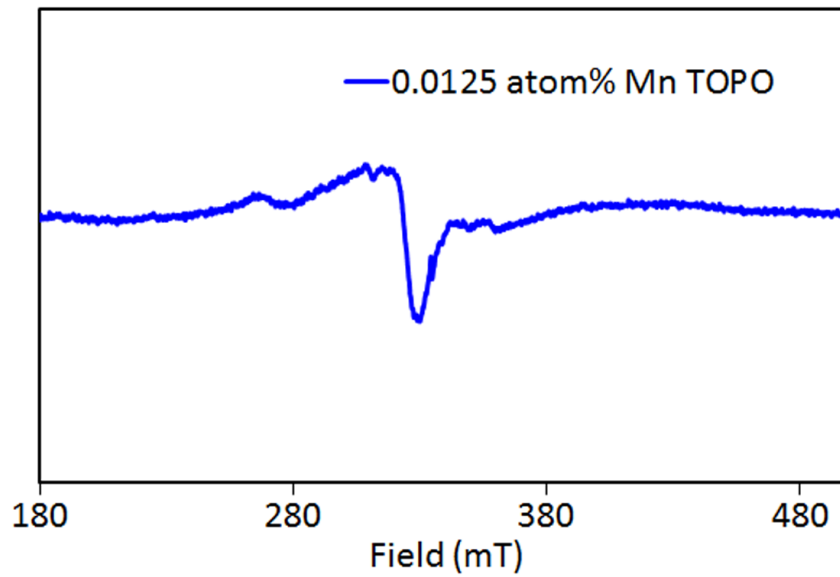**Figure S14**. EPR spectrum of undoped CZTS at 10 K.

Figure S15. EPR spectrum of 0.0125 atom% Mn:CZTS at 10 K.

Table S1. Comparison of EPR parameters.		
System	**Reported Value**	**Reference**
Tetracoordinate Mn^{2+}		
3 atom% Mn:CZTS	$A = 68 \times 10^{-4}$ cm^{-1} $g = 2.0055$ $D = 31 \times 10^{-4}$ cm^{-1}	this work
$Cd_{0.994}Mn_{0.006}Se$	$A = 65 \times 10^{-4}$ cm^{-1}	[53]
Internal Mn - 0.7% Mn:CdS - tetrahedral Surface Mn - 0.7% Mn:CdS - octahedral	$A = 68 \times 10^{-4}$ cm^{-1} $g = 2.0049$ $A = 89 \times 10^{-4}$ cm^{-1} $g = 2.0052$	[73]
internal Mn -0.003% Mn:ZnS - tetrahedral	$A = 64 \times 10^{-4}$ cm^{-1} $D = 37.4 \times 10^{-4}$ cm^{-1}	[75]
Internal Mn - $Cd_{0.9}Mn_{0.1}Se$ Surface Mn- $Cd_{0.9}Mn_{0.1}Se$	$A = 60 \times 10^{-4}$ cm^{-1} $g = 2.010$ $A = 85 \times 10^{-4}$ cm^{-1} $g = 2.0021$	[78]
$Cd_{0.97}Mn_{0.03}Se$	$A = 85 \times 10^{-4}$ cm^{-1}	[79]
Internal Mn - $Cd_{0.994}Mn_{0.006}Se$ - tetrahedral Surface Mn - $Cd_{0.994}Mn_{0.006}Se$	$A = 63 \times 10^{-4}$ cm^{-1} $D = 15 \times 10^{-4}$ cm^{-1} $A = 85 \times 10^{-4}$ cm^{-1} $D = 0$ cm^{-1}	[69]
Tetracoordinate Co^{2+}		
CCoTS	$g = 4.3$	this work
Co/NAD$^+$	$g = 4.3$	[92]
CoAPO-*n*	$g = 5.44$	[93]
Cobalt bovine superoxide dismutase	$g = 4.3$	[94]
Tetracoordinate Cu^{2+}		
Cu^{2+} in CCoTS	$g_{\parallel} = 2.26$ $g_{\perp} = 2.025$ $A_{\perp} = 16 \times 10^{-4}$ cm^{-1} $A_{\parallel} = 133 \times 10^{-4}$ cm^{-1}	this work
$(Cu_2^{I}SO_3) \cdot (Cd^{II}SO_3) \cdot 2H_2O$ (contains distorted tetrahedral and octahedral sites)	$g_{\parallel} = 2.37$ $g_{\perp} = 2.080$ $A_{\perp} = 15 \times 10^{-4}$ cm^{-1} $A_{\parallel} = 158 \times 10^{-4}$ cm^{-1}	[101]
Undoped CZTS		
CZTS	$g_{\perp} = 2.006$	[100]

Table S2. Band gaps of 'parent' compounds.		
Species	**Reported Band Gap**	**Ref.**
CZTS	1.5	this work
	1.4 – 1.56	[4]
	1.5	[7]
CMnTS	1.3 eV	this work
	1.1 eV	[39]
	1.28 eV	[16]
CCoTS	1.4 eV	this work
	1.25 eV	[16]
	1.5 eV	[13]
CNiTS	1.6 eV	this work
	1.41 eV	[17]
	1.49 eV	[16]
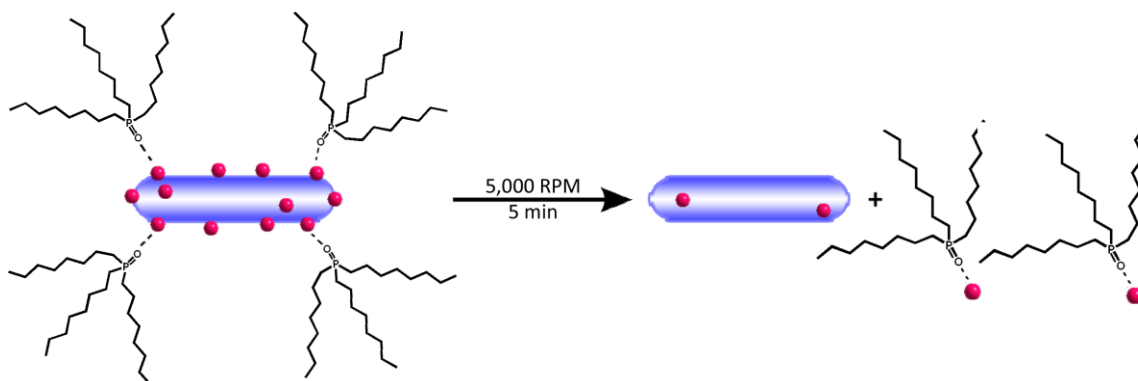
Scheme S1. TOPO washing to remove surface bound manganese ions.
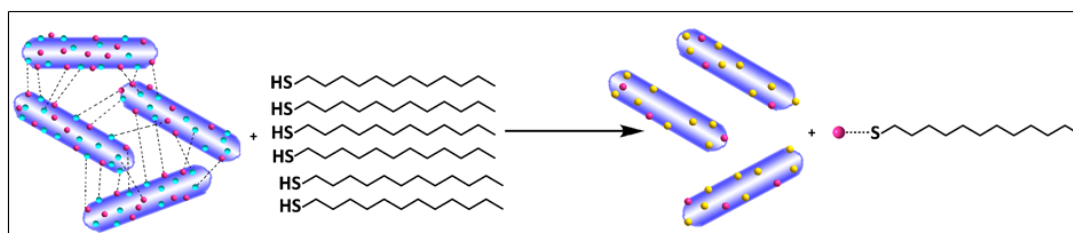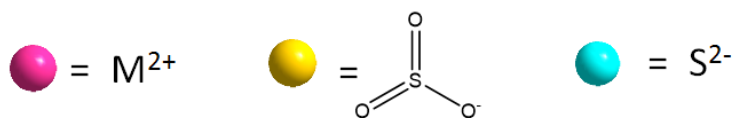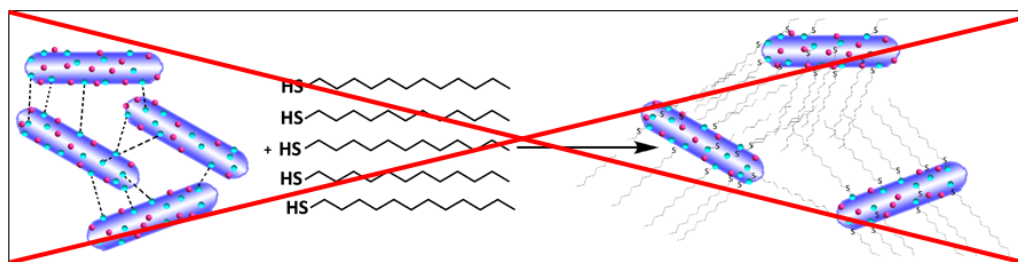
Scheme S2. Thiol washing of nanorods to reduce aggregation due to crosslinking of metal ions with terminal surface sulfides. Additional thiols bond with metal ions, leaving surface terminal sulfides free to oxidize in air, forming sulfonates.

CHAPTER 4

SYNTHESIS AND CHARACTERIZATION OF TERNARY THIOSPINEL AND PYRITE NANOPARTICLES

Michelle Thompson, Brittany Hallmark, Courtney Meekins, Javier Vela

Abstract

Due to their application in a variety of energy and catalysis fields, thiospinels and pyrites have attracted attention in recent years. Typically, these materials are synthesized in bulk, with high temperature methods and low surface areas, making them less than ideal for applications. In this report, we use low temperature, solvothermal methods to synthesize nanocrystalline, ternary thiospinels. The nanocrystals have a variety of morphologies, including spheres and nanorods, and show a broad absorbance in the visible range. This is the first time several of the materials are reported in nano sizes. We also report on the attempted synthesis of pyrite nanocrystals.

Introduction

Spinel compounds, with a typical formula AB_2X_4 can show many different, interesting properties using various combinations of A, B, and X. Thiospinels are one type of spinel, with a formula of AB_2S_4. In a thiospinel structure, sulfur atoms are in a cubic close-packed arrangement with A^{2+} cations occupying 8 tetrahedral sites and B^{3+} cations occupying 16 octahedral sites. As with spinels, thiospinels show a range of interesting magnetic and electrical properties – most have been shown to possess an antiferromagnetic ground state,[2] while some thiospinels are magnetic semiconductors[3],

and others show metallic behavior with complicated magnetic properties. Studies of thiospinels have led to interesting discoveries, such as their photosensitivity and transparency to high energy photons,[4] as well as their anisotropic pressure dependent properties, which could lead to applications in defect engineering.[5] Thiospinels have shown promise for a variety of applications, such as supercapacitors,[6,7] anodes for lithium ion batteries,[1] and catalysts for the oxygen reduction reaction.[8]

Pyrites are another interesting type of crystalline compound. Binary transition metal pyrites have been extensively studied, but ternary pyrite systems have received less attention, with only a few computational reports,[9,10] and reports of doped bulk systems.[11-15] Pyrites have an AX_2 formula, where cations (A) form a face centered cubic arrangement with octahedral coordination to X, and X forms covalently bonded pairs which are parallel to the cube's diagonals. The most common pyrites are composed of a single metal (A = B) and sulfur, such as nickel, iron, or cobalt.[1] Pyrites have been studied for their applications in photovoltaics,[23,26,27] thermoelectrics,[16,17] spin-tronics[18], and catalysis.[19]
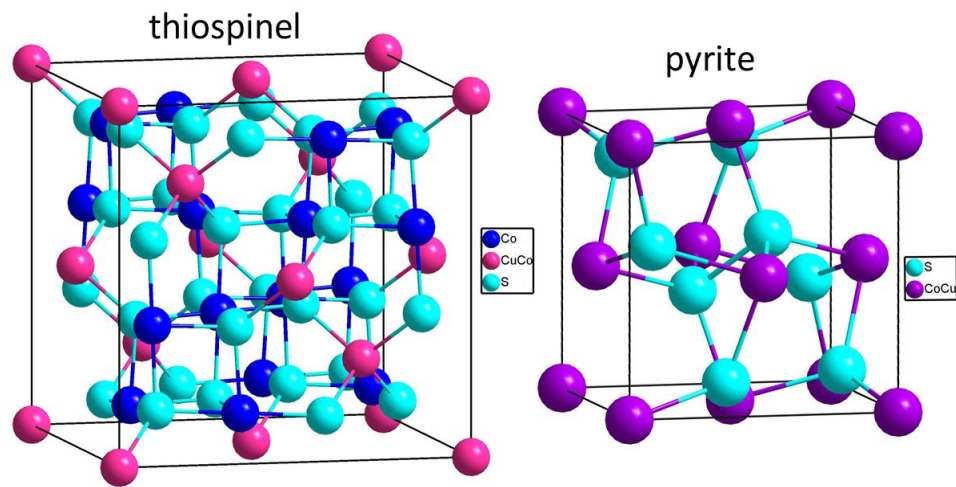

Figure 1. Unit cells of thiospinel and pyrite crystal structures

In this report, we explore the synthesis of several nanoscale thiospinels, namely $CuCo_2S_4$, $CuCo_5S_8$, and $NiCo_2S_4$. While $NiCo_2S_4$ has been heavily explored in both the bulk and nano regimes due to its application as a supercapacitor,[20-22] there are very few reports of $CuCo_2S_4$ in nano sizes[23,24] and to the best of our knowledge, this is the first report of $CuCo_5S_8$ in nano sizes. Bulk $CuCo_2S_4$ has been successfully utilized as a reversible cathode in lithium battery systems since the discovery in the early 1980's,[25-27] and has also been extensively studied for its magnetic and electronic properties.[10,28-30] We also report on the synthesis and characterization of $CuNiCoS_4$, $CuNi_{1.5}Co_{0.5}S_4$, and $CuNi_{0.5}Co_{1.5}S_4$, which, to the best of our knowledge, have also never been reported in nano sizes, with only one report in the literature on bulk sizes.[31] Additionally, we explored the synthesis of several pyrite compounds; $CuNi_3S_8$, $CuCoS_4$, Cu_3ZnS_8, and $CuMn_3S_8$.

Experimental

Materials Copper(II) acetylacetonate (99.99%), 1-dodecanethiol (98+%), tert-dodecylthiol (98.5%), nickel(II) acetate tetrahydrate (99+%), cobalt(II) tetrahydrate (99+%) oleylamine (70%) and trioctylphosphine oxide (TOPO) (99%) were purchased from Sigma Aldrich; zinc(II) acetate dihydrate (98+%), and manganese(II) acetate tetrahydrate (99+%) from Strem Chemicals, and 1-octadecene (ODE) (90%) from Acros. All materials were used as received.

Synthesis. All thiospinels were synthesized by a modified literature procedure.[32,33] In the reaction, transition metal salts and trioctylphosphine oxide (TOPO) (1.75 mmol) were mixed with ODE (5 mL) in a three-neck, round bottom flask and

evacuated at room temperature for 30 min. The flask was heated to 120 °C, and a mixture of 1-dodecanethiol (0.52 mmol) and tert-dodecylthiol (3.72 mmol) was quickly injected. After additional heating to 210 °C for 30 min with continuous stirring, the solution was allowed to cool to 80 °C, and anhydrous toluene (1.5 mL) added. Brown/black colored solids (nanocrystals) were isolated by repeated precipitation with a mixture of ethanol and methanol, and centrifugation at 5000 rpm for 8 min, followed by re-dissolution in toluene. *$CuCo_2S_4$ and $CuCo_5S_8$*: copper(II) acetylacetonate (0.25 mmol) and cobalt(II) acetate tetrahydrate (0.5 or 1.25 mmol). *$NiCo_2S_4$*: cobalt(II) acetate tetrahydrate (0.5 mmol) and Ni(II) acetate tetrahydrate (0.25 mmol). *$CuNiCoS_4$, $CuNi_{1.5}Co_{0.5}S_4$, and $CuNi_{0.5}Co_{1.5}S_4$*: cobalt(II) acetate tetrahydrate (0.25, 0.375, or 0.125 mmol) and Ni(II) acetate tetrahydrate (0.25, 0.375, or 0.125 mmol) and copper(II) acetylacetonate (0.25 mmol). *Thiol Wash.* In order to reduce nanoparticle aggregation, we employed a wash using excess thiols. Briefly, approximately 0.4 mL of a 1:7 mixture of 1-dodecanethiol and tert-dodecylthiol was added to approximately 5 mL of nanoparticles dispersed in toluene. After sonication for 1 h, the particles were washed once with ethanol and methanol and centrifuged at 5000 rpm for 8 min. *Pyrite synthesis*. $CuCoS_4$ was attempted using a modified literature report.[11] Copper(II) acetylacetonate (0.25 mmol), cobalt(II) acetate (0.25 mmol), TOPO (0.3 mmol) and OLAM (10 mL) were degassed at 120°C for 1 hour. The temperature was increased to 170°C and the solution was refluxed for 2 hours. The temperature was increased to 220°C and 0.6M sulfur in OLAM (5 mL) was injected. The solution was stirred at 220°C for 2 hours, then cooled. The product was isolated by repeated precipitation with a mixture of methanol, ethanol, and isopropanol, and centrifugation at 5000 rpm for 8 minutes, followed by re-dissolution in toluene.

Photochemical synthesis. Unwashed (crude) $CuCo_2S_4$ nanoparticles (0.2 mL) were dispersed in toluene (4.75 mL) and illuminated under 380 nm light. Additional thiols (0.1 mL) and copper(II) acetylacetonate (0.0163 g) were added in one synthesis, and EDTA (0.1461 g in 5 mL toluene) was added in another.

Characterization. *Powder X-ray diffraction* (XRD) were measured using Cu Kα radiation on a Rigaku Ultima IV diffractometer. A standard pattern of wurtzite (hexagonal) ZnS was used in lieu of that of wurtzite CZTS (unknown). *Transmission Electron Microscopy* (TEM) was conducted on carbon-coated nickel or gold grids using a FEI Tecnai G2F20 field emission scanning transmission electron microscope (STEM) at 200 kV (point-to-point resolution <0.25 nm, line-to-line resolution <0.10 nm). The nanorods' axial elemental composition was characterized using energy-dispersive spectroscopy (EDX) line scans in STEM mode. Atom% values were determined by averaging five EDX scans of representative areas within each sample. *Particle sizes* (dimensions) and statistics (>100 particles) were measured manually using ImageJ. Average sizes are reported with ± 1 standard deviations. *Optical absorption spectra* were measured with a photodiode array Agilent 8453 UV-Vis-NIR spectrophotometer. Solvent absorption was subtracted from all spectra.

Results and discussion

Synthesis of ternary pyrites. Along with the ternary thiospinel nanocrystals, we were interested in ternary pyrite nanocrystals. We attempted to synthesize several different ternary pyrites, including: $CuNi_3S_8$, $CuCoS_4$, Cu_3ZnS_8, and $CuMn_3S_8$. We began with a routine, hot-injection, solvothermal synthesis (scheme 1), which was unsuccessful. We altered the synthetic conditions (time, temperature, metal precursor, and solvent(s))

and tried several different photochemical methods. However, none of the methods we tried were successful. In the case of $CuNi_3S_8$, regardless of the reaction time, temperature, sulfur source, or alteration of the metal sources, the product was nearly always a mixture of α-NiS and β-NiS (Figure 2). The UV-Visible solution phase absorbance showed very little; likely due to scattering, since the products were only partially soluble.
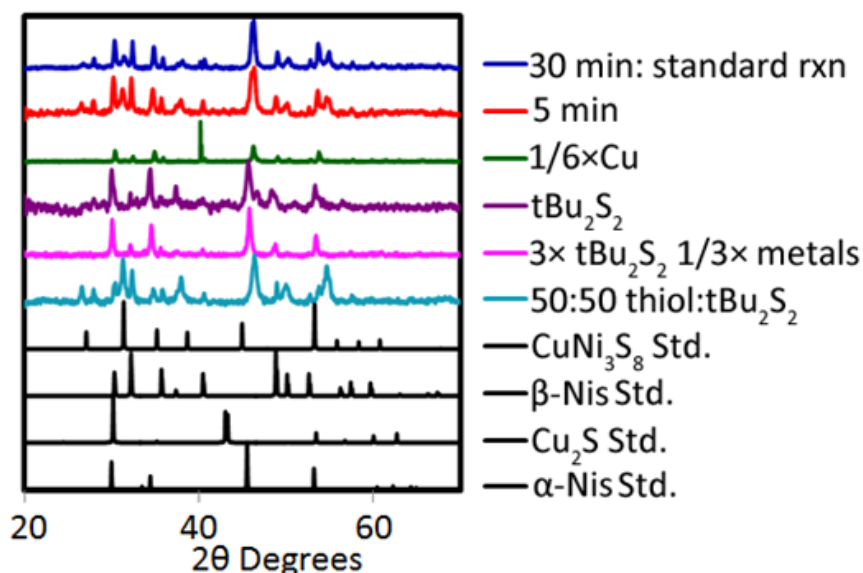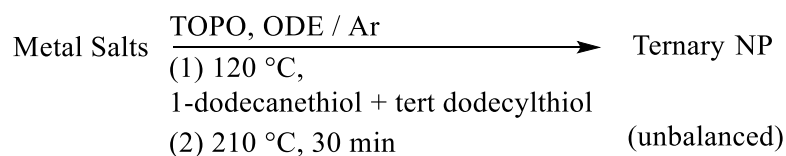
Scheme 1. Synthesis of the nanoparticles using a hot-injection.

Metal Salts $\xrightarrow[\substack{(1)\ 120\ °C, \\ 1\text{-dodecanethiol} + \text{tert dodecylthiol} \\ (2)\ 210\ °C,\ 30\ \text{min}}]{\text{TOPO, ODE / Ar}}$ Ternary NP

(unbalanced)

Figure 2. PXRD of attempts to synthesize ternary pyrite $CuNi_3S_8$ nanocrystals.

Attempts to synthesize Cu_3ZnS_8 yielded crystalline copper sulfide phases and ZnS (Figure 3). The solution phase absorbance was featureless, with an onset around 600 nm. Synthesis of $CuMn_3S_8$ showed only MnS as the product by PXRD (Figure 4) with an unknown impurity phase. The absorbance was broad and featureless, spanning from 200-1100 nm.
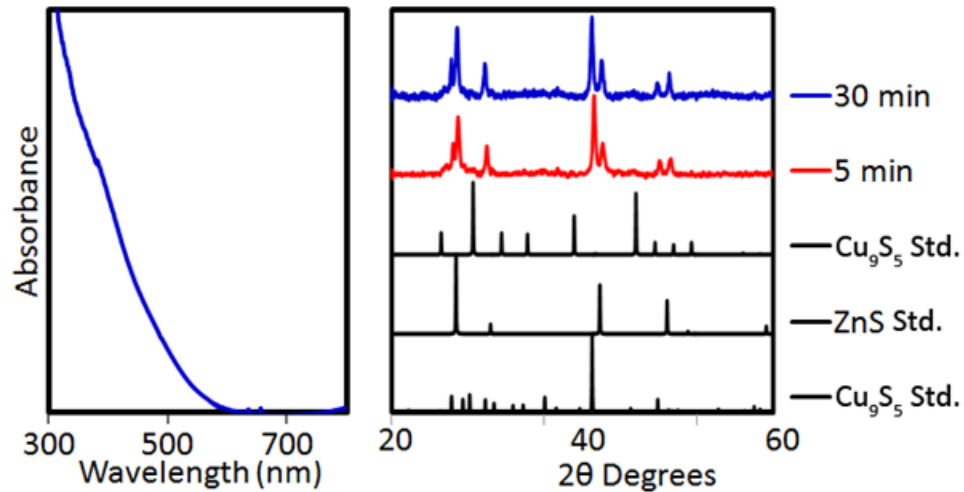
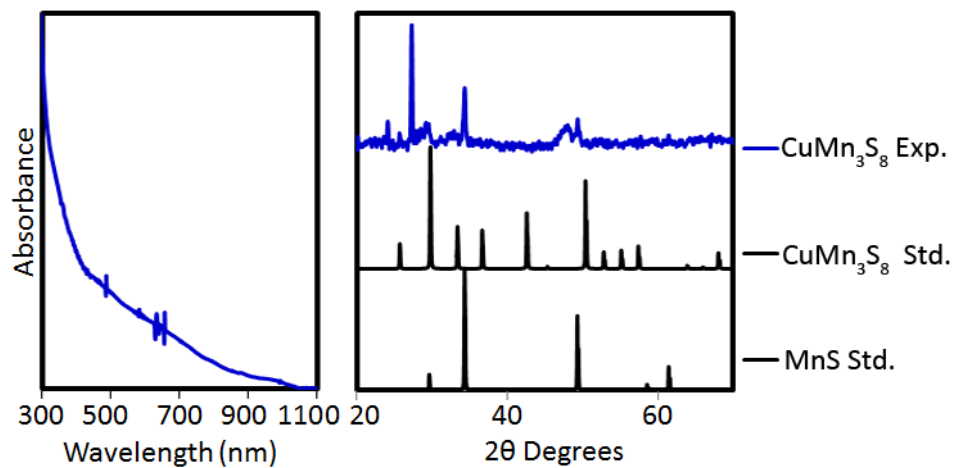**Figure 3.** UV-Visible solution phase absorption and PXRD of attempted synthesis of ternary pyrite Cu_3ZnS_8 nanocrystals.

Figure 4. UV-Visible solution phase absorption and PXRD of attempted synthesis of ternary pyrite $CuMn_3S_8$ nanocrystals.

The attempted syntheses of $CuCoS_4$ also proved unsuccessful, regardless of preparation method, precursor choice, or precursor ratio. While we began with the optimized hot injection method used earlier, we also pursued a published method for pyrite preparation,[11] shown in Scheme 2. We also varied the sulfur source and initial loading of sulfur and metal precursors, with no success. Photochemical synthesis was also unsuccessful. As shown in figure 5, nearly every synthesis route produced the thiospinel compound $CuCo_2S_4$.

Scheme 2. Reaction scheme for pyrite prep synthesis for $CuCoS_4$

$$Cu(acac)_2 + Co(OAc)_2 \cdot H_2O \xrightarrow[\substack{(1)\ 170°C\ 2\ h \\ (2)\ 220°C\ 5mL\ 0.6\ M\ S\ in\ OLAM \\ (3)\ 220°C\ 2\ h}]{OLAM,\ TOPO/Ar} CuCoS_4$$
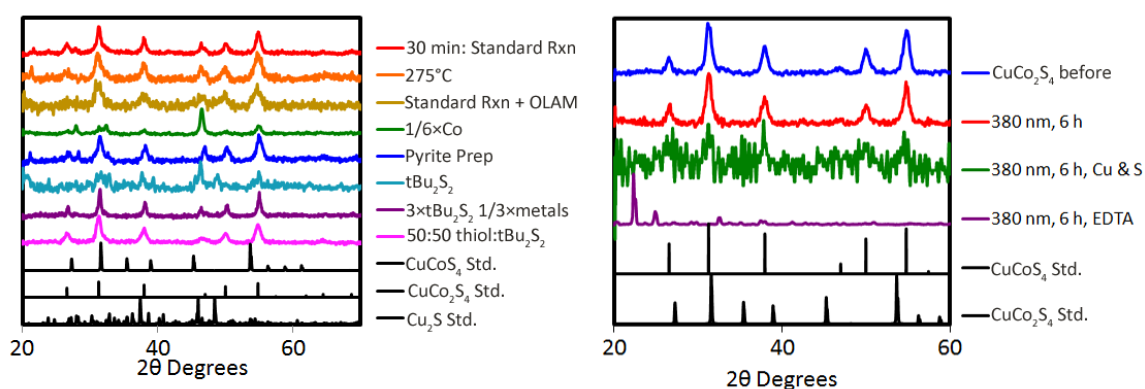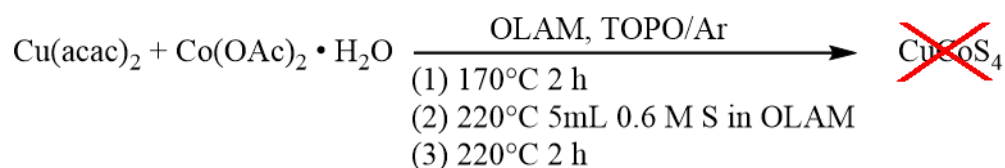
Figure 5. PXRD of attempted hot injection synthesis (left) and photochemical synthesis (right) of ternary pyrite $CuCoS_4$ nanocrystals.

Synthesis of CuMn₂S₄ and CuZn₂S₄. In addition to these compounds, we also attempted to synthesize thiospinel $CuMn_2S_4$ and $CuZn_2S_4$ nanocrystals. We began with a stoichiometric synthesis of $CuMn_2S_4$, and then also modified the synthesis with different precursor ratios. Regardless of the modifications, the majority end product was consistently MnS (Figure 6), and several syntheses also yielded copper sulfide and sulfur as minor components. TEM images show that the nanocrystals made by stoichiometric synthesis were spherical with an average diameter of 8 ± 1 nm (Figure 7). We also tried to synthesize $CuZn_2S_4$, which yielded ZnS (hexagonal) nanocrystals and a small amount of copper sulfide as the end products (Figure 8). The nanocrystals were cone shaped, with an average length of 28 ± 6 nm (Figure 9).
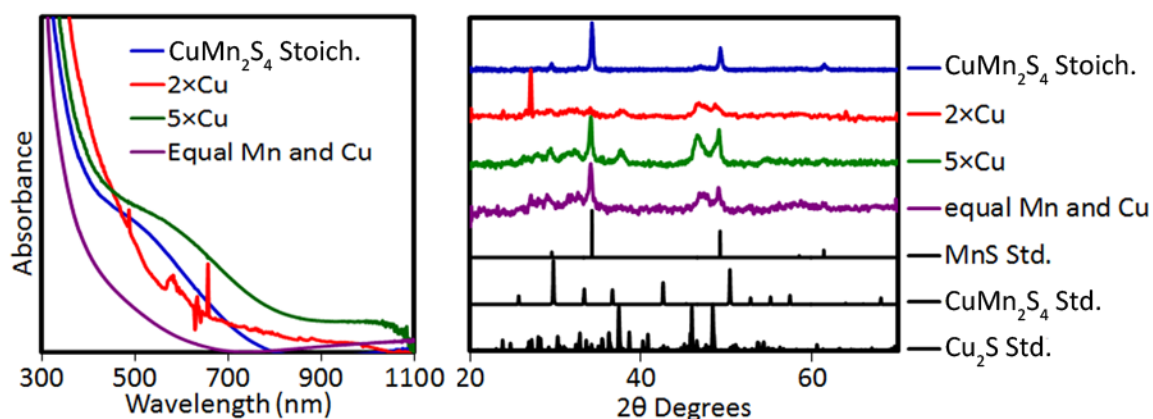
Figure 6. UV-Visible solution phase absorption and PXRD of attempts to synthesize $CuMn_2S_4$.
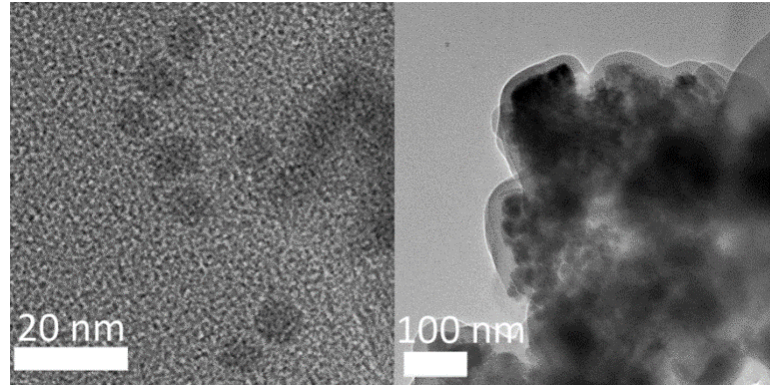
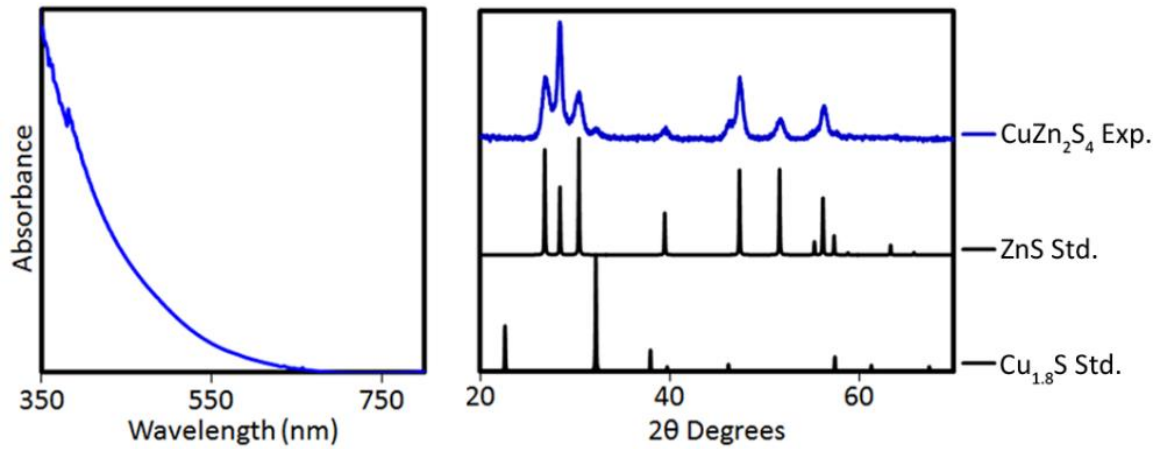**Figure 7.** TEM images of nanocrystalline product from stoichiometric attempt to synthesize $CuMn_2S_4$

Figure 8. UV-Visible solution phase absorbance and PXRD of $CuZn_2S_4$ synthesis.
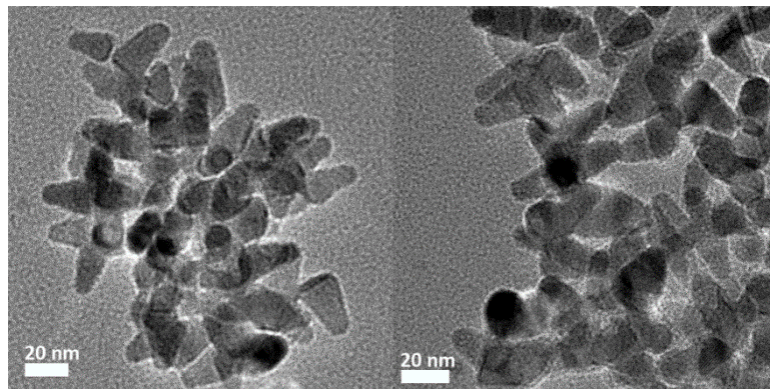

Figure 9. TEM images of Nanocrystalline product of attempted synthesis of $CuZn_2S_4$

Synthesis and Characterization of CuCo2S4. During synthesis of Cu_2CoSnS_4 nanocrystals, an impurity phase appeared in the powder x-ray diffraction pattern. That phase was characterized as $CuCo_2S_4$, a ternary thiospinel called Carrollite, which is a naturally occurring metallic thiospinel. Following this discovery, we deliberately synthesized the ternary compound using a hot injection synthesis that was optimized in the second chapter. Briefly, the particles were synthesized by mixing metal salts with TOPO, injecting excess thiol at 120°C, followed by 30 minutes of heating at 210°C (Scheme 2). The product was dark brown/black in color.
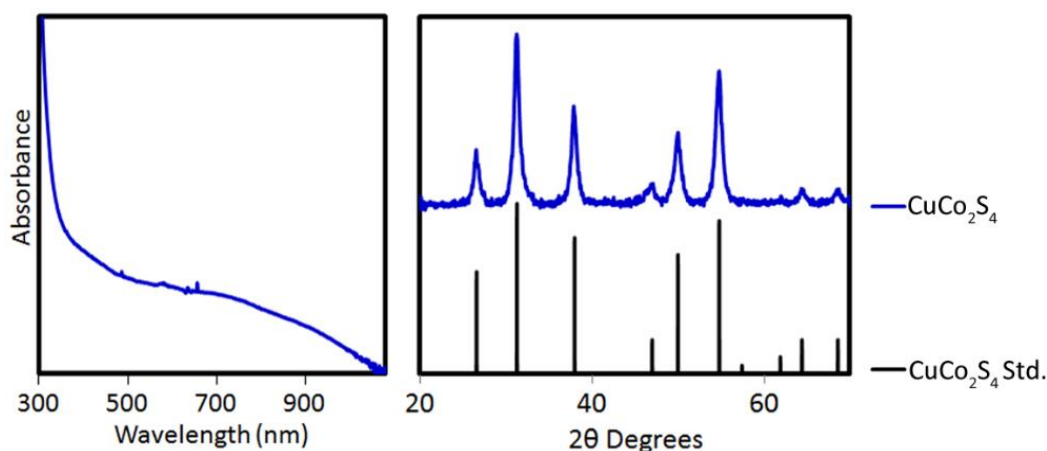

Figure 10. UV-Visible solution phase absorption and PXRD of $CuCo_2S_4$ nanocrystals

The powder XRD pattern showed that the product was crystalline, with an average diameter of 11 nm (calculated using the Scherrer equation). UV-Vis solution phase absorbance showed a broad absorption over the range from 200 – 1000 nm (Figure 10). Transmission electron microscopy (TEM) showed significant aggregation of nanocrystals, so we employed a thiol 'wash' to reduce aggregation of the particles. In this

wash, we take the as-synthesized particles and centrifuge (wash) with ethanol and toluene twice. Then we dispersed the particles in toluene and add 0.4 mL of a mixture of 1-DDT and t-DDT and sonicate for 30 minutes.
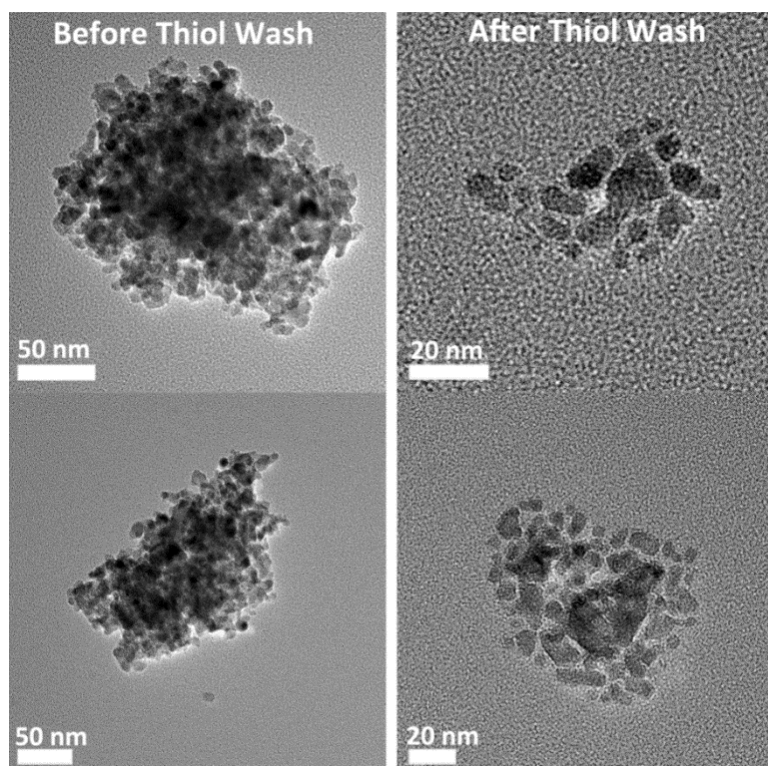

Figure 11. TEM images of $CuCo_2S_4$ before (left) and after (right) thiol washing to reduce aggregation.

After the additional thiol wash, the nanocrystals were much less aggregated and showed a spherical morphology with an average diameter of 9 ± 4 nm, which corresponds well with the size calculated from the PXRD (Figure 11). Energy dispersive x-ray spectroscopy (EDX) shows that the molar ratio of Cu:Co:S is 1:2:4, which helps confirm that we have synthesized $CuCo_2S_4$, since there are several other PXRD patterns which are indistinguishable, such as $CuCo_5S_8$.

Synthesis and Characterization of CuCo₅S₈. Studying $CuCo_2S_4$ piqued our interest in other ternary thiospinels and we proceeded by synthesizing $CuCo_5S_8$. There has been only one published study of bulk $CuCo_5S_8$,[34] and to our best knowledge this is the first report of nano-sized $CuCo_5S_8$. The nanocrystals were synthesized using the method reported above, with a different ratio of copper to cobalt to sulfur precursor. UV-Vis solution phase absorbance shows a broad, featureless absorbance from 200 – 1000 nm. PXRD shows a crystalline spinel phase; however, the powder patterns for $CuCo_2S_4$ and $CuCo_5S_8$ are the same, since the only difference is the ratio of metals in the mixed sites in the crystal structure. (Figure 12).
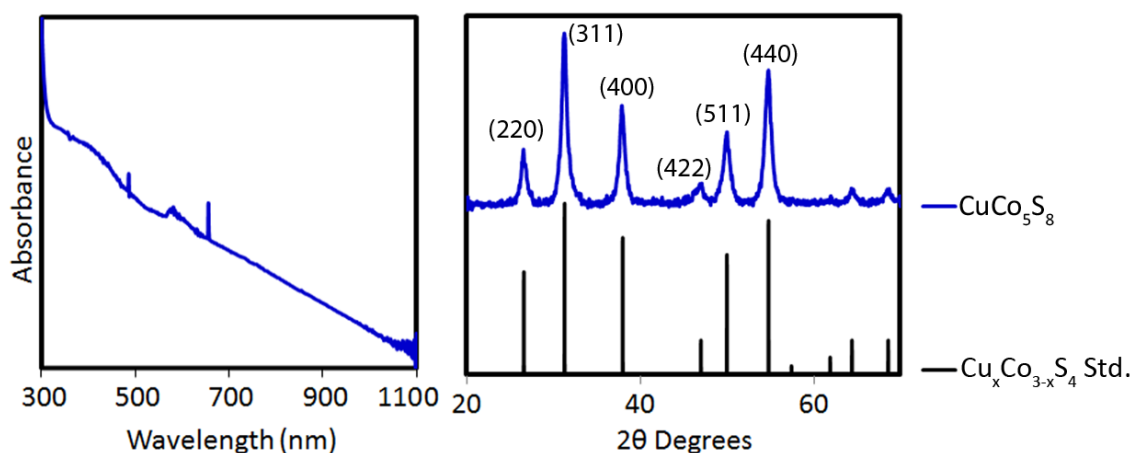

Figure 12. UV-Visible solution phase absorption and PXRD of $CuCo_5S_8$ nanocrystals.

TEM images show nanorod morphology with an average diameter of 6 ± 1 nm and an average length of 18 ± 4 nm after thiol washing to reduce the aggregation (Figure 13). Analysis of lattice fringes in TEM images gave a d spacing of 2.72 Å and 2.70 Å (Figure 14), matching well with the d spacing of the (400) plane in both $CuCo_2S_4$ and $CuCo_5S_8$. However, since the sample showed a rod-like morphology, which was different

from the $CuCo_2S_4$ sample (spheres) above, we believe this indicates that a different product was formed in this sample. EDX area scans confirm that the stoichiometry for Cu:Co:S was 1:3:5 (almost exactly the average of the two phases), so we can speculate that these particles may be an intermediate composition between the two phases.
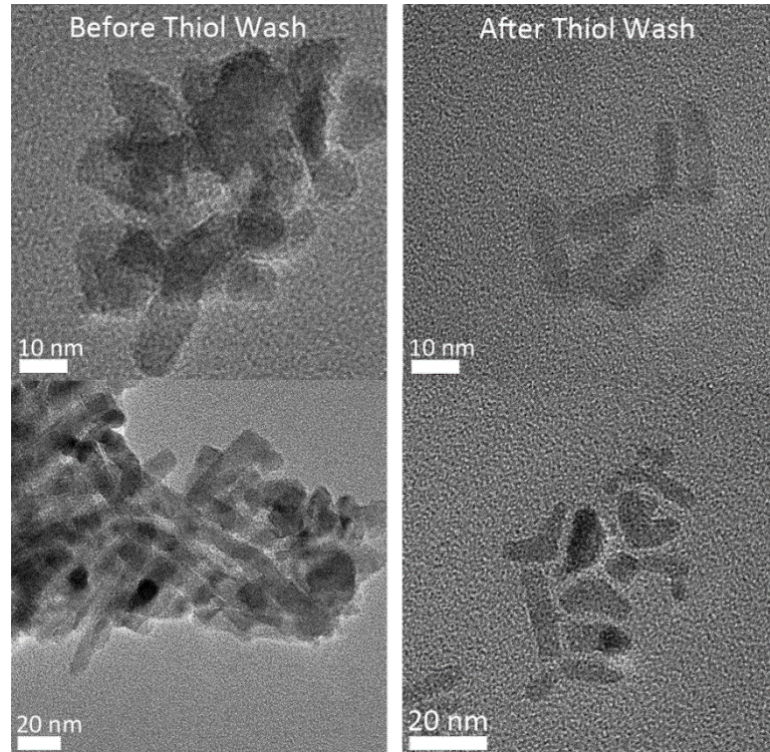

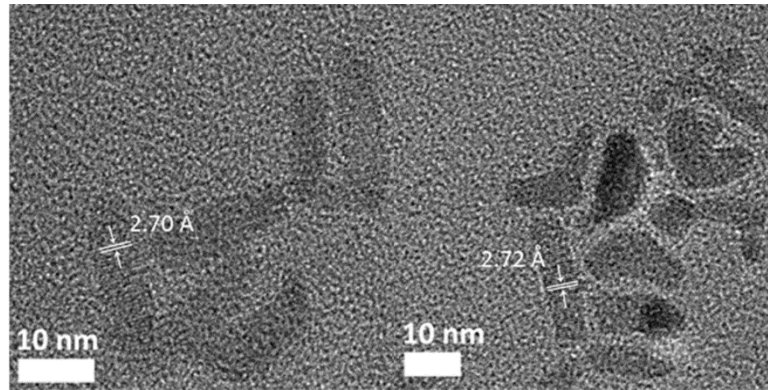**Figure 13.** TEM images before (left) and after (right) thiol washing $CuCo_5S_8$ nanocrystals

Figure 14. TEM images with lattice fringes analyzed.

Synthesis and Characterization of NiCo2S4. We also synthesized NiCo2S4 nanocrystals, which have been extensively studied for their utility as supercapacitors. The nanocrystals showed a spinel PXRD pattern (Figure 15), aggregated nanorod morphology in TEM images, and a broad absorption over the entire visible range. Thiol washing did not impact the aggregation in the sample (Figure 16). Since these nanocrystals have been rigorously examined by others, we did not perform any further characterization. We also attempted to synthesize several other thiospinels, including CuMn2S4, CuZn2S4, and CuNi2S4 without success.
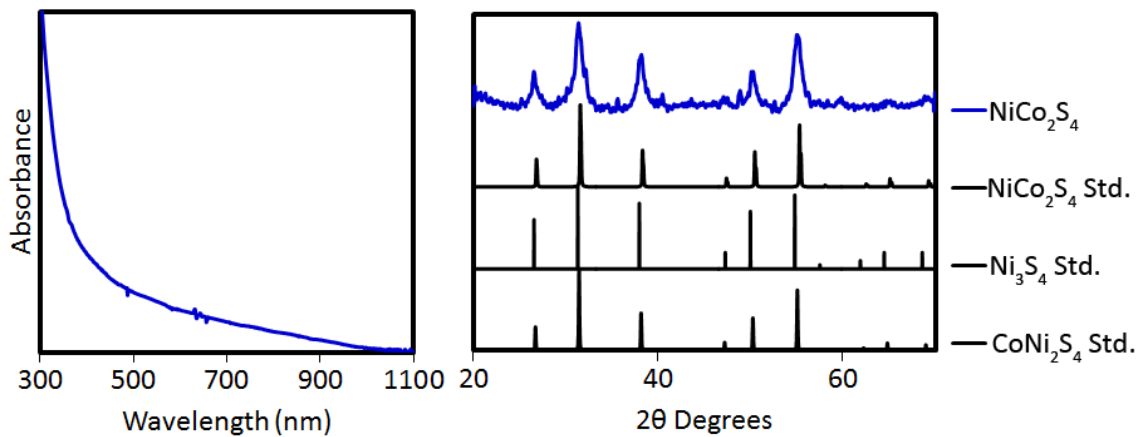

Figure 15. UV-Visible solution phase absorbance and PXRD of NiCo2S4 nanocrystals.
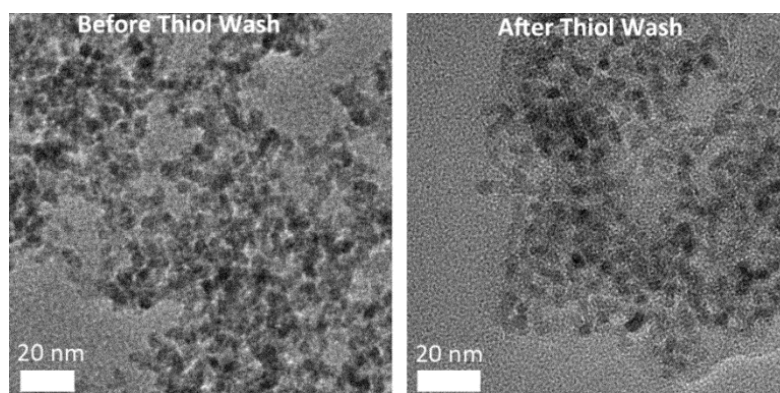
Figure 16. TEM images before (left) and after (right) thiol washing of $NiCo_2S_4$ nanocrystals.

Since we were able to synthesize $NiCo_2S_4$, but not $CuNi_2S_4$, we synthesized $NiCo_2S_4$ with copper, yielding $CuNiCoS_4$. The PXRD pattern was not distinguishable between $CuNiCoS_4$, $NiCo_2S_4$, and Ni_3S_4 (Figure 17), but EDX analysis showed that the molar ratio of Cu:Ni:Co:S was 1:1:1:1, which indicates that the particles were synthesized, but they are sulfur deficient, which indicates that there may be the presence of an amorphous impurity. The TEM images showed significant aggregation of particles, so we performed an extra thiol wash (Figure 18). After the thiol wash, images show that the nanocrystals were a mixture of spheres (mostly) and some nanorods, with an average diameter of 8 ± 3 nm, which corresponded well to the average size of 9 nm calculated using the Scherrer equation from the PXRD pattern.
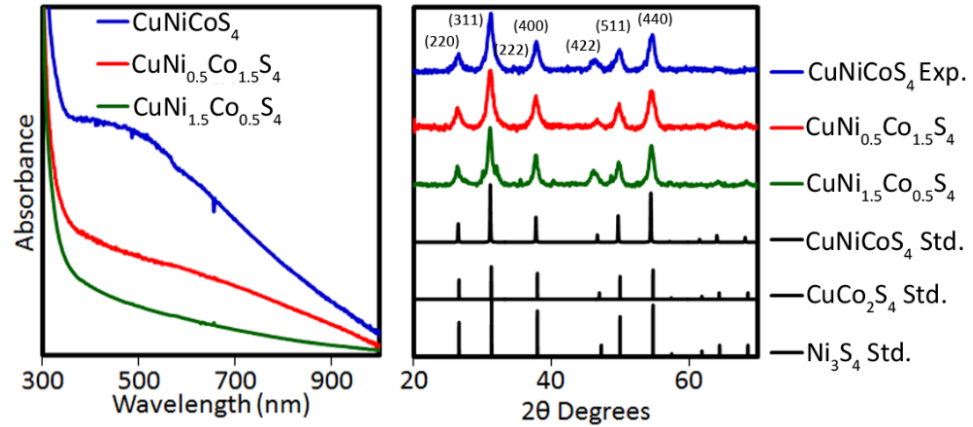
Figure 17. UV-Visible solution phase absorbance and PXRD of CuNiCoS₄, CuNi₁.₅Co₀.₅S₄, and CuNi₀.₅Co₁.₅S₄ nanocrystals.
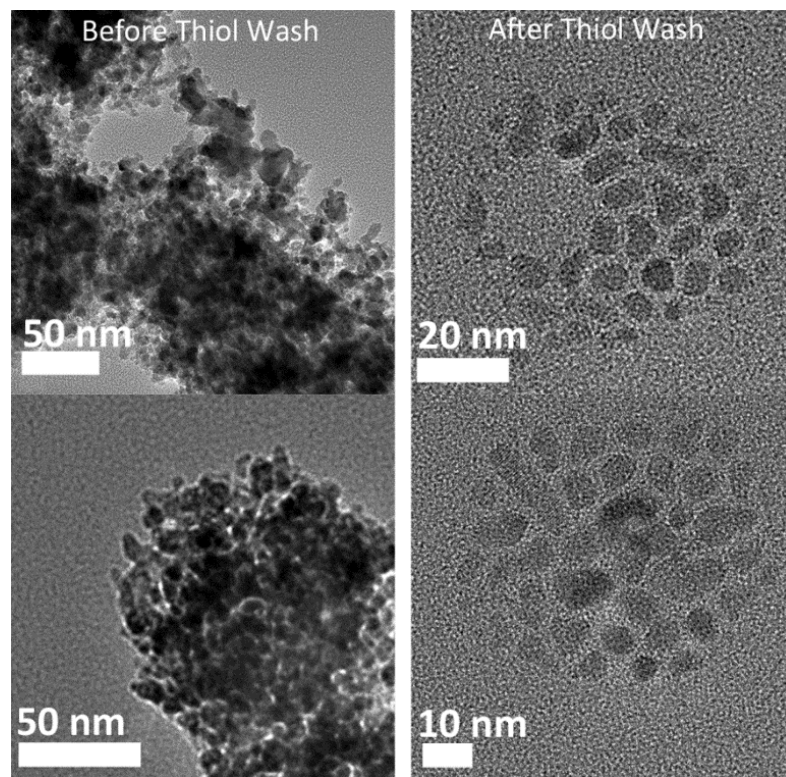

Figure 18. TEM images before (left) and after (right) thiol washing CuNiCoS₄ nanocrystals.

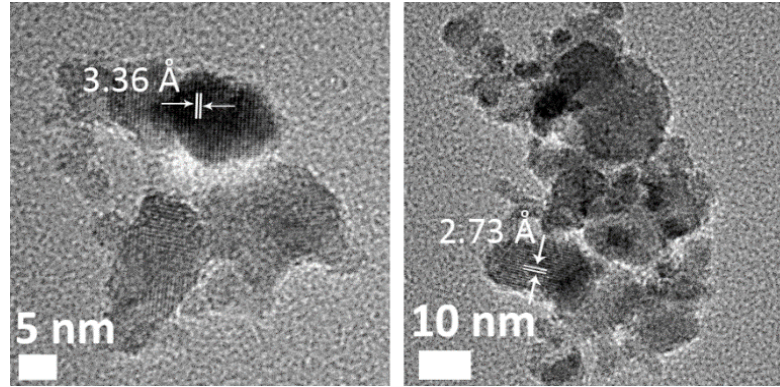**Figure 19.** TEM images showing lattice fringing and d spacing analysis. Left: $CuNi_{0.5}Co_{1.5}S_4$ Right: $CuNi_{1.5}Co_{0.5}S_4$

We also synthesized $CuNi_{1.5}Co_{0.5}S_4$, and $CuNi_{0.5}Co_{1.5}S_4$ nanoparticles. The PXRD patterns show a crystalline spinel phase, but again, several different patterns are nearly indistinguishable from one another (Figure 17). TEM analysis shows aggregated particles with distinct lattice fringing (Figure 19). Analysis shows a d spacing of 3.36 Å, which corresponds with the (220) plane and 2.73 Å, which corresponds to the (222) plane. EDX analysis shows that $CuNi_{1.5}Co_{0.5}S_4$ has a molar ratio of 1:0.4:0.4:1and $CuNi_{0.5}Co_{1.5}S_4$ has a molar ratio of 1:0.3:1.4:2. Both samples are sulfur deficient and the $CuNi_{1.5}Co_{0.5}S_4$ nanocrystals are deficient in nickel, which is possibly due to an amorphous impurity.

Conclusions

We attempted to synthesize ternary pyrite nanocrystals using hot-injection methods, as well as photochemical methods. Several different hot-injection methods, with various modifications to experimental parameters, consistently yielded the undesired thiospinel products or a mixture of metal sulfides, as did the photochemical methods. Although the syntheses of the ternary pyrites were unsuccessful in yielding the desired results, we will utilize these outcomes to influence the future directions of this project.

We have synthesized several ternary thiospinels: $CuCo_2S_4$ nanocrystals, $CuCo_5S_8$ nanorods, and $CuNi_xCo_{2-x}S_4$ nanocrystals with varying levels of nickel and cobalt loading. These are novel systems with a variety of potential applications in energy and catalysis. All of the nanocrystals show a broad absorbance in the visible range, and powder x-ray diffraction and transmission electron microscopy show that the particles are crystalline. The additional thiol wash proved to be effective at reducing aggregation of the nanocrystals in nearly every case. These nanocrystals could prove useful in energy applications, particularly batteries and catalysis.

Acknowledgments

References

[1] Li, T.; Li, H.; Wu, Z.; Hao, H.; Liu, J.; Huang, T.; Sun, H.; Zhang, J.; Zhang, H.; Guo, Z. Colloidal Synthesis of Greigite Nanoplates with Controlled Lateral Size for Electrochemical Applications. *Nanoscale* **2015**, *7*, 4171–4178.

[2] Park, M. S.; Kwon, S. K.; Min, B. I., Half-metallic Antiferromagnets in Thiospinels. *Phys. Rev. B.* **2001**, 64.

[3] Pearce, C. I.; Pattrick, R. A. D.; Vaughan, D. J. Electrical and Magnetic Properties of Sulfides. *Rev. Mineral. Geochem.* **2006**, *61*, 127–180.

[4] Lee, S. J.; Kim, J. E.; Park, H. Y., Optical Absorption of Co^{2+} in $MgIn_2S_4$, $CdIn_2S_4$, and $HgIn_2S_4$ Spinel Crystals. *J. Mater. Res.* **2003**, *18*, 733–736.

[5] Radautsan, S. I.; Tiginyanu, I. M., Defect Engineering in $II-III_2-IV_4$ and Related Compounds. *Japn. J. Appl. Phys.* **1993**, *32*, 5–9.

[6] Zhang, Y.; Sun, W.; Rui, X.; Li, B.; Tan, H. T.; Guo, G.; Madhavi, S.; Zong, Y.; Yan, Q. One-Pot Synthesis of Tunable Crystalline Ni_3S_4@Amorphous MoS_2 Core/Shell Nanospheres for High-Performance Supercapacitors. *Small* **2015**, *11*, 3694–3702.

[7] Wang, Q.; Jiao, L.; Du, H.; Si, Y.; Wang, Y.; Yuan, H. Co_3S_4 Hollow Nanospheres Grown on Graphene as Advanced Electrode Materials for Supercapacitors. *J. Mater. Chem.* **2012**, *22*, 21387–21391.

[8] Mahmood, N.; Zhang, C.; Jiang, J.; Liu, F.; Hou, Y. Multifunctional Co3S4/Graphene Composites for Lithium Ion Batteries and Oxygen Reduction Reaction. *Chem. Eur. J.* **2013**, *19*, 5183–5190.

[9] Bachhuber, F.; Rothballer, J.; Soehnel, T.; Weihrich, R., Phase Stabilities at a Glance II: Ternary ordering variants of Pyrite and Marcasite Type Structures. *Comp. Mater. Sci.* **2014**, *89*, 114–121.

[10] Bachhuber, F.; Krach, A.; Furtner, A.; Soehnel, T.; Peter, P.; Rothballer, J.; Weihrich, R., Phase stabilities of Pyrite-related MTCh Compounds (M=Ni, Pd, Pt; T=Si, Ge, Sn, Pb; Ch=S, Se, Te): A Systematic DFT Study. *J. Solid State Chem.* **2015**, *226*, 29–35.

[11] Mao, B.; Dong, Q.; Xiao, Z.; Exstrom, C. L.; Darveau, S. A.; Webber, T. E.; Lund, B. D.; Huang, H.; Kang, Z.; Huang, J., Zinc Alloyed Iron Pyrite Ternary Nanocrystals for Band Gap Broadening. *J. Mater. Chem. A* **2013**, *1*, 12060–12065.

[12] Donohue, P. C.; Bither, T. A.; Cloud, W. H.; Frederic.Cg, Magnetic and Electrical Properties of Ternary Pyrite-type $Cr_xCo_{1-x}S_2$ Phases Prepared at High Pressure. *Mater. Res. Bull.* **1971**, *6*, 231

[13] Xia, J.; Lu, X.; Gao, W.; Jiao, J.; Feng, H.; Chen, L. Hydrothermal Growth of Sn^{4+}-doped FeS_2 Cubes on FTO Substrates and its Photoelectrochemical Properties. *Electrochim. Acta* **2011**, *56*, 6932–6939.

[14] Thomas, B.; Ellmer, K.; Bohne, W.; Rohrich, J.; Kunst, M.; Tributsch, H. Photoeffects in Cobalt Doped Pyrite (FeS_2) Films. *Solid State Commun.* **1999**, *111*, 235–240.

[15] Lehner, S. W.; Newman, N.; van Schilfgaarde, M.; Bandyopadhyay, S.; Savage, K.; Buseck, P. R. Defect Energy Levels and Electronic Behavior of Ni-, Co-, and As-doped Synthetic Pyrite (FeS_2). *J. Appl. Phys.* **2012**, *111*.

[16] Liu, K.; Ji, N.; Ma, Z., Phases and Thermoelectric Properties of Bulk $NiSb2$ and Composite of $NiSb_2$ and $CoSb_3$ Prepared by Sintering. *Adv. Mater. Res.* **2012**, *503*, 507–510.

[17] Vaqueiro, P.; Sobany, G. G.; Guinet, F.; Leyva-Bailen, P. Synthesis and Characterisation of the Anion-ordered Tellurides MGeTe (M = Co, Rh). *Solid State Sci.* **2009**, *11*, 1077–1082.

[18] Han, J.-T.; Huang, Y.-H.; Huang, W. Solvothermal Synthesis and Magnetic Properties of Pyrite $Co_{1-x}Fe_xS_2$ with Various Morphologies. *Mater. Lett.* **2006**, *60*, 1805–1808.

[19] De Los Reyes, J. A.; Vrinat, M.; Geantet, C.; Breysse, M.; Grimblot, J. Supported Ternary Sulfide Phases: Characterization and Catalytic Properties of Alumina-Supported $Ni_xRu_{1-x}S_2$. *J. Catal.* **1993**, *142*, 455–464.

[20] Chen, H.; Jiang, J.; Zhang, L.; Wan, H.; Qi, T.; Xia, D., Highly Conductive $NiCo_2S_4$ Urchin-like Nanostructures for High-rate Pseudocapacitors. *Nanoscale* **2013**, *5*, 8879–8883.

[21] Liu, Y.; Zhang, J.; Wang, S.; Wang, K.; Chen, Z.; Xu, Q., Facilely Constructing 3D Porous $NiCo_2S_4$ Nanonetworks for High-performance Supercapacitors. *New J. Chem.* **2014**, *38*, 4045–4048.

[22] Chen, H.; Jiang, J.; Zhang, L.; Xia, D.; Zhao, Y.; Guo, D.; Qi, T.; Wan, H., In Situ Growth of $NiCo_2S_4$ Nanotube Arrays on Ni foam for Supercapacitors: Maximizing Utilization Efficiency at High Mass Loading to Achieve Ultrahigh Areal Pseudocapacitance. *J. Power Sources* **2014**, *254*, 249–257.

[23] Wiltrout, A. M.; Read, C. G.; Spencer, E. M.; Schaak, R. E. Solution Synthesis of Thiospinel $CuCo_2S_4$ Nanoparticles. *Inorg. Chem.* **2015**.

[24] Bezverkhyy, I.; Danot, M.; Afanasiev, P., New Low-temperature Preparations of Some Simple and Mixed Co and Ni Dispersed Sulfides and Their Chemical Behavior in Reducing Atmosphere. *Inorg. Chem.* **2003**, *42*, 1764–1768.

[25] Eisenberg, M., The Sulfospinel - Lithium Battery System - Initial Study of 3 Sulfospinels. *J. Electrochem. Soc.* **1980**, *127*, 2382–2383.

[26] Thackeray, M. M.; Depicciotto, L. A.; Dekock, A.; Johnson, P. J.; Nicholas, V. A.; Adendorff, K. T., Spinel Electrodes for Lithium Batteries - A Review. *J. Power Sources* **1987**, *21*, 1–8.

[27] Buckley, A. N.; Skinner, W. M.; Harmer, S. L.; Pring, A.; Fan, L.-J., Electronic Environments in Carrollite, $CuCo_2S_4$, Determined by Soft X-ray Photoelectron and Absorption Spectroscopy. *Geochim. Cosmochim. Acta* **2009**, *73*, 4452–4467.

[28] Oda, T.; Shirai, M.; Suzuki, N.; Motizuki, K., Electronic Band-structure of Sulfide Spinels CuM_2S_4 (M = Co, Rh, Ir). *J. Phys. Condens. Matter* **1995**, *7*, 4433–4446.

[29] Wada, S.; Sugita, H.; Miyatani, K.; Tanaka, T.; Nishikawa, T., Weak Antiferromagnetism and Superconductivity in Pseudo-binary Spinel Compounds $(Cu,Co)Co_2S_4$ Investigated by Co-59 and Cu-63 Magnetic Resonance. *J. Phys. Condens. Matter* **2002**, *14*, 219–230.

[30] Fang, L.; Zou, P. Y.; Lu, X. F.; Xu, Z.; Chen, H.; Shan, L.; Wen, H. H., Superconductivity in Thiospinel $Cu_{1.3}K_{0.2}Co_{1.5}S_4$. *Phys. Rev. B* **2005**, *71*.

[31] Craig, J. R.; Carpenter, A. B., Fletcherite, $Cu(Ni,Co)_2S_4$, a New Thiospinel from the Vibrunum Trend (New Lead Belt), Missouri. *Econ. Geo.* **1977**, *72*, 480–486.

[32] Thompson, M. J.; Ruberu, T. P. A.; Blakeney, K. J.; Torres, K. V.; Dilsaver, P. S.; Vela, J. Axial Composition Gradients and Phase Segregation Regulate the Aspect Ratio of Cu_2ZnSnS_4 Nanorods. *J. Phys. Chem. Lett.* **2013**, 4, 3918–3923.

[33] Singh, S.; Liu, P.; Singh, A.; Coughlan, C.; Wang, J.; Lusi, M.; Ryan, K. M. Colloidal $Cu_2ZnSn(SSe)_4$ (CZTSSe) Nanocrystals: Shape and Crystal Phase Control to Form Dots, Arrows, Ellipsoids, and Rods. *Chem. Mater.* **2015**, *27*, 4742–4748.

[34] Kesler, Y. A.; Smirnov, S. G.; Pokholok, K. V.; Viting, B. N., Peculiarities of the Electronic-structure of Co,Ni-Thiospinel. *Inorg. Mater.* **1991**, *27*, 977–980.

CHAPTER 5

SUMMARY AND CONCLUSIONS

This thesis demonstrates the synthesis, optimization, modification, and characterization of several ternary and quaternary nanocrystalline semiconductor materials. In the second chapter, we have shown that wurtzite CZTS nanorods commonly possess composition gradients along their axes. The composition gradients found in our nanocrystals were composed of a copper-rich end and an opposite zinc-rich end. Through experiments varying precursor loading and time evolution studies, we found that the reactivity of the three cationic precursors and relative rate of nucleation of the corresponding metal sulfides decrease as: $Cu(C_5H_7O_2)_2 > Zn(CH_3CO_2)_2 > Sn(CH_3CO_2)_4$.

Under stoichiometric conditions, the reactivity differences of the metal precursors lead to sequential nucleation events and axial composition gradients. Seeds made of copper sulfides quickly form by homogeneous nucleation, followed by heterogeneous nucleation of zinc and tin sulfides. Decreasing the loading of the copper precursor lowers the rate of nucleation of the copper sulfide seeds, which increases the nanorods' aspect ratio. When the three metal precursors nucleate at more comparable rates, it produces significantly longer CZTS nanorods with a more constant elemental composition along their axes. Increasing the copper precursor loading or changing the zinc and tin precursor loadings also produces significant changes to the composition and morphology of the products. Increasing the loading of tin precursor leads to CZTS nanorods with much less pronounced composition gradients along their axes. Thus, we have shown that cationic precursor loading predictably affects the morphology (dots vs. rods) and degree of axial phase segregation of anisotropic CZTS nanocrystals.

In the third chapter of this thesis, we show successful doping of these hexagonal (wurtzite) Cu_2ZnSnS_4 nanorods with Mn^{2+}, Co^{2+}, and Ni^{2+}. Experimental evidence (EPR and XPS) is consistent with substitution at the zinc site in the three series and all show a wurtzite crystal structure by powder XRD, nanorod morphology by TEM and broad absorption over the visible range, with a band gap ranging from 1.3-1.6 eV. EPR analysis confirms the presence of Mn^{2+} and Co^{2+} metal ions in a high spin configuration and XPS analysis elucidates the oxidation states of the metal dopants as Mn^{2+}, Co^{2+}, and Ni^{2+}. XPS was also used to determine the oxidation states of additional components as Cu^+, Sn^{4+}, Zn^{2+}, and S^{2-}.

Two additional purification washes were employed, along with the original methanol/ethanol wash. A TOPO wash was employed in the $Cu_2Mn_xZn_{1-x}SnS_4$ samples, since the additional TOPO ligands bind strongly to the excess Mn^{2+} on the surface of the nanocrystals and remove these ions upon centrifugation. The efficacy of this wash is confirmed by the EPR signal in the 3 atom% Mn sample. The spectrum before wash shows only one smooth curve, but post-wash, we see the expected six peak splitting pattern. Analogous to other systems, this change in the EPR spectrum indicates that the remaining manganese is located within (at the interior of) the nanocrystal lattice.

Several samples showed substantial aggregation, particularly Cu_2ZnSnS_4 and $Cu_2Ni_xZn_{1-x}SnS_4$ nanocrystals. We mitigated this problem by employing a thiol wash with a mixture of 1-dodecanethiol and tert-dodecylthiol, followed by centrifugation. We believe this aggregation is due to metal ions crosslinking the surface terminal sulfides of separate nanocrystals and upon washing, the additional free thiols bind and remove the

metal ions, leaving the terminal sulfurs free to oxidize in air. This hypothesis is supported by the sulfonate peaks found in the XPS and FTIR data after the thiol wash.

In the fourth chapter, we have synthesized several new nanocrystalline ternary thiospinels: $CuCo_2S_4$ nanocrystals, $CuCo_5S_8$ nanorods, and $CuNi_xCo_{2-x}S_4$ nanocrystals with varying levels of nickel and cobalt loading. All of the nanocrystals show a broad, fairly featureless absorbance in the visible range, and powder x-ray diffraction and transmission electron microscopy show that the particles are crystalline. The additional thiol wash introduced in chapter three proved to be effective at reducing aggregation of the ternary thiospinel nanocrystals in nearly every case.

We also attempted to synthesize ternary pyrite nanocrystals using several different synthetic methods. Many different hot-injection methods, with various modifications to experimental parameters, consistently yielded the undesired thiospinel products or a mixture of metal sulfides, as did the photochemical methods. Although the syntheses of the ternary pyrites were unsuccessful in yielding the desired results, we will utilize these outcomes to influence the future directions of this project.

The discoveries presented in this thesis will improve our ability to fabricate CZTS and similar nanostructures for photovoltaics, energy storage, data storage, spin-tronics and photocatalysis. More generally, they will aid our understanding of -and ability to control- phase segregation and doping in complex compound semiconductors such as quaternary CZTS.